

**QTDK/CVVWVF G'EJ CPI GU'QH'QDLGE VU'K''
PGCT'GCTVJ 'URCEG'KPF WEGF'D['P CVWT CN''
EJ CTI KPI**

Carolyn Frueh and Smriti Nandan Paul

**Purdue University
401 South Grant Street
West Lafayette, IN 47907-2024**

2 May 2017

Final Report

APPROVED FOR PUBLIC RELEASE; DISTRIBUTION IS UNLIMITED.



**AIR FORCE RESEARCH LABORATORY
Space Vehicles Directorate
3550 Aberdeen Ave SE
AIR FORCE MATERIEL COMMAND
KIRTLAND AIR FORCE BASE, NM 87117-5776**

DTIC COPY NOTICE AND SIGNATURE PAGE

Using Government drawings, specifications, or other data included in this document for any purpose other than Government procurement does not in any way obligate the U.S. Government. The fact that the Government formulated or supplied the drawings, specifications, or other data does not license the holder or any other person or corporation; or convey any rights or permission to manufacture, use, or sell any patented invention that may relate to them.

This report is the result of contracted fundamental research deemed exempt from public affairs security and policy review in accordance with SAF/AQR memorandum dated 10 Dec 08 and AFRL/CA policy clarification memorandum dated 16 Jan 09. This report is available to the general public, including foreign nationals. Copies may be obtained from the Defense Technical Information Center (DTIC) (<http://www.dtic.mil>).

AFRL-RV-PS-TR-2017-0007 HAS BEEN REVIEWED AND IS APPROVED FOR
PUBLICATION IN ACCORDANCE WITH ASSIGNED DISTRIBUTION STATEMENT.

//SIGNED//
RYAN WEISMAN
Program Manager

//SIGNED//
PAUL HAUSGEN, Ph.D.
Technical Advisor, Spacecraft Component Technology

//SIGNED//
JOHN BEAUCHEMIN
Chief Engineer, Spacecraft Technology Division
Space Vehicles Directorate

This report is published in the interest of scientific and technical information exchange, and its publication does not constitute the Government's approval or disapproval of its ideas or findings.

Approved for public release; distribution is unlimited.

REPORT DOCUMENTATION PAGE				Form Approved OMB No. 0704-0188	
Public reporting burden for this collection of information is estimated to average 1 hour per response, including the time for reviewing instructions, searching existing data sources, gathering and maintaining the data needed, and completing and reviewing this collection of information. Send comments regarding this burden estimate or any other aspect of this collection of information, including suggestions for reducing this burden to Department of Defense, Washington Headquarters Services, Directorate for Information Operations and Reports (0704-0188), 1215 Jefferson Davis Highway, Suite 1204, Arlington, VA 22202-4302. Respondents should be aware that notwithstanding any other provision of law, no person shall be subject to any penalty for failing to comply with a collection of information if it does not display a currently valid OMB control number. PLEASE DO NOT RETURN YOUR FORM TO THE ABOVE ADDRESS.					
1. REPORT DATE (DD-MM-YYYY) 02-05-2017		2. REPORT TYPE Draft Final Report		3. DATES COVERED (From - To) 21-05-2015 – 21-02-2017	
4. TITLE AND SUBTITLE Orbit-Attitude Changes of Objects in Near Earth Space Induced by Natural Charging				5a. CONTRACT NUMBER	
				5b. GRANT NUMBER FA9453-15-1-0309	
				5c. PROGRAM ELEMENT NUMBER 62601F	
6. AUTHOR(S) Carolyn Frueh and Smriti Nandan Paul				5d. PROJECT NUMBER 8809	
				5e. TASK NUMBER PPM00020200	
				5f. WORK UNIT NUMBER EF125340	
7. PERFORMING ORGANIZATION NAME(S) AND ADDRESS(ES) Purdue University 401 South Grant Street West Lafayette, IN 47907-2024				8. PERFORMING ORGANIZATION REPORT NUMBER	
9. SPONSORING / MONITORING AGENCY NAME(S) AND ADDRESS(ES) Air Force Research Laboratory Space Vehicles Directorate 3550 Aberdeen Ave, SE Kirtland AFB, NM 87117-5776				10. SPONSOR/MONITOR'S ACRONYM(S) AFRL/RVSV	
				11. SPONSOR/MONITOR'S REPORT NUMBER(S) AFRL-RV-PS-TR-2017-0007	
12. DISTRIBUTION / AVAILABILITY STATEMENT Approved for public release; distribution is unlimited.					
13. SUPPLEMENTARY NOTES					
14. ABSTRACT This research investigates the effect of naturally induced Lorentz force perturbations on the orbital evolution of near Earth space objects. Natural charging of all space objects occurs in the natural space plasma environment. The charging levels are dependent on the local plasma environment, the (surface) materials of the space object and its geometry (capacitance). When the charge is moving relative to the Earth magnetosphere, Lorentz forces are induced. The Lorentz forces are in turn an orbital perturbation force. The emphasis of this research focuses on the low Earth orbital region and geosynchronous region. The charging of a spherical space object and the orbital effects are shown. A full numerical solution of the steady state plasma interactions are derived, for high charging and low charging conditions and low and high area-to-mass ratio objects. In order to speed up computational time, analytic expressions utilizing variational equations have been derived. High charging plasma conditions lead to significant secular perturbations in the investigated cases.					
15. SUBJECT TERMS State-of-the Art; Attitude Propagation; Magnetic Field; Geosynchronous Orbit; Satellite Components; Electrons; Operational Anomalies					
16. SECURITY CLASSIFICATION OF:			17. LIMITATION OF ABSTRACT Unlimited	18. NUMBER OF PAGES 88	19a. NAME OF RESPONSIBLE PERSON Ryan Weisman
a. REPORT Unclassified	b. ABSTRACT Unclassified	c. THIS PAGE Unclassified			19b. TELEPHONE NUMBER (include area code)

(This page intentionally left blank)

TABLE OF CONTENTS

Section	Page
List of Figures	ii
List of Tables	iii
1.0 SUMMARY	1
2.0 INTRODUCTION	1
3.0 METHODS, ASSUMPTIONS AND PROCEDURES	3
3.1 Assumptions	3
3.2 Orbital Differential Equation	3
3.3 Earth Magnetosphere	5
3.4 Space-Plasma Environment	6
3.5 Plasma Current Model	7
3.6 Secondary Electron Current Model	13
3.7 Backscattering Current Model	17
3.8 Photoelectron Current Model	23
3.9 Capacitance Modeling	34
3.10 Spherical Capacitance Model	34
3.11 Analytic Expressions for Orbital Perturbation Due to Lorentz Force	35
3.12 General and LEO Perturbation Expressions for One Orbital Period	39
3.13 GEO Perturbation Expressions for One Orbital Period	41
4.0 RESULTS AND DISCUSSION	42
4.1 Low Earth Orbit Simulation	43
4.2 Geosynchronous Earth Orbit Simulation	52
4.3 Comparison of Analytic Expressions	59
5.0 CONCLUSIONS	59
REFERENCES	61
APPENDIX A - General Perturbation Coefficients	65
APPENDIX B - LEO Perturbation Coefficients.	71
APPENDIX C - Perturbation Expressions from Peng, et al.	74
APPENDIX D - Publications and Presentations	75
APPENDIX E - Abstracts	76
LIST OF SYMBOLS, ABBREVIATIONS, AND ACRONYMS	77

LIST OF FIGURES

Figure	Page
1 1D System of Particles Hitting a Wall	8
2 Side View of Wall Area A Being Hit by Particles	8
3 Backscatter Cone	20
4 Backscatter Cone, scattered electrons.	21
5 AM 0 Spectrum	24
6 Electric Field Break Down into Parallel and Perpendicular Directions	28
7 Charging Characteristic of LEO Under Low-Charge Plasma Conditions (LAMR)	45
8 Voltage Characteristic of LEO Objects (LAMR, High-Charge Plasma Condition)	46
9 Common Logarithm of Perturbing Acceleration Magnitudes for LEO Orbits Under Low-Charge Plasma Conditions	47
10 In-track Perturbations for Lorentz Force Perturbed Low Earth Orbit Relative to Lorentz Force Excluded Orbit Under Low-Charge Plasma Conditions (LAMR Object)	48
11 Cross-track Perturbations for Lorentz Force Perturbed Low Earth Orbit Relative to Lorentz Force Excluded Orbit Under Low-Charge Plasma Conditions (LAMR Object)	49
12 Radial Perturbations for Lorentz Force Perturbed Low Earth Orbit Relative to Lorentz Force Excluded Orbit Under Low-Charge Plasma Conditions (LAMR Object)	50
13 In-Track Perturbations, Cross-Track perturbations, Radial Perturbations for Lorentz Force Perturbed Low Earth Orbit Relative to Lorentz Force Excluded Orbit Under High-Charge Plasma Conditions (LAMR object)	51
14 Charging Characteristic of GEO Group 1 (LAMR, Low-Charge Plasma Condition)	54
15 Common Logarithm of Perturbing Acceleration Magnitudes for GEO Orbits, Low-Charge Plasma Condition	55
16 In-Track Perturbations for Lorentz Force Perturbed GEO Relative to Lorentz Force Excluded Orbit (HAMR Object)	57
17 Cross-Track Perturbations for Lorentz Force Perturbed GEO Relative to Lorentz Force Excluded Orbit (HAMR Object)	57
18 Radial Perturbations for Lorentz Force Perturbed GEO Relative to Lorentz Force Excluded Orbit (HAMR Object)	58
19 Difference in Semi-Major Axis, Eccentricity and Inclination for Cases With and Without Lorentz Force Modeling. GEO Group 1 Under High-Charge Plasma Condition (HAMR)	58

LIST OF TABLES

Table	Page
1 Table Summarizing Plasma Currents	11
2 Arguments Against Anderson's Voltage Formulation	13
3 The LEO Cases	43
4 Plasma Parameters Inside Auroral Oval	44
5 Perturbations of HAMR Object in LEO Under Low-Charge Plasma Conditions After One Orbital Time-Period	52
6 Perturbations of HAMR Object in LEO Under High-Charge Plasma Conditions After One Orbital Time-Period	52
7 The GEO Cases	53
8 High-Charge Plasma Environment for GEO	53
9 Orders of Magnitude for In-Track, Cross-Track and Radial Perturbations for LAMR Objects in GEO Over a Period of Four Days	59
10 Values of Orbital Perturbations for LAMR Objects in LEO Under Low-Charge Plasma Conditions	59

ACKNOWLEDGMENTS

This material is based on research sponsored by Air Force Research Laboratory under agreement number FA9453-15-1-0309. The U.S. Government is authorized to reproduce and distribute reprints for Governmental purposes notwithstanding any copyright notation thereon.

DISCLAIMER

The views and conclusions contained herein are those of the authors and should not be interpreted as necessarily representing the official policies or endorsements, either expressed or implied, of Air Force Research Laboratory or the U.S. Government.

1.0 SUMMARY

This work models charging of space objects and investigates the effect it has on the orbital evolution of those objects. In the approach that is presented in this research, a spherical conductor model has been adopted. In a steady state approach, charging levels have been derived under low-charging plasma condition and high-charging plasma condition. A dipole model for the Earth magnetosphere has been adopted. Formulations for Luni-Solar gravitational force and solar radiation pressure are taken from Frueh et al. [1]. In this research, we include Earth gravitational spherical expansion up to order and degree 12 [2]. Gosudarstvennyy Standart (GOST) model [3] is used to simulate atmospheric drag force in low Earth orbit. Atmospheric drag is assumed to be absent in geosynchronous orbits. This research will improve understanding of space plasma environment in the low Earth orbits (LEO) and geosynchronous Earth orbits (GEO), and how the plasma interacts with space objects leading to charge development. It will also shed light into photo-emission effect on charging. The research will investigate effects of Lorentz force on orbital evolution of standard low area to mass ratio (LAMR) objects and highly perturbation susceptible high area to mass ratio (HAMR) objects. Furthermore, it will shed light into effects of presence/absence of sunlight and orbit inclination on the evolution of orbital parameters.

2.0 INTRODUCTION

High fidelity propagation models are integral for the long and short term orbital prediction of near Earth space objects. For a robust space catalog, the orbit prediction of an individual object has to be better than half the field of view of the observing sensor; which is of the order of several degrees down to less than half a degree. The frequency of observations can be really low, sometimes the time between two consecutive observations can exceed 30 orbital periods. Ideally, orbital predictions need to be on the arc second level several days ahead to allow for an informed decision about possible collision avoidance maneuvers.

In the orbit prediction, usually perturbation forces include higher harmonics of Earth's gravity, Luni-Solar gravitational forces, solar radiation pressure (cannonball model), and atmospheric drag. An important question, however, remains is whether the inclusion of other perturbation forces beyond those mentioned above is significant for precise orbit propagation. In this research, Lorentz force has been considered as an additional perturbation.

A body obtains a charge when there is a difference between the fluxes of electrons and ions received by the body. In this case the object develops a potential so as to reduce the flux of more available particle and increase the flux of less available particle until both of them equal out and the body reaches an equilibrium state. Natural space plasma is sufficient to introduce significant charges. Spacecraft charging research has first come into focus because of several satellite anomalies observed during the 1970s. The 1973 failure of Defense Satellite Communications System (DSCS) 9431 satellite of US Air Force because of a discharge lead National Aeronautics and Space Administration (NASA) and the US Air Force to investigate the effects of charging and develop technologies to mitigate the same. Accumulated charges may result in currents entering the tender circuits and impeding their functionality. Sometimes, differential charging across various parts of the space-craft can be high enough to initiate arcing. The effects of arcing on the on-board electronics can

vary from mild to fatal depending on the magnitude of differential voltage and the spacecraft material. Charged particles can also create strong electric fields, which can interfere with sensitive scientific instruments, resulting in wrong data measurements.

Several studies investigating charging in the near geosynchronous orbit have been done. DeForest [4] investigated charging of ATS-5 satellite in geosynchronous orbit. He found that there were high levels of charging of the order of thousands of negative volts during eclipse and few hundred negative volts during sunlit conditions. The difference in charging levels between shadow and sun light conditions result from the emission of photo electrons. Mullen et al. [5] analyzed the high-level charging under sunlit condition. Their work was based on data from Spacecraft Charging at High Altitudes (SCATHA) satellite. Although less common, high-level charging can also be experienced in low Earth orbit. Defense Meteorological Satellite Program (DMSP) spacecraft in low Earth polar orbit was found to charge up to voltage as high as -2000 volts [6]. In addition to the few mentioned studies, comprehensive texts by Shu [7], Hastings and Garrett [8] have greatly furthered theoretical knowledge of space environment and charging.

Several existing software are available for simulating spacecraft charging. Jointly developed by NASA and Air Force Research Laboratory (AFRL), NASA/Air Force Spacecraft Charging Analysis Program (NASCAP-2K) [9] is probably the most widely known software in this regard. The computations employed by NASCAP-2K involves both analytic and particle-in-cell (PIC) methods, and it is based on previously developed NASA Charging Analyzer Program for Low-Earth Orbit (NASCAP-LEO), NASA Charging Analyzer Program for Geosynchronous Orbit (NASCAP-GEO) and Potentials Of Large objects in the Auroral Region (POLAR). The Spacecraft Plasma Interaction System (SPIS) is an open-source software under development and it is based on three-dimensional particle-in-cell computations. It includes several detailed interactions like photoelectric effect, secondary emission, etc. but the software graphics and documentation still need to be improved so as to increase user-friendliness. Commercially available spacecraft-charge simulating software include Multi-Utility Spacecraft Charging Analysis Tool (MUSCAT) [10] and Spacecraft Charging Software (SPARCS) [11].

The focus of the aforementioned tools is the precise investigation of charging levels with respect to a pre-launch satellite design. The interest is to compute charge spikes for a given orbital design. Hence, the calculations are based upon the assumption that the objects are placed on Keplerian orbits.

However, when the charged object moves relative to the Earth magnetosphere, Lorentz forces are induced. Those forces result in orbital perturbations. First steps towards evaluating how significant Lorentz force perturbations are in the orbital evolution of natural objects, a few preliminary studies have been made. Antal et al. [12] studied the dynamics of charged micron and sub-micron sized space debris particles in Earth's plasma environment. Aziz [13] used Lagrange planetary equations to derive analytical formulas for perturbations in orbital elements of middle Earth LA-GEOS satellite due to Lorentz force, while assuming a fixed value, rather than the one induced by the actual plasma conditions in the orbital region, for body charge. Peng et al [14] derived Gauss variational equations for Lorentz force perturbations under the assumption of an invariant Earth magnetic dipole. Frueh et al. [15] simulated orbital evolution of HAMR flat plates in geostationary orbit. They took into account solar radiation pressure, Earth's gravity, third body perturbations

and Lorentz force. In their simulation, charging plasma values were computed in interaction of the orbital propagation and recurrent use of the NASCAP-2k tool, to allow the computation of the charging in the natural and changing plasma environment.

In this study, the work from Frueh et al has been developed further. Instead of relying on the NASCAP tool, the natural charging effects have been computed alongside the orbital propagation, in order to be able to investigate the effect of the Lorentz perturbations as realistically as possible in a computationally feasible integrated fashion. In order to allow for computational fast computations, the analytic variational equations from Peng et al [14] have been expanded.

This report is organized as the following: In the next section, the model and assumptions are introduced. The model consist of the dipole model of the Earth magnetosphere with time varying coefficients, the plasma environment. Subsequently, the modeling of the space object charging and its capacitance is shown. The analytic variational equation expressions are then introduced. In the next section the numerical test cases are shown and discussed. Test orbits of high and low area-to-mass ratio objects in low Earth orbit and geosynchronous orbital region have been propagated. The report concludes with a summary of the findings and the conclusions. In Appendices A and B, coefficients of the variational equations developed in this research can be found, and in Appendix C, Peng's [14] variational equations are listed for comparison. Symbols, abbreviations and acronyms follow the appendices.

3.0 METHODS, ASSUMPTIONS AND PROCEDURES

3.1 Assumptions

In the approach that is presented in this research, a spherical conductor model has been adopted. In a steady state approach, charging levels have been derived Under Low-charging plasma condition and high-charging plasma condition. A dipole model for the Earth magnetosphere with time varying coefficients has been adopted [16]. Formulations for Luni-Solar gravitational force and solar radiation pressure are taken from Frueh et al. [1]. Earth gravitational spherical expansion up to order and degree 12 [2] are modeled. Model [3] is used to simulate atmospheric drag force in low Earth orbit. Atmospheric drag is assumed to be absent in geosynchronous orbits.

3.2 Orbital Differential Equation

A three degree of freedom motion is assumed for the debris since a spherical geometry is considered in this study. The following equation of motion holds for center of mass,

$$\ddot{\vec{x}} = -GM_{\oplus}\nabla V(\vec{x}) - G \sum_{k=1,2} M_k \left[\frac{\vec{x} - \vec{x}_k}{|\vec{x} - \vec{x}_k|^3} + \frac{\vec{x}_k}{x_k^3} \right] + \sum_l \vec{a}_l \quad (1)$$

where \vec{x} is the geocentric position of the object, G the gravitational constant, M_{\oplus} the Earth mass and $V(\vec{x})$ the Earth gravitational potential. The formulation of Pines [2] has been implemented for the gravitational potential representations, and the user can choose order and degree representations up to 100. The third body gravitational perturbations of the Sun and Moon ($k=1, 2$) with the states \vec{x}_k are modeled via their center of mass. The Sun and Moon masses are represented by M_k

(k=1, 2). Finally, $\sum \vec{a}_l$ is the sum over all non-gravitational accelerations acting on the satellite. Solar radiation pressure, atmospheric drag and Lorentz force are the three non-gravitational forces considered in this paper.

The acceleration due to solar radiation pressure for a spherical body of radius r is modeled as,

$$\vec{a}_{rad} = -\frac{4\pi r^2 E}{m} \frac{A_{\oplus}^2}{c |\vec{x} - \vec{x}_{\odot}|^2} \left(\frac{1}{4} + \frac{1}{9} C_d \right) \hat{S} \quad (2)$$

where m represents the total mass of the body, E represents solar flux at 1 AU, c represents speed of light, A_{\oplus} represents astronomical unit and C_d is the diffuse reflection coefficient. \vec{x} , \vec{x}_{\odot} , \hat{S} represent geocentric position of object, geocentric position of sun and direction of radiation source, respectively.

The acceleration due to atmospheric drag force is modeled as,

$$\vec{a}_{drag} = -\frac{1}{2} \frac{\tilde{c}_D A_{ref} \rho |\vec{v}_{relv}| \vec{v}_{relv}}{m} \quad (3)$$

where \tilde{c}_D is drag coefficient, A_{ref} is reference area, ρ is atmospheric density and \vec{v}_{relv} is velocity of body relative to atmosphere. A_{ref} is taken as spherical cross-sectional area i.e., πr^2 and the atmosphere is assumed to be co-rotating with Earth. The density ρ is obtained using GOST model as,

$$\rho = \rho_n k_0 k_1 k_2 k_3 k_4 \quad (4)$$

where the parameters ρ_n and k_j ($j=1,2,3,4$) are semi-empirical factors that take into account various aspects like diurnal variation, solar cycle, semi-annual variation, etc. and can be obtained from Vallado [3].

The acceleration due to Lorentz force is modeled as,

$$\vec{a}_{charge} = \frac{q \vec{v}_{rel} \times \vec{B}}{m} \quad (5)$$

where \vec{B} is the Earth magnetic field, q is the surface charge of spherical body and \vec{v}_{rel} is the velocity of the object relative to the magnetic field. Charge q can be obtained from potential ϕ of the space object using the following relation,

$$q = C\phi \quad (6)$$

where C is body capacitance. The body potential ϕ is obtained by solving the so-called current equation.

A variety of currents contribute to body charging. A body in space acts like a node in an electrical circuit and hence Kirchhoff's current law is applicable. At equilibrium, according to Kirchhoff's law,

$$\sum_j I_j(\phi) = 0 \quad (7)$$

$$I_i + I_e + I_{ph} + I_{se} + I_{bsc} + I_{misc} = 0 \quad (8)$$

where I_i is plasma ion current, I_e is plasma electron current, I_{ph} is photoelectric current, I_{se} is secondary electron current, I_{bsc} is backscattered current and I_{misc} is miscellaneous current. Miscellaneous current includes all currents apart from ones just mentioned, and it will be neglected in all the theoretical developments and simulations in this work. Some important components constituting miscellaneous current may include electron beam emission, neutral particle generated secondary electrons and ions, etc. ϕ appearing in Equation (7) is body potential.

In non-equilibrium scenario, charging takes place according to the differential equation, $\sum_j I_j = C \frac{d\phi}{dt}$. The time scale for charging of a spherical conductor can be given approximately by [25],

$$\tau_{ts} \approx \frac{C\phi}{4\pi r^2 J} \quad (9)$$

where the subscript ts stands for transient time. The parameters C , ϕ , r , J represent body capacitance, body potential, body radius and ambient flux, respectively. In this research, the charging time scale is much smaller compared to orbit propagation time steps and hence equilibrium current condition is assumed.

3.3 Earth Magnetosphere

Lorentz acceleration given by Equation (5) depends upon Earth's magnetosphere. Typically, magneto-sphere models can be grouped under two classes: statistical and physics-based. The Physics-based models are computationally expensive and difficult to solve as they require solving numerically several nonlinear partial differential equations on a three-dimensional grid of points. They take magnetohydrodynamic (MHD) flows of the plasma into consideration for simulating the magnetic field. Statistical models, on the other hand, are based on empirical formulations and are most reliable under weak storm scenarios.

Early geomagnetosphere models were primarily physics-based due to unavailability of sufficient space-data, but over the last three decades, with the availability of huge amount of data from satellites and space-instruments, trend has shifted towards use of statistical models. Mead-Fairfield geomagnetic field model [17] is one of the earliest statistical models. The model is valid till 17 earth radii, and it is created with the help of data from Interplanetary Monitoring Platform (IMP) satellites spanning over the period from 1966 to 1972. The Mead-Fairfield model is linear in tilt, quadratic in position and power series (second order) in solar magnetic coordinates. Following this, Tsyganenko, Usmanov, and Sitnov [18, 19] contributed significantly to the development of statistical models. The Tsyganenko magnetic field model is based on data from various satellites like IMP, Highly Eccentric Orbit Satellite (HEOS), International Sun-Earth Explorer (ISEE), Polar, Geotail, etc. The model takes into consideration the effect of ring current, magnetotail current system, magnetopause current, field-aligned current system.

Olson-Pfitzer quiet, 1977 [20] is another early statistical Earth magnetic field model developed with the aid of data from Orbiting Geophysical Observatory (OGO) 3 and 5. The model's validity extends from dayside subsolar magnetosphere to farther than lunar orbit in the nightside magnetotail. This model, however, applies to only quiet conditions. It includes the contributions from tail, magnetopause and ring currents and the core field is approximated by a fixed dipole.

A modification of Olson-Pfitzer Field Model (1977) is Olson-Pfitzer Dynamic Model, 1988 [21]. It takes into consideration the variation in the size and strength of primary magnetospheric current systems resulting from interplanetary sources. The model is appropriate for dayside magnetic field at geosynchronous orbit for any magnetic condition and nightside field for quiet conditions. The Ostapenko-Maltsev Magnetic Field Model, 1997 [22] is another model which uses the database of Fairfield et al. [23] and valid for $3R_E$ to $7R_E$. The model is dependent on geomagnetic indices K_p and D_{st} , solar wind dynamic pressure and z-component of interplanetary magnetic field.

The Lyon-Fedder-Mobarry (LFM) code is a three-dimensional MHD modeling of the magnetosphere and the work on the code first started around 1985. Over the years, the code has been continuously improved to accommodate better resolving power transport; an adaptable grid based on the problem statement; addressing the problem of non-zero $\nabla \cdot \vec{B}$; improvement upon the cases of high Alfvén speed, low ratio of plasma pressure to magnetic pressure and strong magnetic field gradients; and integration of ionospheric model [24].

The work carried out here uses the empirical dipole magnetic field model. The model is a first order approximation of Earth's actual magnetic field. The implementation of dipole model is simple, and is particularly accurate at low Earth altitudes. Equations (10), (11), (12) represent the dipole model [16], where the parameters η , ξ , ζ represent geocentric distance, co-elevation and East longitude from Greenwich, respectively. r_E is equatorial radius of Earth. The parameters g_i^j and h_i^j are International Geomagnetic Reference Field (IGRF) coefficients and can be obtained from data released by International Association of Geomagnetism and Aeronomy (IAGA).

$$B_\eta = 2 \left(\frac{r_E}{\eta} \right)^3 \left[g_1^0 \cos \xi + (g_1^1 \cos \zeta + h_1^1 \sin \zeta) \sin \xi \right] \quad (10)$$

$$B_\xi = \left(\frac{r_E}{\eta} \right)^3 \left[g_1^0 \sin \xi - (g_1^1 \cos \zeta + h_1^1 \sin \zeta) \cos \xi \right] \quad (11)$$

$$B_\zeta = \left(\frac{r_E}{\eta} \right)^3 \left[g_1^1 \sin \zeta - h_1^1 \cos \zeta \right] \quad (12)$$

3.4 Space-Plasma Environment

Body charge depends on longitude, local time and altitude, because of varying plasma conditions [7]. Current work focuses on low Earth altitudes (approximately 150 Km to 2000 Km) and geosynchronous altitude only. In the current work, for the low Earth regions, local time and longitudinal variations of plasma data are neglected focusing only on altitude dependent effects as they appear to be the most crucial ones. For the geosynchronous region, only the local time variations are considered because of limitations in data availability. Plasma at low Earth orbits is usually of low energy (typically less than .1 eV energy) and high density (typically 10^5 cm^{-3} or higher). At geosynchronous altitudes, plasma density is relatively small (around 1 cm^{-3}), but plasma energy is high, typically around 100 eV, often reaching KeV ranges during geomagnetic storm activities. A Geomagnetic storm is a space weather phenomena resulting from rapid increase in energy transfer from Sun to Earth's magnetosphere and typically caused by solar coronal mass ejections (CME). Bodies in geosynchronous orbit typically get positively charged in sunlight due to emission of

photo-electrons. The photoelectric current in geosynchronous region is of similar order as that of the dominant plasma electron current and hence it is a major contributor to body charge. For low Earth region, photoelectric current is relatively insignificant as plasma currents are much larger than photoelectric current. In geosynchronous shadow region and in all of low Earth region, bodies are typically negatively charged because of dominant plasma electron current.

Once the voltage is determined from current equilibrium, the charge can be determined using capacitance. The capacitance is both object geometry dependent and plasma dependent. The plasma dependence is characterized by means of the so-called Debye length. When a body gets charged, it attracts the species of opposite polarity and repels the species of same polarity and as a result, a layer adjacent to body is formed which is rich in opposite polar species and poor in same polar species. A Debye length is roughly the distance outside which no effect of the body charge is felt i.e., the electric field of the body roughly cancels out the electric field of the opposite polar species surrounding the body. Since plasma density is less in geosynchronous Earth orbit as compared to low Earth orbit, more thickness of the opposite polar species would be required in geosynchronous orbit to cancel out the electric field due to body charging and hence Debye length is comparatively large or sheath is thick. Opposite is true for low Earth orbit and the plasma sheath is thin. For geosynchronous orbit, Debye length is typically greater than 200m whereas for low Earth orbit, it is in millimeter range. As will be seen later, formulation of current depends on sheath thickness. It is worth mentioning that in terms of analytical convenience, sphere, infinite plate and infinite cylinder are three geometries which are usually looked into, because of the symmetry in their field.

Plasma electron and ion currents, secondary electron and ion currents, backscattered electron current and photoelectric current are modeled using steady state approach.

3.5 Plasma Current Model

Depending on whether a particular kind (polarity) of plasma species is attracted or repelled, plasma current expression can be different.

This section derives analytic expression [26], [27] for flux of particles repelled by the polarity of the space object in low Earth and geosynchronous orbits.

Let us consider a 1D system of particles as shown in Figure 1. Let n be the number of particles per unit length. For any particular speed v and a time span t , only the particles within a distance of vt from the wall will be able to reach it. Thus, if \bar{v} represents the mean speed, then the average number of particles reaching the wall in a time span of t is given as,

$$N_r = (\text{strike radius}) \left(\frac{\text{linear density}}{2} \right) = \bar{v}t \cdot \frac{n}{2} \quad (13)$$

And the particle strike rate is given as,

$$\frac{N_r}{t} = \frac{\bar{v}n}{2}$$

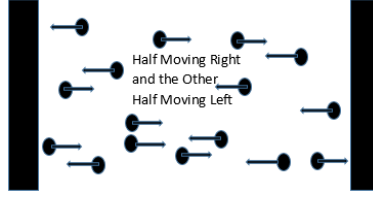


Figure 1. 1D System of Particles Hitting a Wall [27]

This idea can be extended to 3D. Let $f(\vec{v})$ be the probability density function for velocity of particles, then the mean number of particles per unit volume between velocities \vec{v} and $\vec{v} + d\vec{v}$ is given by $f(\vec{v})d^3v = f(\vec{v}) \sin \theta d\theta d\psi v^2 dv$, where v is velocity magnitude and θ, ψ represent polar coordinates.

With reference to Figure 2, number of particles having velocity \vec{v} reaching the elemental area A in time span t can be written as,

$$\tilde{N}_r = (\text{No. per unit volume})(\text{volume of slanted cylinder}) = [f(\vec{v})d^3v][Avt \cos \theta] \quad (14)$$

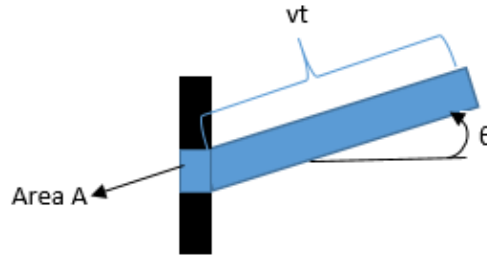


Figure 2. Side View of Wall Area A Being Hit by Particles [27]

Number of particles hitting wall per unit area per unit time with velocity \vec{v} is,

$$\frac{\tilde{N}_r}{At} = f(\vec{v})d^3v v \cos \theta$$

To obtain the flux ϕ_0 , the above expression needs to be integrated over all velocity ranges,

$$\phi_0 = \int f(\vec{v})v \cos \theta d^3v \quad (15)$$

$$\phi_0 = \int \int \int f(\vec{v})v \cos \theta \sin \theta d\theta d\psi v^2 dv \quad (16)$$

$$\phi_0 = \int v^3 f(\vec{v})dv \cdot \frac{1}{2} \int_0^{\frac{\pi}{2}} \sin 2\theta d\theta \cdot \int_0^{2\pi} d\psi \quad (17)$$

$$\phi_0 = \pi \int v^3 f(\vec{v})dv \quad (18)$$

If the particles follow Maxwell-Boltzmann distribution, then the plasma velocity distribution, $f(\vec{v})$ and the plasma speed distribution, $F(v)$ are given as,

$$f(\vec{v}) = n \left(\frac{m}{2\pi kT} \right)^{\frac{3}{2}} e^{-\frac{mv^2}{2kT}} \quad (19)$$

$$F(v) = 4\pi n \left(\frac{m}{2\pi kT} \right)^{\frac{3}{2}} v^2 e^{-\frac{mv^2}{2kT}} \quad (20)$$

where n , m , k , T represent particle number density, particle mass, Boltzmann constant and plasma distribution temperature, respectively.

Using Equations (19), (20), the flux in Equation (18) can then be written in terms of distribution function as,

$$\phi_0 = \frac{\pi n}{4\pi} \cdot \frac{1}{n} \int v F(v) dv \quad (21)$$

$$\phi_0 = \frac{n\bar{v}}{4} \quad (22)$$

$$\phi_0 = \frac{n}{4} \sqrt{\frac{8kT}{\pi m}} = n \sqrt{\frac{kT}{2\pi m}} \quad (23)$$

where \bar{v} is mean speed. When the spacecraft is charged to potential V , the probability distribution changes from $f(E)$ to $f(E + qV)$ [7], where q is particle charge and E is particle energy. Thus, the flux is given as,

$$\phi = \int \int \int n \left(\frac{m}{2\pi kT} \right)^{\frac{3}{2}} e^{-\frac{m(v^2 + \frac{2qV}{m})}{2kT}} v^3 \frac{1}{2} \sin 2\theta d\theta d\psi dv \quad (24)$$

$$\phi = e^{-\frac{qV}{kT}} \phi_0 \quad (25)$$

where ϕ_0 is the flux obtained earlier in Equation (23) in absence of spacecraft charging.

The current density to an uncharged body can be written in terms of flux as,

$$J_0 = q\phi_0 = nq \sqrt{\frac{kT}{2\pi m}} = \frac{1}{2} nq \sqrt{\frac{2kT}{\pi m}} \quad (26)$$

and the current density to a body charged to a potential V is given as,

$$J = q\phi = e^{-\frac{qV}{kT}} q\phi_0 = e^{-\frac{qV}{kT}} J_0 \quad (27)$$

It is to be noted again that the above derivation is based on the assumption that the plasma particles follow Maxwell-Boltzmann distribution under thermal equilibrium condition. The assumption is usually valid for calm environment. In actuality, no single distribution can accurately model the plasma particles because of various disturbances.

The flux for particles can be discriminated by the attracted by debris polarity. In the geosynchronous region, where the plasma density is low, the incoming current density collected by a perfectly absorbing spherical or infinitely long cylindrical body from a collisionless, stationary, isotropic plasma is limited by the particles' orbital angular momenta. This current is known as orbit-limited current [28]. For orbit-limited sphere, for an attracted particle approaching the body from infinity, conservation of energy and angular momentum results in,

$$\frac{1}{2}mv_0^2 = \frac{1}{2}mv(r_s)^2 + qV(r_s) \quad (28)$$

$$mR_1v_0 = mr_sv(r_s) \quad (29)$$

where v_0 is velocity in ambient medium, v is velocity at object surface, R_1 is impact parameter, V is body potential and r_s is object radius. Only particles having radius less than R_1 will reach r_s . Manipulations of Equations (28) and (29) would produce,

$$\frac{1}{2}mv_0^2 = \frac{1}{2}m\left(\frac{R_1v_0}{r_s}\right)^2 + \frac{2q}{m}V(r_s) \quad (30)$$

$$R_1^2 = r_s^2 \left(1 - \frac{2qV(r_s)}{mv_0^2}\right) \quad (31)$$

$(R_1 - r_s)$ is equivalent to the sheath thickness and is also the size of the region from which particles can be drawn. Total current density striking the debris surface is given as,

$$J(V) = \frac{I}{4\pi r_s^2} \quad (32)$$

$$J(V) = \frac{I(1 - \frac{2qV(r_s)}{mv_0^2})}{4\pi R_1^2} \quad (33)$$

$$J(V) = J_0(1 - \frac{2qV(r_s)}{mv_0^2}) \quad (34)$$

$$J(V) = J_0(1 - \frac{qV}{kT}) \quad (35)$$

where I is the total current to spherical debris equal to the ambient current that would pass through an area $4\pi R_1^2$. J_0 is ambient current density outside the sheath and equals to $\frac{I}{4\pi R_1^2}$. J_0 is given by Equation (26). The current derived in this section is called “thick-sheath, orbit-limited” current relation.

In the derivation of Equation (35), velocity of the body is not taken into consideration i.e., it is assumed that the body is at rest compared to plasma velocities. At geosynchronous altitudes, plasma energy is high. The average kinetic energy of particles is much larger than the orbital speed and the body is essentially at rest compared to plasma particles and hence Equation (35) is valid.

At low Earth orbit regime, body gets negatively charged i.e., ion is the attracted species. However, at low Earth orbit, the plasma sheath is thin such that thick sheath theories do not apply here. Also, the orbital velocity is larger than the average kinetic energy of ions. Hence, Equation (35) becomes invalid for ions in low Earth orbits.

For low Earth orbits, as ions are relatively at rest, they are assumed to be ramming into debris surface and the ion current is approximately given as,

$$I = en_i V_{sc} A_i \quad (36)$$

where e is elementary charge, n_i is free plasma ion density, V_{sc} is inertial debris velocity and A_i is projected ion collection area. For sphere of radius R_s ,

$$A_i = \left(\frac{1}{4}\right)(4\pi R_s^2) \quad (37)$$

The plasma electron and ion currents to a sphere of radius R_s are summarized in Table 1.

Table 1. Table Summarizing Plasma Currents

Orbit Region	Plasma Current (Species is Repulsed)	Plasma Current (Species is Attracted)
LEO	$\left(e^{-\frac{qV}{kT}}\right) \left(\frac{1}{2} nq \sqrt{\frac{2kT}{\pi m}}\right) (4\pi R_s^2)$	$qnV_{sc}(\pi R_s^2)$
GEO	$\left(e^{-\frac{qV}{kT}}\right) \left(\frac{1}{2} nq \sqrt{\frac{2kT}{\pi m}}\right) (4\pi R_s^2)$	$\left(1 - \frac{qV}{kT}\right) \left(\frac{1}{2} nq \sqrt{\frac{2kT}{\pi m}}\right) (4\pi R_s^2)$

It is to be noted in Table 1 that a debris in LEO always gets negatively charged and hence the ion automatically qualifies as attracted species.

A quick and approximate method to validate charging level in low Earth orbits is sometimes given by the so-called Anderson's voltage expression. According to Philip C. Anderson [6], at equilibrium, voltage expression is given as,

$$V_{eq} = -\frac{KT_e}{e} \ln \left(\left(\frac{A_e}{A_i} \right) \left(\frac{KT_e}{2\pi m_e v_{sp}^2} \right)^{\frac{1}{2}} \right) \quad (38)$$

where K is Boltzmann constant, T_e is plasma temperature, e is elementary charge, A_e is current collection area for electrons, A_i is current collection area for ions, m_e is mass of electron and v_{sp} is speed of debris. Given below is a quick derivation of Anderson's formula.

Anderson approximated plasma ion current as,

$$J_i = en_i v_{sp} \quad (39)$$

where J_i is ion current density, e is elementary charge, n_i is ion density and v_{sp} is debris speed. Here, it is assumed that ion is having unit elementary charge and ions are relatively stationary w.r.t debris. Assuming the presence of only electron and ion plasma currents, at equilibrium,

$$\text{Electron current} = \text{Ion current} \quad (40)$$

$$J_e A_e = J_i A_i \quad (41)$$

$$e^{\frac{eV_{eq}}{kT}} J_0 A_e = J_i A_i \quad (42)$$

$$\frac{1}{2} e n_e \sqrt{\frac{2kT_e}{\pi m_e}} e^{\frac{eV_{eq}}{kT}} A_e = e n_i v_{sp} A_i \quad (43)$$

$$e^{\frac{eV_{eq}}{kT}} = \frac{A_i}{A_e} \cdot 2v_{sp} \cdot \sqrt{\frac{\pi m_e}{2kT_e}} \quad (\text{assuming } n_e = n_i) \quad (44)$$

$$V_{eq} = -\frac{KT_e}{e} \ln \left(\left(\frac{A_e}{A_i} \right) \left(\frac{KT_e}{2\pi m_e v_{sp}^2} \right)^{\frac{1}{2}} \right) \quad (45)$$

Equation (38) should be used with caution for it is valid only in ionosphere, and that too approximately. But Anderson's formula acts as good means to roughly validate results for low Earth orbit propagations, specifically when debris is in shadow. Approximating a geosynchronous orbit with Anderson's formula would result in highly inaccurate results because Anderson neglected photo-electric current and secondary electron current, which are significant in GEO. Table 2 argues out the reasons for exercising restraint in use of Equation (38) in full detail.

Table 2. Arguments Against Anderson's Voltage Formulation

Assumptions	Arguments
Ion density (n_i) = electron density (n_e)	The more correct assumption should be neutrality of charge, so $n_i = n_e$ assumption should be valid only when charging scenario involves electrons and a single monovalent ion species. In reality, there are more than one kind of ion species, and they may be multi-valent
Ions are essentially stationary w.r.t debris. Mathematically, $\vec{V}_{particles/sc} = \vec{V}_{particles} - \vec{V}_{sc} \approx -\vec{V}_{sc}$	Since magnitude of ion velocity is usually of the order of 1.2 Km/s or less in LEO, whereas typical spacecraft velocity magnitude in low Earth orbit can be 7.8 Km/s, this assumption will hold quite good in LEO. This assumption, however, will not hold good for geostationary orbit, because in geostationary orbit, spacecraft velocity magnitude is about 3 Km/s and ion velocity magnitude can be much more than 1.2 Km/s as there would be more high energy ions in GEO as compared to LEO
Body has negative potential	This assumption again holds good for low altitudes. At high altitude, photoelectron current often exceeds plasma currents, resulting in net positively charged body
Effect of negative potential on ion collection is neglected	This assumption would not be so accurate because it can be seen from Whipple [28] that body potential indeed effects ion current, especially the accuracy of this assumption would be poor in GEO
Ignored secondary current, backscattered current and photoelectric current	These currents cannot be neglected as insignificant, especially the photoelectric current in GEO

3.6 Secondary Electron Current Model

Expression for secondary electron current can be found out using yield i.e., number of secondary electrons generated per incident projectile particle. Yield expressions can be multiplied with incident plasma ion and electron currents to find the value of secondary electron current. The secondary electron currents due to hitting ions and electrons are given as,

$$I_{sec_i} = (< \Delta_i >) I_i \quad (46)$$

$$I_{sec_e} = (< \Delta_e >) I_e \quad (47)$$

where the subscript i and e denote hitting particles as ions and electrons, respectively. I_i and I_e represent plasma ion and electron currents, respectively and their expressions can be obtained from Table 1. It will be assumed that all the incident electrons and ions get absorbed and contribute to secondary electron emission process. The $\langle \rangle$ symbol signifies averaged yield value, averaged over all energies, and is given as,

$$\langle \Delta \rangle = \frac{\int_{E_l}^{E_u} E f(E) \Delta(E) dE}{\int_{E_l}^{E_u} E f(E) dE} \quad (48)$$

where E represents energy, $f(E)$ represents the Maxwell-Boltzmann distribution function representing incoming electrons or ions. The integral limits E_l and E_u in Equation (48) represent lower and upper energy bounds of the impacting particles. In absence of precise information, E_l and E_u are taken as 0 and ∞ , respectively. $\Delta(E)$ represents the secondary electron yield corresponding to the particular energy E of the impacting particle. $f(E)$ is given as,

$$f(E) = n \left(\frac{m}{2\pi kT} \right)^{\frac{1}{2}} e^{-\frac{E}{kT}} \quad (49)$$

It may be argued that in LEO, ions simply ram into the objects, thereby rendering the incoming ions far from following Maxwell-Boltzmann distribution. However, the energies of ions and electrons in LEO are too small to incite any secondary emission. The minimum energy requirement for secondary emission can be computed using $\Delta(E)$.

The secondary electron yield derived is taken from Sternglass [29]. At depth x of the substrate, low-energy secondary electrons are generated in two major ways – 1) produced directly by interaction with incoming projectile 2) produced by fast δ rays. δ rays are energetic electrons (induced by energy transfer from the primary projectile) that go and hit other electrons and atoms to form secondaries.

Let $n_{se}^{(1)}$ and $n_{se}^{(2)}$ denote the number of secondary electrons produced per unit distance at depth x due to direct interaction and fast δ rays respectively. Let \bar{E}_0 be the mean energy loss per secondary formed. Let $\langle \frac{dE_i}{dx} \rangle_{av}^{(1)}$ be the mean energy loss per unit distance going directly into secondary formation. Therefore,

$$n_{se}^{(1)}(v_i, x) = \frac{1}{\bar{E}_0} \langle \frac{dE_i}{dx} \rangle_{av}^{(1)} \quad (50)$$

$$n_{se}^{(2)}(v_i, x) = f(v_i, x) \frac{1}{\bar{E}_0} \langle \frac{dE_i}{dx} \rangle_{av}^{(2)} \quad (51)$$

where $\langle \frac{dE_i}{dx} \rangle_{av}^{(2)}$ is the energy loss per unit length going into the formation of δ rays, and $f(v_i, x)$ is a factor that represents the fraction of $\langle \frac{dE_i}{dx} \rangle_{av}^{(2)}$ available for formation of secondaries in higher order collisions at depth x. According to Sternglass,

$$\langle \frac{dE_i}{dx} \rangle_{av}^{(1)} = \langle \frac{dE_i}{dx} \rangle_{av}^{(2)} = \frac{1}{2} \langle \frac{dE_i}{dx} \rangle_{av} \quad (52)$$

where $\langle \frac{dE_i}{dx} \rangle_{av}$ is the total energy loss per unit length.

$$n_{se}(v, x) = \left(\frac{1}{\bar{E}_0}\right) \left(\frac{1}{2}\right) \langle \frac{dE_i}{dx} \rangle_{av} [1 + f(v_i, x)] \quad (53)$$

According to Bohr,

$$\langle \frac{dE_i}{dx} \rangle_{av} = \frac{2\pi N \epsilon^4 z_i^2}{E_{eq}} \sum_{n,l} z_{n,l} \ln\left(\frac{4E_{eq}}{I_{n,l}}\right) \quad (54)$$

where,

$$E_{eq} = \frac{1}{2} m_0 v_i^2 = \left(\frac{m_0}{M}\right) E_i \quad (55)$$

N is the number of atoms per unit volume, ϵ is electronic charge, z_i is charge of incident particle, M is mass of incident particle, E_i is energy of incident particle, v_i is velocity of incident particle, $z_{n,l}$ is number of electrons in n,l shell and $I_{n,l}$ is binding energy of these electrons. The summation is to be taken over all shells for which logarithm remains positive. If the primary velocity is sufficiently high, then Equation (54) takes the following form,

$$\langle \frac{dE_i}{dx} \rangle_{av} = 2\pi N \epsilon^4 z_i^2 \left[\frac{Z}{E_{eq}} \ln\left(\frac{4E_{eq}}{\bar{I}}\right) \right] \quad (56)$$

where \bar{I} is mean excitation potential for the atom, Z is atomic number of substrate atom and $Z \ln(\bar{I}) = \sum_{n,l} z_{n,l} \ln(I_{n,l})$. \bar{E}_0 is approximated as 25eV for solids. The idea of minimum energy required for secondary electron emission stems from Equation (56). In order to ensure that $\langle \frac{dE_i}{dx} \rangle_{av}$ is positive, input inside the natural logarithm function in Equation (56) must be greater than 1 words, E_{eq} must be greater than $\frac{\bar{I}}{4}$.

A secondary electron formed at depth x below the surface will have certain probability P(x) of reaching the substrate surface and escaping. P(x) can be given as,

$$P(x) = \tau A e^{-\frac{x}{L_s}} \quad (57)$$

where τ is surface transmission coefficient, representing the probability that an electron arriving at the surface from the interior will be able to escape. A is a constant determined by the distribution of initial velocities of secondaries and by the ratio $\frac{\lambda_{sa}}{\lambda_{sc}} = \bar{n}_c$, where λ_{sa} is mean free path for absorption, λ_{sc} is mean free path for inelastic collisions. For a symmetrical distribution of initial directions about a plane parallel to the surface, A has an approximate value of .6. L_s appearing in Equation (57) is given as,

$$L_s = \left(\frac{1}{3} \lambda_{sa} \lambda_{sc}\right)^{\frac{1}{2}} \quad (58)$$

$$L_s = \left(\frac{1}{3} \bar{n}_c\right)^{\frac{1}{2}} \lambda_{sc} \quad (59)$$

The mean free path for inelastic collisions, λ_{sc} is given as,

$$\lambda_{sc} = (N \sigma_{sc})^{-1} \quad (60)$$

where σ_{sc} is the cross-section for secondary electron scattering, and is given as,

$$\sigma_{sc} = \alpha \sigma_g \quad (61)$$

where σ_g is geometrical area of the outermost filled electron shells as determined by covalent radii and α is some constant. σ_g is approximately given as,

$$\sigma_g = 1.6Z^{\frac{1}{3}} \times 10^{-16} \quad (62)$$

where Z represents atomic number of the target. Using Equations (60), (61) in Equation (59),

$$L_s = \left(\frac{1}{3}\bar{n}_c\right)^{\frac{1}{2}}(N\alpha\sigma_g)^{-1} = (\alpha'N\sigma_g)^{-1} \quad (63)$$

where $\alpha' = \left(\frac{3}{\bar{n}_c}\right)^{\frac{1}{2}}\alpha$. If the assumption that the solid may be treated as a collection of free atoms is valid, α' should have closely the same values for all metals. α' is assumed to be .23 [29]. Surface transmission coefficient τ appearing in Equation (57), in case of isotropic distribution of electron velocities approaching a uniform surface potential barrier, is given as,

$$\tau = 1 - \left(\frac{\phi_D}{\bar{E}_s + \phi_D}\right)^{\frac{1}{2}} \quad (64)$$

where \bar{E}_s is energy of the secondary as measured relative to zero vacuum level outside the metal. Typical values of \bar{E}_s lies in the range of 6 eV to 8 eV. Also, for monovalent metals, typical values of ϕ_D lies in the range of .1 eV and .5 eV. Thus, it can be seen that τ lies in the range of .8 and .9. This makes $\tau A \approx .5$, and hence,

$$P(x) \approx .5e^{-\frac{x}{L_s}} \quad (65)$$

Yield, Δ is defined as as the number of secondary electrons escaping from the surface per incident ion. The yield from a thin layer of width dx located at depth x is given as,

$$d\Delta = n_{se}(v_i, x)P(x)dx \quad (66)$$

$$\Delta = \int_0^\infty \frac{1}{2} \frac{1}{\bar{E}_0} \left\langle \frac{dE_i}{dx} \right\rangle_{Av} [1 + f(v_i, x)] \tau A e^{-\frac{x}{L_s}} dx \quad (67)$$

When the atomic number of substrate is small ($Z < 30$),

$$f(v_i, x) = 1 - e^{-\frac{x}{L_\delta(v_i)}} \quad (68)$$

where $L_\delta(v_i)$ is effective penetration distance of δ rays. Substituting Equation (68) into Equation (67), and recalling that $\left\langle \frac{dE_i}{dx} \right\rangle_{Av}$ may be taken as constant over a surface region of width large compared to L_s ,

$$\Delta = \frac{1}{2} \frac{1}{\bar{E}_0} \left\langle \frac{dE_i}{dx} \right\rangle_{Av} \tau A L_s (1 + F(v_i)) \quad (69)$$

$$F(v_i) = \left(1 + \frac{L_\delta}{L_s}\right)^{-1} \quad (70)$$

For heavier elements ($Z \geq 30$), more accurate expression for $f(v_i, x)$ results in,

$$\Delta = \frac{1}{2} \frac{1}{\bar{E}_0} \left\langle \frac{dE_i}{dx} \right\rangle_{Av} \tau A L_s (1 + \bar{F}(v_i)) \quad (71)$$

$$\bar{F}(v_i) = \left(\left(1 + \frac{L_\delta}{L_s} \right)^{-1} + \frac{L_{\delta'}}{L_\delta} \right) \left(1 + \frac{L_{\delta'}}{L_\delta} \right)^{-1} \quad (72)$$

It has been found that [29],

$$\frac{L_\delta(v_i)}{L_s} \approx \frac{E_{eq}}{100} \quad (73)$$

where E_{eq} is expressed in electronvolts. Experimental values for the ratio $\frac{L_{\delta'}}{L_\delta}$ range typically from .05 for aluminium to .25 for gold [29]. A linear variation of this quantity with atomic number will be assumed, i.e.,

$$\frac{L_{\delta'}}{L_\delta} = .05 + \left[\frac{.25 - .05}{79 - 13} \right] (Z - 13) \quad (74)$$

It is to be noted carefully that the formulations are made assuming centimeter-gram-second (CGS) system of units. Appropriate unit conversions must be applied so as not to run into unnecessary errors.

3.7 Backscattering Current Model

Backscattering current can be obtained with the help of backscattering yield i.e. number of backscattered particles per incident particle. The backscattering of electrons is more important than the backscattering of ions. Backscattering yield is usually much smaller compared to secondary yield. Backscattering electron current is given as,

$$I_{bsc} = rI_e \quad (75)$$

where r represents backscattering yield and I_e represents plasma electron current, which can be obtained from Table 1. One might be wondering why averaged value is not considered for backscattering yield. The fact is, as will be seen in next section, according to the model chosen, backscattering yield comes out to be constant for a particular material i.e., $\langle r \rangle = r$.

There are two models which Archard [30] used for explaining backscattering. Neither of these two models single-handedly explains the backscattering, but a combination of the two explains the backscattering over entire atomic number range.

In the diffusion model, it is assumed that electrons travel straight into the target up to a certain specified distance, after which they diffuse evenly in all directions. This model assumes that an electron exhibits completely random motion after multiple collisions. It ignores the possibility of an electron undergoing large single elastic reflections between the surface and the depth of complete diffusion.

In the elastic collision model [31], it is assumed that electrons travel straight into the target suffering retardation according to Thomson-Whiddington law. In addition, the electrons undergo elastic collisions in accordance with Rutherford's law of scattering. This model acknowledges the presence of electrons that are elastically scattered through large angles, but ignores the diffusion effect of multiple collisions. All electrons that are not turned through more than a right angle are assumed not to have turned at all.

“Depth of complete diffusion” is the depth at which the average cosine between actual direction of motion and direction of primary beam becomes $\frac{1}{e}$ or, the angle becomes 68.4° . Corresponding to this, a critical energy E_d exists such that,

$$\int_{E_d}^{E_0} \frac{dE}{\lambda \left| \frac{dE}{dx} \right|} = \frac{1}{2} \quad (76)$$

$$\frac{1}{\lambda} = \frac{\pi N e^4 Z^2}{2E^2} \ln \frac{2a_H m \left(\frac{2E}{m} \right)^{\frac{1}{2}}}{\hbar Z^{\frac{1}{3}}} \quad (77)$$

where N is number of atoms per cubic centimeter, e is electronic charge, m is electronic mass, $\hbar = \frac{h}{2\pi}$ is reduced Plank's constant, Z is atomic number of target, a_H is Bohr hydrogen radius $= 5.2917721092 \times 10^{-11}$ m, E_0 is initial energy.

From Bethe's stopping power theory,

$$\frac{dE}{dx} = 2\pi N e^4 Z \frac{\ln\left(\frac{2E}{J}\right)}{E} \quad (78)$$

where $J = 11.5Z$ (eV) is approximate mean excitation energy. Substitution of Equations (77), (78) into Equation (76) results in,

$$\int_{E_d}^{E_0} \frac{\pi N e^4 Z^2}{2E^2} \ln\left(\frac{2a_H m \left(\frac{2E}{m} \right)^{\frac{1}{2}}}{\hbar Z^{\frac{1}{3}}}\right) \frac{E dE}{2\pi N e^4 Z \ln\left(\frac{2E}{J}\right)} = \frac{1}{2} \quad (79)$$

Applying change of variables $V = \frac{E}{e}$ from Energy E to voltage V ,

$$\int_{V_d}^{V_0} \frac{Z}{2(eV)^2} \frac{(eV) e dV}{2 \ln\left(\frac{2eV}{11.5Z}\right)} \ln\left(\frac{2a_H m \left(\frac{2eV}{m} \right)^{\frac{1}{2}}}{\hbar Z^{\frac{1}{3}}}\right) \frac{eV e dV}{2\pi N e^4 Z \ln\left(\frac{2eV}{11.5Z}\right)} = \frac{1}{2} \quad (80)$$

$$\int_{V_d}^{V_0} \frac{Z}{4V} \frac{\ln(.5418V^{\frac{1}{2}}Z^{-\frac{1}{3}})}{\ln(.1739VZ^{-1})} dV = \frac{1}{20} \quad (81)$$

The ratio of logarithms in Equation (81), according to Archard [30], remains constant between 5 KV and 50 KV and is approximately taken by Archard as .7. However, this does not always hold true. As a better approximation to this, it can be assumed that the logarithmic ratio is .7 for energy between 5kV and 100 kV, and the ratio is .6 for higher energies.

Proceeding forward with the assumption of ratio as .7 (.6 assumption follows the same procedure), Equation (81) results in,

$$Z \ln\left(\frac{V_0}{V_d}\right) = \frac{20}{7} \quad (82)$$

On substituting $V = \frac{E}{e}$ in Bethe's stopping power formula,

$$\frac{dE}{dx} = 2\pi N e^4 Z \frac{\ln\left(\frac{2E}{J}\right)}{E} \quad (83)$$

$$e \frac{dV}{dx} = \frac{2\pi N e^3 Z}{V} \ln\left(\frac{2V}{11.5Z}\right) \quad (84)$$

Integration of Equation (84) leads to,

$$x = \frac{7.68 \times 10^{12}}{NZ} (V_0^2 F(V_0) - V^2 F(V)) \quad (85)$$

where x is in centimeters, N is number of substrate atoms per cubic centimeter, V_0 is initial voltage in volts and the function F is defined as follows,

$$F(V) = \frac{1}{y} \left(1 + \frac{1}{y} + \frac{2!}{y^2} + \dots\right) \quad (86)$$

$$y = 2 \ln\left(\frac{.174V}{Z}\right) \quad (87)$$

Now,

$$N = \frac{\rho N_A}{A} \quad (88)$$

where ρ is target density in gm/cc, N_A is Avogadro's number, A is atomic weight in gram/mole. Substituting Equation (88) in Equation (85) results in,

$$\rho x = \frac{7.68 \times 10^{12} \times A}{NAZ} (V_0^2 F(V_0) - V^2 F(V)) \quad (89)$$

Assuming electrons come to rest when $F(V)=0$,

$$\rho x_R = \frac{7.68 \times 10^{12} V_0^2 \times A}{NAZ} F(V_0) \quad (90)$$

where, x_R denotes full range. The ratio of depth of complete diffusion to full range can be written as,

$$\frac{x_d}{x_R} = \frac{V_0^2 F(V_0) - V_d^2 F(V_d)}{V_0^2 F(V_0)} \quad (91)$$

$$\frac{x_d}{x_R} = 1 - \left(\frac{V_d}{V_0}\right)^2 \frac{F(V_d)}{F(V_0)} \quad (92)$$

$$\frac{x_d}{x_R} = 1 - \left(\frac{V_d}{V_0}\right)^2 \left(\frac{\frac{1}{2 \ln\left(\frac{.174V_d}{Z}\right)} \left(1 + \frac{1}{y_d} + \frac{2!}{y_d^2} + \dots\right)}{\frac{1}{2 \ln\left(\frac{.174V_0}{Z}\right)} \left(1 + \frac{1}{y_0} + \frac{2!}{y_0^2} + \dots\right)} \right) \quad (93)$$

As per Archard,

$$\frac{\frac{1}{2 \ln\left(\frac{.174V_d}{Z}\right)} \left(1 + \frac{1}{y_d} + \frac{2!}{y_d^2} + \dots\right)}{\frac{1}{2 \ln\left(\frac{.174V_0}{Z}\right)} \left(1 + \frac{1}{y_0} + \frac{2!}{y_0^2} + \dots\right)} \approx 1 \quad (94)$$

Using the approximation given by Equation (94) in Equation (93),

$$\frac{x_d}{x_R} \approx 1 - \left(\frac{V_d}{V_0}\right)^2 \quad (95)$$

$$\frac{x_d}{x_R} = 1 - e^{-\frac{40}{7Z}} \quad \left[\text{since } Z \ln\left(\frac{V_0}{V_d}\right) = \frac{20}{7} \right] \quad (96)$$

$$\frac{x_d}{x_R} \approx 1 - \left(1 + \left(-\frac{40}{7Z}\right)\right) \quad (\text{first order approximation}) \quad (97)$$

$$\frac{x_d}{x_R} = \frac{40}{7Z} \quad (98)$$

With the assumption that electrons move equally in all directions from the depth of complete diffusion in such a manner that the overall path length equals full range, it can be easily seen from Figure 3 that only electrons within solid angle 2θ will escape.

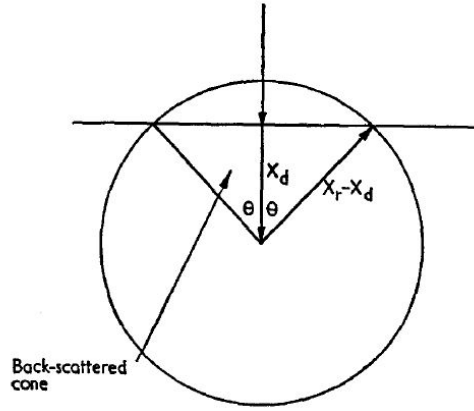


Figure 3. Backscatter Cone [30]

The backscattering coefficient/yield R is given as,

$$R = \frac{\text{Solid angle formed by semiangle } \theta}{\text{total solid angle}} \quad (99)$$

$$R = \frac{2\pi(1 - \cos \theta)}{4\pi} \quad (100)$$

$$R = \frac{1 - \left(\frac{x_d}{x_r - x_d}\right)}{2} \quad (101)$$

$$R = \frac{7Z - 80}{14Z - 80} \quad \left(\text{since } \frac{x_d}{x_R} = \frac{40}{7Z}\right) \quad (102)$$

From Equation (102), it can be seen that R is zero for $Z < 12$ (as R cannot be negative). In fact, for low Z ($Z \leq 11$), experimental value does not match with theoretical value zero. This is because, as Z decreases, the ratio $\frac{x_d}{x_R}$ increases i.e., electrons travel a large part of their range before diffusion sets in. Hence, there is significant time for other neglected phenomenon of large single elastic collisions to take place.

Backscattering Yield from Elastic Collision Model According to Thomson-Whiddington law, if v is the electron velocity and x is the distance traveled in the target, then,

$$v^4 = v_0^4 - c\rho x = c\rho(R - x) \quad (103)$$

where v is electron velocity in cm/s, v_0 is initial electron velocity in cm/s, ρ is target density in gm/cc, c is a constant and its value is $5.05 \times 10^{42} \text{ cm}^6 \text{ sec}^4 \text{ g}^{-1}$, R is range of electron in target material in cm and given as $R = \frac{v_0^4}{c\rho}$. Rutherford [31] predicts that if n_0 electrons per S square centimeter are incident on a bare nucleus of charge Ze , the scattered intensity per unit solid angle is given as,

$$P(\phi) = \left(\frac{n_0 Z^2 e^4}{4Sm^2 v^4} \right) \left(\frac{1}{\sin^4(\frac{\phi}{2})} \right) \quad (104)$$

where ϕ is angle of deviation of scattered electrons as shown in Figure 4, e is electronic charge, n_0 is electron density per S sq. cm, m is electronic mass. If a rectangular parallelepiped element having surface area S and thickness dx is considered, then the number of atoms present in the volume element is given as,

$$dN = N_A \cdot \text{moles} \quad (105)$$

$$dN = \frac{N_A \rho S dx}{A} \quad (106)$$

where N_A is Avogadro's number and A is gram atomic weight of the substrate material. Incremental number of electrons at depth y deflected through an angle of $\phi = \pi - \theta$ into the incremental solid angle $d\Omega$ is given as,

$$d_n(y, \theta) = P(\phi) \cdot dN \cdot d\Omega \quad (107)$$

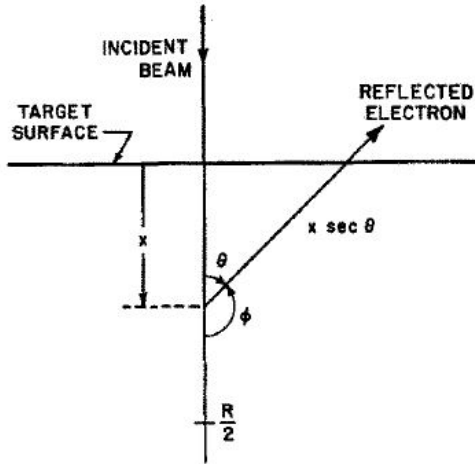


Figure 4. Backscatter Cone, scattered electrons [31]

Substituting the values of $P(\phi)$, dN and $\Omega = 2\pi(1 - \cos\theta)$ or $d\Omega = 2\pi \sin\theta d\theta$ in Equation (107),

$$d_n(y, \theta) = \frac{n_0 Z^2 e^4}{4Sm^2 c\rho(R - x)} \frac{1}{\sin^4 \frac{\phi}{2}} \frac{N_A \rho S dx}{A} 2\pi \sin\theta d\theta \quad (108)$$

On change of variable using $y = \frac{x}{R}$, Equation (108) results in,

$$d_n(y, \theta) = \frac{Z^2 e^4 N_A n_0(y) R(dy) 2\pi \sin \theta d\theta}{4m^2 c A (1-y) \cos^4(\frac{\theta}{2})} \quad (109)$$

Number of electrons incident on a plane at depth y in the target is given as,

$$n_0(y) = n_0 - \int_0^y \int_0^{\frac{\pi}{2}} d_n(y, \theta) \quad (110)$$

It is assumed here that electrons having deflection angle of less than 90° have not deflected at all, and therefore, reflection coefficient r obtained is smaller than experimental value. Using Equation (109) in Equation (110) results in,

$$n_0(y) = n_0 - a \int_0^y \frac{n_0(y)}{1-y} dy \quad (111)$$

where,

$$a = \frac{\pi Z^2 e^4 N_A}{m^2 c A} \quad (112)$$

Equation (111) has the following solution,

$$n_0(y) = n_0 (1-y)^a \quad (113)$$

Incremental backscattering coefficient/yield is given as,

$$dr(y, \theta) = \frac{dn(y, \theta)}{n_0} \quad (114)$$

$$dr(y, \theta) = \frac{a}{2} (1-y)^{a-1} dy \frac{\sin \theta d\theta}{\cos^4(\frac{\theta}{2})} \quad (115)$$

θ is varied from 0 to θ_0 where $x + \frac{x}{\cos \theta_0} = R$ or $y(1 + \sec \theta_0) = 1$, and y is varied from 0 to .5 in integration of Equation (115). The integration results in following expression for backscattering yield,

$$\text{Backscattering Yield, } r = \frac{a - 1 + .5^a}{a + 1} \quad (116)$$

The value of constant 'a' as given by $\frac{\pi Z^2 e^4 N_A}{m^2 c A}$ comes out to be .012. However, Everhart [31] later changed it to .045 to match the experimental results. Archard has given a very nice explanation for this whimsical change of 'a' by Everhart. According to Archard, half the electrons deflected between 0° and 90° will be lost in layers. Let us suppose an electron suffer 45° deflection, it should suffer another 45° deflection in opposite sense to retain original direction. It may also suffer deflection of 45° in same sense and get lost. So, Equation (110) would actually have the following form,

$$n_0(y) = n_0 - \int_0^y \int_0^{\frac{\pi}{2}} d_n(y, \theta) - \frac{1}{2} \int_0^y \int_{\frac{\pi}{2}}^{\frac{3\pi}{4}} d_n(y, \theta) d\theta \quad (117)$$

If the above formulation is used, 'a' comes out to be .041, which is very close to the empirical 'a' of .045 used by Everhart.

At low atomic number (Z), the ratio of depth of complete diffusion x_d to full range x_R is large, such that there is a great chance of large elastic collisions before diffusion sets in, hence elastic collision model is used. For high Z , $\frac{x_d}{x_R}$ is small, so diffusion sets in almost immediately long before any elastic collision may take place, so diffusion model is applicable. In the intermediate region, both models are applicable and a weighted average of both is used. The following piece-wise model can be assumed for a substrate with atomic number Z :

For $Z < 11$,

$$r = \frac{a - 1 + .5^a}{a + 1} \quad (118)$$

For $Z > 60$,

$$r = \frac{7Z - 80}{14Z - 80} \quad (119)$$

For $11 \leq Z \leq 60$

$$r = \frac{x_d}{x_R} \left(\frac{a - 1 + .5^a}{a + 1} \right) + \frac{x_R - x_d}{x_R} \left(\frac{7Z - 80}{14Z - 80} \right) \quad (120)$$

3.8 Photoelectron Current Model

Photoelectron current is one of the significant currents in high altitude orbits like GEO. Photoelectron current density (divided by elementary charge) is given as [7],

$$J_{ph} = \int_0^\infty f_s Y d\omega \quad (121)$$

where f_s is number of photons per unit area per unit time per unit photon energy, and is a function of photon frequency, ω . Y is the yield i.e. number of photoelectrons per incident photon and is a function of ω and angle of incidence, θ . The yield is given as

$$Y[\omega, R(\omega)] = Y^*[\omega, R(\omega, \theta)][1 - R(\omega, \theta)] \quad (122)$$

where R is reflectance and Y^* is yield per absorbed photon, which can be approximated as [7, 32],

$$Y^*[\omega, R(\omega, \theta)] \approx \frac{Y^*[\omega, R(\omega, 0)]}{\cos\theta} \quad (123)$$

Laboratory measurements [7, 33, 34] show,

$$1 - R(\omega, \theta) \approx [1 - R(\omega, 0)]\cos(\theta) \quad (124)$$

Thus, from the product of Y^* and $(1 - R)$, there is no θ dependence of Y . The only incident angle dependence of the photoelectric current stems from the factor $\cos\theta$, which results from effective surface area on which light is incident. Photoelectrons can be assumed to follow Maxwellian distribution for positive body potentials with characteristic temperature ranging 1eV-2eV [7]. The characteristic temperature T_{ph} will be taken as 1.5 eV in our simulations. This leads to:

$$I_{ph} = q_e J_{ph}(0) A \cos\theta \equiv q_e J_{ph}(0) A_\perp \quad \text{if } \phi \leq 0 \quad (125)$$

and,

$$I_{ph} = q_e J_{ph}(0) A_{\perp} e^{-\frac{\phi}{T_{ph}}} \quad \text{if } \phi > 0 \quad (126)$$

where the neutral current density $J_{ph}(0)$ is given as,

$$J_{ph}(0) = \int_0^{\infty} f_s(\omega) Y^*(\omega) [1 - R(\omega)] d\omega \quad (127)$$

where q_e represents elementary charge, A_{\perp} represents projected area of the body and ϕ represents the body potential.

In the following, methods for obtaining quantities appearing in Equation (127) are stated. Number of photons per unit area per unit time per unit photon energy (f_s) will be obtained from Air Mass Zero (AM 0) solar spectral irradiance. Yield per absorbed photon (Y^*) will be obtained using Fowlers method for near-threshold frequencies and assumed constant for higher frequencies. Fowlers yield depends upon absolute body temperature, which will be obtained using thermal equilibrium equation. Reflectance (R) will be obtained using Fresnel's equation. Fresnel's equation depends upon refractive index, which will be computed using Brendel and Bormann model.

AM 0 or ASTM E-490 spectrum provides solar spectral irradiance ($\frac{W}{m^2 nm^{-1}}$) data and is based on data collected from several satellites, space shuttles, high altitude aircrafts, solar telescopes etc. The correctness of the spectrum is validated by scientific communities using the spectral irradiance integration, which should be equal to the accepted value of solar constant i.e. $1366.1 \frac{W}{m^2}$. AM 0 spectrum is shown in Figure 5.

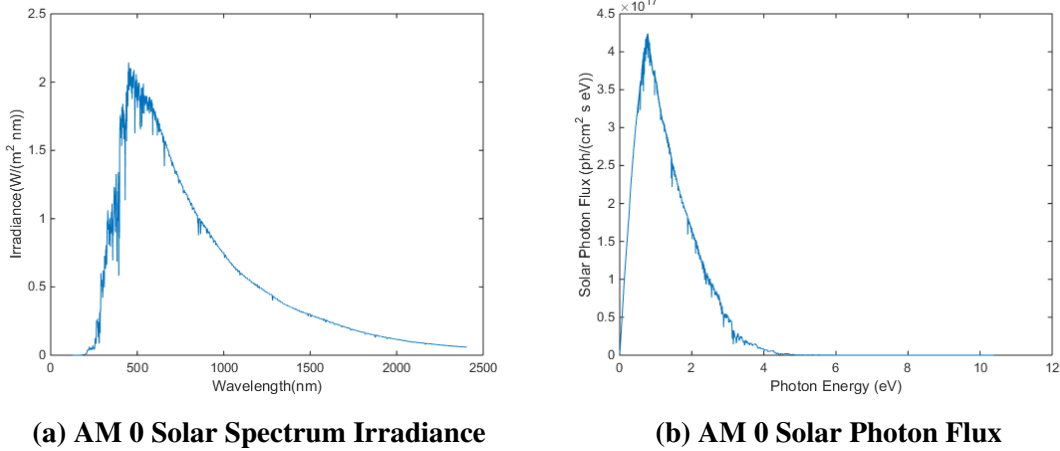


Figure 5. AM 0 Spectrum

If λ_i and λ_f are the initial and final wavelengths of a certain band, then the power received per unit area can be written as,

$$\frac{P}{A} = \int_{\lambda_i}^{\lambda_f} S_{\lambda} d\lambda \quad (128)$$

where S_λ is spectral irradiance (power per unit area per unit wavelength). Then, photon rate per unit area (number of incident photons per unit area per unit time) in that λ range can be written as,

$$Ph_{rate} = \int_{\lambda_i}^{\lambda_f} \frac{S_\lambda}{E} d\lambda \quad (129)$$

where E is energy of a photon having wavelength λ . The photon rate per unit area can also be written in the following form,

$$Ph_{rate} = - \int_{E_i}^{E_f} f_s dE \quad (130)$$

where f_s represents solar photon flux (number of photons per unit area per unit time per unit photon energy). The negative sign is because of the fact that $\lambda_f > \lambda_i \implies E_f < E_i$ and vice versa. Bringing in a change of variables,

$$Ph_{rate} = - \int_{\lambda_i}^{\lambda_f} f_s \frac{dE}{d\lambda} d\lambda \quad (131)$$

Comparison of Equation (129) and Equation (131)

results in,

$$S_\lambda = -f_s E \frac{dE}{d\lambda} \quad (132)$$

Differentiating the energy equation $E = \frac{hc}{\lambda}$, $\frac{dE}{d\lambda} = -\frac{hc}{\lambda^2}$ is obtained, and substituting it in Equation (132) results in,

$$S_\lambda = f_s \frac{(hc)^2}{\lambda^3} \quad \text{or} \quad f_s = \frac{\lambda^3}{(hc)^2} S_\lambda \quad (133)$$

Application of Equation (133) to solar spectrum irradiance data presented in Figure 5a results in the solar photon flux data plot given by Figure 5b.

In the field of quantum statistics, Fermi-Dirac distribution states that for a system of identical fermions, the average number of fermions in a single-particle state i is given as,

$$\bar{n}_i = \frac{1}{e^{(\varepsilon_i - \mu)/(kT)} + 1} \quad (134)$$

where ε_i is the energy of the single-particle state i , μ is total chemical potential, k is Boltzmann constant and T is absolute temperature. The term fermion is used for any particle following Fermi-Dirac distribution. If it is assumed that the electrons in a material follow the Femi-Dirac distribution, then the number of electrons per unit volume with velocity components in the ranges $(u, u+du)$, $(v, v+dv)$, $(w, w+dw)$ (u being normal to the surface and u, v, w forming an orthogonal system) can be written as,

$$n(u, v, w) du dv dw = 2 \left(\frac{m}{h} \right)^3 \frac{du dv dw}{e^{(\frac{1}{2}m(u^2 + v^2 + w^2) - \varepsilon^*)/(kT)} + 1} \quad (135)$$

Here, m is mass of electron, h is Plank's constant and ε^* is fermi energy. k is Boltzmann constant and T is absolute temperature. The particle volumetric density having surface-normal velocities in the range $(u, u+du)$ is given as,

$$\bar{n}(u) du = 2 \left(\frac{m}{h} \right)^3 du \int_0^\infty \int_0^{2\pi} \frac{\rho d\rho d\theta}{e^{(\frac{1}{2}m(u^2 + \rho^2) - \varepsilon^*)/(kT)} + 1} \quad (136)$$

$$\bar{n}(u)du = \frac{4\pi kT}{m} \left(\frac{m}{h}\right)^3 \log(1 + e^{(\epsilon^* - \frac{1}{2}mu^2)/(kT)}) du \quad (137)$$

A new variable χ_0 is introduced such that $\chi_0 = \chi + \epsilon^*$, where χ is the work function. Fowler's derivation [35] is based on the hypothesis that “the photoelectron yield is proportional to the number of electrons per unit volume of the metal whose kinetic energy normal to the surface augmented by photon energy $h\nu$ is sufficient to overcome the potential step at the surface”. Number of such available electrons N_B is given as,

$$N_B = \int_{\frac{1}{2}mu^2 = \chi_0 - h\nu}^{\infty} \bar{n}(u) du \quad (138)$$

With introduction of a new variable, $y = (\frac{1}{2}m\rho^2 - (\chi_0 - h\nu))/(kT)$

$$N_B = \frac{2\pi kT}{m} \left(\frac{2kT}{m}\right)^{\frac{1}{2}} \left(\frac{m}{k}\right)^3 \int_0^{\infty} \frac{\log(1 + e^{-y + (h\nu - \chi)/(kT)})}{(y + (\chi_0 - h\nu)/(kT))^{\frac{1}{2}}} dy \quad (139)$$

When the frequency is near threshold frequency, y is small compared to the term $(\chi_0 - h\nu)/(kT)$, so Fowler neglects the denominator y in Equation (139). This is the single most important assumption of Fowler's theory and it leads to:

$$N_B = \frac{2\sqrt{2}\pi m^{\frac{3}{2}}}{h^3} \frac{k^2 T^2}{(\chi_0 - h\nu)^{\frac{1}{2}}} \int_0^{\infty} \log(1 + e^{-y + (h\nu - \chi)/(kT)}) dy \quad (140)$$

The logarithmic term may be expanded as a series and integrated term-wise to obtain,

$$N_B = \frac{2\sqrt{2}\pi m^{\frac{3}{2}}}{h^3} \frac{k^2 T^2}{(\chi_0 - h\nu)^{\frac{1}{2}}} [e^{\mu} - \frac{e^{2\mu}}{2^2} + \frac{e^{3\mu}}{3^2} - \dots] \quad \text{with } \mu \leq 0 \quad (141)$$

where $\mu = (h\nu - \chi)/(kT)$. When $\mu > 0$,

$$\int_0^{\infty} \log(1 + e^{-y + \mu}) dy = \int_0^{\mu} \log(1 + e^{-y + \mu}) dy + \int_0^{\infty} \log(1 + e^{-y'}) dy' \quad (142)$$

$$\int_0^{\infty} \log(1 + e^{-y + \mu}) dy = \frac{\pi^2}{12} + \frac{1}{2}\mu^2 + \int_0^{\mu} \log(1 + e^{-y''}) dy'' \quad (143)$$

The logarithmic term is expanded, which results in,

$$\int_0^{\infty} \log(1 + e^{-y + \mu}) dy = \frac{\pi^2}{6} + \frac{1}{2}\mu^2 - [e^{-\mu} - \frac{e^{-2\mu}}{2^2} + \frac{e^{-3\mu}}{3^2} - \dots] \quad (144)$$

Therefore,

$$N_B = \frac{2\sqrt{2}\pi m^{\frac{3}{2}}}{h^3} \frac{k^2 T^2}{(\chi_0 - h\nu)^{\frac{1}{2}}} [\frac{\pi^2}{6} + \frac{1}{2}\mu^2 - [e^{-\mu} - \frac{e^{-2\mu}}{2^2} + \frac{e^{-3\mu}}{3^2} - \dots]] \quad (145)$$

It is noteworthy that even when $\mu < 0$, photoemission occurs, because Fowler tries to evaluate a situation where kinetic energy of motion perpendicular to surface plus incident light energy $h\nu$

exceeds the work function. Since Fowler has assumed N_B being proportional to the yield, it can be written,

$$Y^* = K_P \frac{T^2}{(\chi_0 - h\nu)^{\frac{1}{2}}} f\left(\frac{h\nu - \chi}{kT}\right) \quad (146)$$

where K_P is a constant of proportionality. Fowler also assumed that for frequencies near threshold, $(\chi_0 - h\nu)^{\frac{1}{2}}$ is constant. According to Fowler, at $h\nu \approx \chi$, $(\chi_0 - h\nu) \approx \epsilon^*$, so if ν changes by 15%, (with ν_0 of the order of 4 eV and $\chi_0 - h\nu$ of the order of 10 volts), $(\chi_0 - h\nu)$ changes by 6% and $(\chi_0 - h\nu)^{\frac{1}{2}}$ changes by only 3%. This implies approximately a constant $(\chi_0 - h\nu)^{\frac{1}{2}}$. Our upper and lower limit on variation of photon frequency ν from threshold frequency ν_0 would correspond to 3% variation of $(\chi_0 - h\nu)^{\frac{1}{2}}$ from its nominal value $(\chi_0 - \chi)^{\frac{1}{2}}$. Thus,

$$Y^* = K'_P T^2 f(\mu) \quad (147)$$

where K'_P is new constant of proportionality. The function f as previously given is defined as,

$$f(\mu) = e^\mu - \frac{e^{2\mu}}{2^2} + \frac{e^{3\mu}}{3^2} \dots \quad \text{with } \mu \leq 0 \quad (148)$$

and,

$$f(\mu) = \frac{\pi^2}{6} + \frac{1}{2}\mu^2 - (e^{-\mu} - \frac{e^{-2\mu}}{2^2} + \frac{e^{-3\mu}}{3^2} - \dots) \quad \text{with } \mu > 0 \quad (149)$$

The value of constant K'_P has to be found from experimental values of the photoelectric yield. For frequencies that have energy values lower than the proposed 3% range, it will be assumed that there is no photoelectron emission. For all frequencies that have energy values higher than this range, the yield will be taken as constant. This assumption is made using the basic fact of photoelectric effect, “for frequencies greater than threshold frequency, there is no effect of frequency in photoelectric current. But it increases linearly with increase in light intensity. Increasing frequency only leads to increase in kinetic energy of photoelectrons”. As can be seen in Figure 5b, above threshold frequency (4.16 eV for aluminum), intensity is approximately constant, thereby validating the correctness of assumption of constant yield above the proposed 3% range.

Equation (147) requires absolute body temperature, which can be obtained from thermal equilibrium,

$$\text{Heat absorbed} = (1 - a)\pi R^2 S_0 \quad (150)$$

where a is albedo, R is radius of the body and S_0 is solar constant

$$\text{Heat radiated from the body} = (4\pi R^2)\sigma T^4 \quad (151)$$

where σ is Stefan's constant. Under thermal equilibrium condition,

$$(1 - a)\pi R^2 S_0 = (4\pi R^2)\sigma T^4 \quad (152)$$

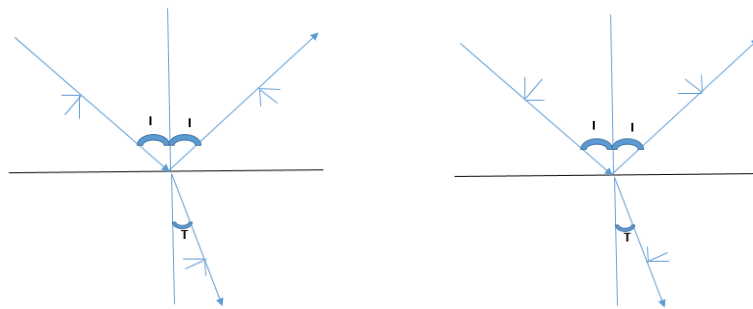
$$T = \left(\frac{(1 - a)S_0}{4\sigma}\right)^{\frac{1}{4}} \quad (153)$$

Albedo is defined as fraction of incident light that is reflected off of the body surface. Reflectance is defined similarly but for a single incidence angle. Thus, albedo is directional integration of reflectance; albedo can be obtained as sum of diffuse and specular reflection components.

An important property closely related to reflectance is reflectivity. Reflectivity is property of a material whereas reflectance is property of a particular sample of that material. Only in case of very thin bodies, reflectance and reflectivity are different. If the body is too thin e.g., of the order of few atoms layer thin, inner atomic layers start reflecting the light as well as the light starts transmitting through the body easily, resulting in different values of reflectance and reflectivity. For thick materials, both reflectance and reflectivity are same. Reflectivity is limiting value of reflectance when your sample is thick. Reflectivity is given as square of magnitude of Fresnel's reflection coefficient. It can be safely assumed that debris is thick and reflectance can be substituted with reflectivity and hence Fresnel's equation can be used.

The expression for Fresnel's equation depends upon the optical properties of the body and the medium in which incident light is present. Although current research deals with air (dielectric) - conductor interface, we will first look at the derivation of Fresnel's equation for dielectric - dielectric interface and see how it relates to Fresnel's equation for dielectric - conductor interface.

Any electric field can be separated into two components, one perpendicular to the plane of Figure (6) and also perpendicular to the direction of light travel, and the other, parallel to the plane of Figure (6) and also perpendicular to the direction of light travel [36]. Figure (6a) corresponds to E_{\perp} (E_{\perp} lies out of the plane of paper and corresponding B_{\parallel} lies in the plane of paper). Similarly, Fig. (6b) corresponds to E_{\parallel} (E_{\parallel} lies in the plane of paper and the corresponding B_{\perp} lies out of the plane of paper). The small lines perpendicular to light travel directions in Figure (6a) correspond to B-fields. Similarly, the small lines perpendicular to light travel directions in Figure (6b) correspond to E fields. All the in-plane field components are divided into their horizontal and vertical components as can be seen in Figures (6a), (6b).



(a) E_{\perp} , B_{\parallel} to Plane of Paper (b) B_{\perp} , E_{\parallel} to Plane of Paper

Figure 6. Electric Field Break Down into Parallel and Perpendicular Directions

Derivation corresponding to Figure (6a) will be first looked at. Since the E-field is parallel to the boundary (boundary is out of the plane of paper), the E-field will just transmit across the boundary

(consequence of Maxwell's third equation) i.e.,

$$E_i + E_r = E_t \quad (154)$$

where the subscripts i, r and t stand for incident ray, reflected ray and transmitted ray, respectively. The horizontal components of B-field in Figure (6a) are also parallel to the boundary and therefore, they will also transmit across the boundary (consequence of Maxwell's fourth equation) i.e.,

$$B_i \cos(I) - B_r \cos(I) = B_t \cos(T) \quad (155)$$

where I stands for angle of incidence, which is same as angle of reflection. T stands for angle of refraction. Using $B = E/v = (n/c)E$, where v is speed of light, n is refractive index and c is speed of light in vacuum in Equation (155) results in,

$$\frac{n_1}{c} E_i \cos(I) - \frac{n_1}{c} E_r \cos(I) = \frac{n_2}{c} E_t \cos(T) \quad (156)$$

where n_1 and n_2 represent refractive indices of incidence medium and refraction medium, respectively.

$$n_1 E_i \cos(I) - n_1 E_r \cos(I) = n_2 E_t \cos(T) \quad (157)$$

Equations (154) and (157) result in,

$$\frac{E_r}{E_i} = \frac{n_1 \cos(I) - n_2 \cos(T)}{n_1 \cos(I) + n_2 \cos(T)} \quad (158)$$

Next part of the derivation corresponds to Figure (6b), where E-field is parallel to the plane of paper. In Figure (6b), B-field is perpendicular to the plane of paper and parallel to the boundary,

$$\text{and hence} \\ B_i + B_r = B_t \quad (159)$$

The horizontal component of E-field is also parallel to the boundary, so it will also transmit across the boundary,

$$E_i \cos(I) - E_r \cos(I) = E_t \cos(T) \quad (160)$$

Using the relation, $B = (n/c)E$ in eq. (159),

$$\frac{n_1}{c} E_i + \frac{n_1}{c} E_r = \frac{n_2}{c} E_t \quad (161)$$

$$n_1 E_i + n_1 E_r = n_2 E_t \quad (162)$$

Equations (160) and (162) result in,

$$\frac{E_r}{E_i} = \frac{n_2 \cos(I) - n_1 \cos(T)}{n_1 \cos(T) + n_2 \cos(I)} \quad (163)$$

If light is assumed to be unpolarized, the reflectivity or reflectance is given as,

$$R = \frac{\left(\frac{E_r}{E_i} \right)_{\perp}^2 + \left(\frac{E_r}{E_i} \right)_{\parallel}^2}{2} \quad (164)$$

Substituting Equations (158), (163) into Equation (164) and using normal incidence, i.e., $I = T = 0$,

$$R = \left(\frac{n_2 - n_1}{n_2 + n_1} \right)^2 \quad (165)$$

Fresnel's equation for dielectric-conductor interface is analogous to dielectric-dielectric case. n_2 in Eqs. (158), (163) needs to be replaced with complex refractive index $(n_2 - ik_2)$, where k_2 is an optical parameter. Fresnel's equation for dielectric-dielectric interface is given as [37],

$$\left. \frac{E_r}{E_i} \right|_{\perp} = \frac{n_1 \cos(I) - (n_2 - ik_2) \cos(T)}{n_1 \cos(I) + (n_2 + ik_2) \cos(T)} \quad (166)$$

$$\left. \frac{E_r}{E_i} \right|_{\parallel} = \frac{(n_2 - ik_2) \cos(I) - n_1 \cos(T)}{n_1 \cos(T) + (n_2 - ik_2) \cos(I)} \quad (167)$$

Based on Eqs. (166), (167), the s-polarized and p-polarized reflectivities are given as [38],

$$R_s = \frac{a^2 + b^2 - 2a \cos I + \cos^2 I}{a^2 + b^2 + 2a \cos I + \cos^2 I} \quad (168)$$

$$R_p = R_s \frac{a^2 + b^2 - 2a \sin I \tan I + \sin^2 I \tan^2 I}{a^2 + b^2 + 2a \sin I \tan I + \sin^2 I \tan^2 I} \quad (169)$$

$$a^2 = \frac{1}{2n_1^2} \left(\sqrt{(n_2^2 - k_2^2 - n_1^2 \sin^2 I)^2 + 4n_2^2 k_2^2} + n_2^2 - k_2^2 - n_1^2 \sin^2 I \right) \quad (170)$$

$$b^2 = \frac{1}{2n_1^2} \left(\sqrt{(n_2^2 - k_2^2 - n_1^2 \sin^2 I)^2 + 4n_2^2 k_2^2} - n_2^2 + k_2^2 + n_1^2 \sin^2 I \right) \quad (171)$$

When angle of incidence is zero, both R_s and R_p take the following form,

$$R_s = R_p = \frac{k_2^2 + (n_1 - n_2)^2}{k_2^2 + (n_1 + n_2)^2} \quad (172)$$

Furthermore, with the assumption of sunlight being unpolarized, reflectance is given as,

$$R = \frac{R_s + R_p}{2} = \frac{k_2^2 + (n_1 - n_2)^2}{k_2^2 + (n_1 + n_2)^2} \quad (173)$$

Fresnel's Eq. (173) requires values of refractive indices n_1 , n_2 and value of optical parameter k_2 . It is safe to assume $n_1 = 1$, which corresponds to vacuum. The objective is to find refractive index of the second medium n_2 as function of light wavelength or frequency.

A case of an electron bound to its nucleus is considered and it is trying to move under the influence of an applied electric field, E [39]. An electric dipole moment is created because of electric field's attempt to separate the electron from its nucleus. The system can be described as,

$$m\ddot{x} = eE - kx - m\gamma\dot{x} \quad (174)$$

where m is mass of electron, e is elementary charge and k is spring constant. It is assumed that electric field is applied in x-direction, ' kx ' models the restoring force arising from attraction of nucleus, $m\gamma\dot{x}$ is sort of a frictional force and it arises from collisions of electrons with other particles.

Resonance frequency is given as $\omega_0 = \sqrt{\frac{k}{m}}$. Eq. (174) can be written as,

$$m\ddot{x} = eE - m\omega_0^2 x - m\gamma\dot{x} \quad (175)$$

$$\ddot{x} + \gamma\dot{x} + \omega_0^2 x = \frac{e}{m}E \quad (176)$$

$\omega_0 = 0$ corresponds to the case of unbound electrons i.e., good conductors and $\omega_0 \neq 0$ corresponds to dielectrics. $\gamma \neq 0$ for both conductors and dielectrics. The electric field can have any functional form, and it will be assumed of the form $E(t) = Ee^{j\omega t}$. Equation (176) has the standard solution $x(t) = xe^{j\omega t}$, where the amplitude x satisfies the relation,

$$-\omega^2 x + j\omega\gamma x + \omega_0^2 x = \frac{e}{m}E \quad (177)$$

$$x = \frac{\frac{e}{m}E}{\omega_0^2 - \omega^2 + j\omega\gamma} \quad (178)$$

The polarization P is given as,

$$P = Np = Nex = \frac{\frac{Ne^2}{m}E}{\omega_0^2 - \omega^2 + j\omega\gamma} \equiv \epsilon_0\chi(\omega)E \quad (179)$$

$$\epsilon_0\chi(\omega) = \frac{\frac{Ne^2}{m}}{\omega_0^2 - \omega^2 + j\omega\gamma} \quad (180)$$

where N is the total number of elementary dipoles per unit volume, ϵ_0 is permittivity of vacuum and $\chi(\omega)$ is electric susceptibility of medium. Now, the electric flux density is given as,

$$D = \epsilon(\omega)E = \epsilon_0 E + P \quad (181)$$

$$\epsilon(\omega)E = \epsilon_0(1 + \chi(\omega))E \quad (182)$$

$$\epsilon(\omega) = \epsilon_0(1 + \chi(\omega)) \quad (183)$$

$$\epsilon(\omega) = \epsilon_0 + \frac{\frac{Ne^2}{m}}{\omega_0^2 - \omega^2 + j\omega\gamma} \quad (184)$$

where $\epsilon(\omega)$ is effective permittivity. Using the definition of 'plasma frequency' as $\omega_p^2 = \frac{Ne^2}{\epsilon_0 m}$ in Equation (184),

$$\epsilon(\omega) = \epsilon_0 + \frac{\epsilon_0\omega_p^2}{\omega_0^2 - \omega^2 + j\omega\gamma} \quad (185)$$

$\epsilon(\omega)$ will have a real part and an imaginary part, so let $\epsilon(\omega) = \epsilon'(\omega) - j\epsilon''(\omega)$. $\epsilon'(\omega)$ is characteristic of refractive properties, whereas $\epsilon''(\omega)$ is characteristic of absorptive properties. On separating Equation (185) into real and imaginary parts,

$$\epsilon'(\omega) = \epsilon_0 + \frac{\epsilon_0\omega_p^2(\omega_0^2 - \omega^2)}{(\omega^2 - \omega_0^2) + \gamma\omega^2} \quad (186)$$

$$\epsilon''(\omega) = \frac{\epsilon\omega_p^2\omega\gamma}{(\omega^2 - \omega_0^2) + \gamma^2\omega^2} \quad (187)$$

Around the resonance frequency ω_0 , ϵ' shows anomalous behaviour and absorption increases substantially. A small detour will be taken here to have a look at the case of dielectric materials as well. Although the focus of this research is conductors, but the development can be used later if dielectric materials are ever taken up for research.

In actual dielectric materials, there exists many resonance frequencies corresponding to various vibrational modes and polarization mechanism and Equation (185) has the form,

$$\epsilon(\omega) = \epsilon_0 + \epsilon_0 \sum_i \frac{N_i e_i^2 / (m_i \epsilon_0)}{\omega_i^2 - \omega^2 + j\omega\gamma_i} \quad (188)$$

More precise application of quantum mechanical models lead to essentially the same equation

$$\epsilon(\omega) = \epsilon_0 + \epsilon_0 \sum_{j>i} \frac{f_{ji}(N_i - N_j)e^2 / (m\epsilon_0)}{\omega_{ji}^2 - \omega^2 + j\omega\gamma_{ji}} \quad (189)$$

where ω_{ji} represents transition frequency between energy levels, N_i and N_j correspond to population of lower and upper energy levels, respectively, f_{ij} are called oscillator strengths. On using the definition of refractive index $n(\omega) = \sqrt{\frac{\epsilon_0(\omega)}{\epsilon_0}}$ in Equation (188),

$$n^2(\omega) = 1 + \sum \frac{B_i \omega_i^2}{\omega_i^2 - \omega^2 + j\omega\gamma_i} \quad (190)$$

where B_i are constants. Usually, the above equation is applied to regions far away from resonance so that $\gamma_i = 0$,

$$n^2(\omega) = 1 + \sum \frac{B_i \omega_i^2}{\omega_i^2 - \omega^2} \quad (191)$$

$$n^2(\omega) = 1 + \sum_i \frac{B_i \lambda^2}{\lambda^2 - \lambda_i^2} \quad (192)$$

This is known as Sellmeier equation and is valid for dielectric materials. The values of the wavelengths corresponding to resonance condition and the constants B_i are obtained experimentally.

For conductors, $\omega_0 = 0$, and thus Equation (185) can be written as,

$$\frac{\epsilon(\omega)}{\epsilon_0} = 1 + \frac{\omega_p^2}{j\omega(\gamma + j\omega)} \quad (193)$$

The above model is referred to as Drude Model. A more detailed modelling using interband terms gives rise to Lorentz-Drude model, according to which the complex dielectric function is given as [41],

$$\hat{\epsilon}_r(\omega) = \frac{\epsilon(\omega)}{\epsilon_0} = \hat{\epsilon}_r^{(f)}(\omega) + \hat{\epsilon}_r^{(b)}(\omega) \quad (194)$$

where $\hat{\epsilon}_r^{(f)}(\omega)$ corresponds to free-electron/Drude model and $\hat{\epsilon}_r^{(b)}(\omega)$ corresponds to interband part or Lorentz model i.e.,

$$\hat{\epsilon}_r^{(f)}(\omega) = 1 - \frac{\Omega_p^2}{\omega(\omega - i\Gamma_0)} \quad (195)$$

$$\hat{\epsilon}_r^{(b)}(\omega) = \sum_{j=1}^l \frac{f_j \omega_p^2}{(\omega_j^2 - \omega^2) + i\omega\Gamma_j} \quad (196)$$

where ω_p is plasma frequency, l is the number of oscillators with frequency ω_j , strength f_j , and lifetime $1/\Gamma_j$, and $\Omega_p = \sqrt{f_0} \omega_p$ is plasma frequency associated with intraband transitions with oscillator strength f_0 and damping constant Γ_0 .

A modified version of classical Lorentz-Drude model is proposed by Brendel and Bormann [40] according to which the complex dielectric function is given as,

$$\hat{\epsilon}_r(\omega) = 1 - \frac{\Omega_p^2}{\omega(\omega - i\Gamma_0)} + \sum_{j=1}^l \chi_j(\omega) \quad (197)$$

$$\chi_j(\omega) = \frac{1}{\sqrt{2\pi}\sigma_j} \int_{-\infty}^{\infty} e^{-\frac{(x-\omega_j)^2}{2\sigma_j^2}} \frac{f_j \omega_p^2}{(x^2 - \omega^2) + i\omega\Gamma_j} dx \quad (198)$$

where $\omega_p = \sqrt{\frac{Ne^2}{\epsilon_0 m}}$ is plasma frequency, with N , e , ϵ_0 , m being number of conduction electrons per unit volume, electronic charge, permittivity of vacuum and electronic mass, respectively. l is the number of oscillators with frequency ω_j , strength f_j , and lifetime $1/\Gamma_j$, and $\Omega_p = \sqrt{f_0} \omega_p$ is plasma frequency associated with intraband transitions with oscillator strength f_0 and damping constant Γ_0 . σ_j is standard deviation associated with the Gaussian modelling of the dielectric function and its value is experimentally obtained. ω is angular frequency of light.

Rakic [41] has given experimental tables for Brendel-Bormann model parameters f_0 , f_j , Γ_0 , Γ_j , ω_j , σ_j for some commonly used materials including the material Aluminum, which is used in this research work.

Analytical solution for $\chi_j(\omega)$ exists and is given as,

$$\chi_j = \frac{if_j \omega_p^2}{2\sqrt{2}a_j \sigma_j} \left(U \left[1/2, 1/2, -\left(\frac{a_j - \omega_j}{\sqrt{2}\sigma_j} \right)^2 \right] + U \left[1/2, 1/2, -\left(\frac{a_j + \omega_j}{\sqrt{2}\sigma_j} \right)^2 \right] \right) \quad (199)$$

Here, U is known as Kummer function of second kind and $U(1/2, 1/2, z^2) = \sqrt{\pi} e^{z^2} \operatorname{erfc}(z)$, where $\operatorname{erfc}(x) = \frac{2}{\sqrt{\pi}} \int_x^{\infty} e^{-t^2} dt$ is the complementary error function. The parameter a_j is given by its real and imaginary parts,

$$a_j = a'_j + ia''_j \quad (200)$$

where,

$$a'_j = \frac{\omega}{\sqrt{2}} \left((1 + (\Gamma_j/\omega)^2)^{1/2} + 1 \right)^{1/2} \quad (201)$$

$$a''_j = \frac{\omega}{\sqrt{2}} \left((1 + (\Gamma_j/\omega)^2)^{1/2} - 1 \right)^{1/2} \quad (202)$$

Now, the complex refractive index is given as,

$$\tilde{n} = n - jk \quad (203)$$

where n is the usual real refractive index. k is extinction coefficient. Now, the square of amplitude of this complex refractive index $(\tilde{n})^2 = (n^2 - k^2) - 2jkn$ is equal to the complex dielectric function.

Thus, if complex dielectric function $\hat{\epsilon}_r(\omega) = \epsilon_{r1} - j\epsilon_{r2}$, then from $\hat{\epsilon}_r(\omega) = (\tilde{n})^2$,

$$\epsilon_{r1} = n^2 - k^2 \quad (204)$$

$$\epsilon_{r2} = 2kn \quad (205)$$

Solving Equations (204) and (205),

$$n = \frac{1}{\sqrt{2}} \sqrt{\epsilon_{r1} + \sqrt{\epsilon_{r1}^2 + \epsilon_{r2}^2}} \quad (206)$$

$$k = \frac{1}{\sqrt{2}} \sqrt{-\epsilon_{r1} + \sqrt{\epsilon_{r1}^2 + \epsilon_{r2}^2}} \quad (207)$$

3.9 Capacitance Modeling

In the previous section, currents for determining voltage, are modeled. In order to compute object charge (to be subsequently used for computing Lorentz force) from voltage, Equation (6) requires body capacitance, whose modeling depends upon the orbit regime. Primary reason for difference in capacitance modeling arises from difference in Debye length relative to body dimension. For an object with dimension ranging from tens of centimeters to few meters, Debye length is much larger than body dimension in GEO region, whereas Debye length is much smaller than body dimension in LEO region. As a consequence to this, certain first order approximations can be made in the capacitance formulation, as will be seen shortly.

3.10 Spherical Capacitance Model

For two concentric conducting spheres [28] having radii a and b respectively,

$$\Delta V = \frac{Q}{4\pi\epsilon_0} \int_a^b \left(\frac{1}{R^2} \right) dR \quad (208)$$

$$\Delta V = \frac{Q}{4\pi\epsilon_0} \left(\frac{1}{a} - \frac{1}{b} \right) \quad (209)$$

Thus, the capacitance C is,

$$C = \frac{4\pi\epsilon_0}{\left(\frac{1}{a} - \frac{1}{b} \right)} \quad (210)$$

where ϵ_0 is vacuum permittivity. At GEO altitude, $a = R$ and $b = L$, where R is radius of the assumed spherical conducting debris and L is the Debye length.

$$C = \frac{4\pi\epsilon_0 R}{1 - \frac{R}{L}} \quad (211)$$

With $\frac{R}{L} \ll 1$ for GEO, Equation (211) can be approximated as,

$$C = 4\pi\epsilon_0 R^2 \left(\frac{1}{R} + \frac{1}{L} \right) \quad (212)$$

Chunshi [42] makes further assumption by neglecting $\frac{1}{L}$ compared to $\frac{1}{R}$, and Equation (212) becomes,

$$R = 4\pi\epsilon_0 R \quad (213)$$

Using $a = R$ and $b = (R+L)$ for LEO, Equation (211) results in,

$$C = \frac{4\pi\epsilon_0 R(R+L)}{L} \quad (214)$$

With $\frac{R}{L} \gg 1$ for LEO, Equation (214) can be approximated as,

$$C = \frac{4\pi\epsilon_0 R^2}{L} \quad (215)$$

The Debye length L can be obtained from the following equation,

$$\frac{1}{L^2} = \sum \left(\frac{n_j q_j^2}{\epsilon_0 k T_j} \right) \quad (216)$$

where n , q , T and k denote number density of plasma particles, charge of particle, characteristic temperature of particle distribution and Boltzmann constant, respectively, for particle type j .

3.11 Analytic Expressions for Orbital Perturbation Due to Lorentz Force

Numerical simulation is time expensive and does not explicitly highlight the factors effecting the perturbations in various orbital elements. This section is dedicated to developing analytic expressions for perturbations in orbital elements over one orbital period time using Gauss's variational equations. The expressions developed apply to a Keplerian orbit of small eccentricity perturbed by Lorentz force.

The classical Gauss's variational equations representing time rate of change of orbital elements, are given as [14],

$$\frac{da}{dt} = \frac{2}{n\sqrt{1-e^2}} \left[Se \sin f + T(1 + e \cos f) \right] \quad (217a)$$

$$\frac{de}{dt} = \frac{\sqrt{1-e^2}}{na} \left[S \sin f + T(\cos f + \cos E) \right] \quad (217b)$$

$$\frac{di}{dt} = \frac{r \cos(\omega + f)}{na^2 \sqrt{1-e^2}} W \quad (217c)$$

$$\frac{d\Omega}{dt} = \frac{r \sin(\omega + f)}{na^2 \sqrt{1-e^2} \sin i} W \quad (217d)$$

$$\frac{d\omega}{dt} = \frac{\sqrt{1-e^2}}{nae} \left[-S \cos f + T \left(1 + \frac{r}{p} \right) \sin f \right] - \cos i \frac{d\Omega}{dt} \quad (217e)$$

where a , e , i , Ω , ω , f represent the Keplerian orbital parameters of semi-major axis, eccentricity, inclination, right ascension of ascending node (RAAN), argument of perigee and true anomaly, respectively. n , r , p , E represent mean motion, radial distance, semilatus rectum and eccentric anomaly, respectively. S and W are the components of Lorentz acceleration in radial direction and perpendicular to orbital plane direction, respectively. T represents component of Lorentz acceleration in a direction that completes the right handed orthogonal system. Peng et al. [14] calls S , T , W frame as local-vertical-local-horizontal (LVLH) frame. Obtaining expressions for S , T , W in terms of orbital parameters a , e , i , Ω , ω , f , as given in Peng et al. [14], is the key to integrating Equations (217a)-(217e).

According to classical Electrodynamics, Lorentz acceleration of an object is given as,

$$a_L = \left(\frac{q}{m} \right) \left(-(\vec{\omega}_e \times \vec{r}) \times \vec{B} + \dot{\vec{r}} \times \vec{B} \right) \quad (218)$$

where q is charge of the object, m is mass of the object, $\vec{\omega}_e$ is the angular velocity vector of Earth, \vec{r} is the geocentric position vector of the object, \vec{B} is Earth's magnetic field vector and $\dot{\vec{r}}$ is the inertial velocity vector of the object.

Use of the relation $\vec{B} = \frac{B_0}{r^3} [3(\hat{N} \cdot \hat{r})\hat{r} - \hat{N}]$ and Earth-centered inertial (ECI) vectors $\vec{\omega}_e = [0 \ 0 \ \omega_e]^T$, $\vec{r} = [x \ y \ z]^T$, $\hat{N} = [\hat{N}_x \ \hat{N}_y \ \hat{N}_z]^T$, $\dot{\vec{r}} = [\dot{x} \ \dot{y} \ \dot{z}]^T$, $\hat{r} = [\frac{x}{r} \ \frac{y}{r} \ \frac{z}{r}]^T$ in Eq. (218), where B_0 is magnetic dipole moment of Earth, r is the geocentric distance of the object, \hat{r} represents unit vector in the radial direction and \hat{N} is the unit vector in the direction of dipole, results in ECI Lorentz components [14],

$$a_{Lx} = \left(\frac{q}{m} \right) \left(\frac{B_0}{r^5} \right) \left([3x(z\dot{y} - y\dot{z} - xz\omega_e)]\hat{N}_x(t) + [3yz\dot{y} - (3y^2 - r^2)\dot{z} - 3xyz\omega_e]\hat{N}_y(t) + [(3z^2 - r^2)\dot{y} - 3yz\dot{z} - \omega_e x(3z^2 - r^2)]\hat{N}_z \right) \quad (219)$$

$$a_{Ly} = \left(\frac{q}{m} \right) \left(\frac{B_0}{r^5} \right) \left([(3x^2 - r^2)\dot{z} - 3xz\dot{x} - 3xyz\omega_e]\hat{N}_x(t) + [3y(x\dot{z} - z\dot{x} - yz\omega_e)]\hat{N}_y(t) + [3xz\dot{z} - (3z^2 - r^2)\dot{x} - \omega_e y(3z^2 - r^2)]\hat{N}_z \right) \quad (220)$$

$$a_{Lz} = \left(\frac{q}{m} \right) \left(\frac{B_0}{r^5} \right) \left([3xy\dot{x} - (3x^2 - r^2)\dot{y} + \omega_e(3xy^2 + 3x^3 - xr^2)]\hat{N}_x(t) + [(3y^2 - r^2)\dot{x} - 3xy\dot{y} + \omega_e(3y^3 + 3x^2y - yr^2)]\hat{N}_y(t) + [3z(y\dot{x} - x\dot{y} + \omega_e(x^2 + y^2))]\hat{N}_z \right) \quad (221)$$

Peng et al. [14] uses two coordinate transformations: the first transformation is performed from ECI coordinate system to an intermediate frame known as instantaneous nodal inertial coordinate frame, and the second transformation is performed from this intermediate frame to local-vertical-local horizontal (LVLH) frame. The instantaneous nodal inertial coordinate system ($OX'Y'Z'$) is defined as follows: X' lies along instantaneous intersection of equatorial and orbital planes, Z' is perpendicular to equatorial plane and Y' completes the right-handed system. $OX'Y'Z'$ is obtained by rotating the ECI frame by Ω about Z-axis. One can transform $OX'Y'Z'$ frame to LVLH frame by performing following rotations in the order: angle i about X' axis, angle $\theta = (\omega + f)$ about newly formed Z'_{new} axis.

Following the two transformations, Lorentz acceleration components a_{Lx} , a_{Ly} , a_{Lz} in ECI frame can be expressed in terms of Lorentz acceleration components S, T, W in LVLH frame as [14],

$$S = \left(\frac{q}{m}\right)B_0 \left(-\frac{\omega_e}{r^2}(\sin \theta \cos \theta \sin i) \right) \hat{N}_x(t) + \left(\frac{q}{m}\right)B_0 \left(\frac{na}{r^3\sqrt{1-e^2}}[\sin i(1+e \cos f)] - \frac{\omega_e}{r^2}(\sin^2 \theta \sin i \cos i) \right) \hat{N}_y(t) + \left(\frac{q}{m}\right)B_0 \left(-\frac{na}{r^3\sqrt{1-e^2}}[\cos i(1+e \cos f)] + \frac{\omega_e}{r^2}(1 - \sin^2 \theta \sin^2 i) \right) \hat{N}_z \quad (222a)$$

$$T = \left(\frac{q}{m}\right)B_0 \left(\frac{\omega_e}{r^2}(2 \cos^2 \theta \sin i) \right) \hat{N}_x(t) + \left(\frac{q}{m}\right)B_0 \left(\frac{na}{r^3\sqrt{1-e^2}}(-e \sin i \sin f) + \frac{\omega_e}{r^2}(\sin 2\theta \sin i \cos i) \right) \hat{N}_y(t) + \left(\frac{q}{m}\right)B_0 \left(\frac{na}{r^3\sqrt{1-e^2}}(e \cos i \sin f) + \frac{\omega_e}{r^2}(\sin 2\theta \sin^2 i) \right) \hat{N}_z \quad (222b)$$

$$W = \left(\frac{q}{m}\right)B_0 \left(\frac{na}{r^3\sqrt{1-e^2}}(-3e \cos \theta \cos f - 2 \cos \theta + e \cos \omega) + \frac{\omega_e}{r^2}(2 \cos \theta \cos i) \right) \hat{N}_x(t) + \left(\frac{q}{m}\right)B_0 \left(\frac{na}{r^3\sqrt{1-e^2}}\cos i(-3e \sin \theta \cos f - 2 \sin \theta + e \sin \omega) + \frac{\omega_e}{r^2}(2 \sin \theta \cos^2 i) \right) \hat{N}_y(t) + \left(\frac{q}{m}\right)B_0 \left(\frac{na}{r^3\sqrt{1-e^2}} \left(-\frac{\sin i}{2}[e \sin \omega + 4 \sin \theta + 3e \sin(\theta + f)] \right) + \frac{\omega_e}{r^2}(\sin 2i \sin \theta) \right) \hat{N}_z \quad (222c)$$

where $\theta = (\omega + f)$ is the argument of latitude.

The dipole direction components \hat{N}_x , \hat{N}_y , \hat{N}_z are given as,

$$\hat{N} = \begin{bmatrix} \hat{N}_x \\ \hat{N}_y \\ \hat{N}_z \end{bmatrix} = \begin{bmatrix} \sin \theta_m \cos \alpha_m \\ \sin \theta_m \sin \alpha_m \\ \cos \theta_m \end{bmatrix} \quad (223)$$

where θ_m represents angle between dipole north pole and geographic north pole. θ_m is sometimes referred to as coelevation of the dipole. α_m is given as,

$$\alpha_m = \alpha_{G0} + \omega_e t + \phi_m - \Omega \quad (224)$$

where α_{G0} represents right ascension of Greenwich at reference time (time of start of orbit propagation in simulation) and ϕ_m represents the east longitude of dipole. B_0 , θ_m and ϕ_m can be obtained using following relations from Wertz [16],

$$B_0 = R_E^3 \sqrt{(g_1^0)^2 + (g_1^1)^2 + (h_1^1)^2} \quad (225)$$

$$\cos \theta_m = \frac{g_1^0}{\sqrt{(g_1^0)^2 + (g_1^1)^2 + (h_1^1)^2}} \quad (226)$$

$$\tan \phi_m = \frac{h_1^1}{g_1^1} \quad (227)$$

where g_1^0 , g_1^1 , h_1^1 represent IGRF coefficients and R_E is mean radius of Earth.

Equations (222) - (227) can now be used in Equation (217), which can then be integrated to obtain one-period orbital perturbations. Peng et al. [14] derived expressions for one-period orbital perturbations, but they assumed that the inertial direction of Earth's magnetic dipole, $\hat{N}_x(t)$ and $\hat{N}_y(t)$, remain constant during one-orbital period. This assumption is sufficiently accurate for a low Earth orbit whose period is much small compared to Earth's rotation period. The formulas derived in this report for one-orbital period perturbations work well for all altitudes. In this research, following approximations are made while deriving the perturbation expressions: (1) eccentricity is small (near-zero), which allows for approximation of time as $t \approx \frac{f}{n}$ (2) charge-to-mass ratio of the body is constant (3) the factor $(1 + e \cos f)^{-1}$, which appears in the derivation is approximated by second-order Taylor series (4) the orbital elements [a, e, i, ω , Ω] are assumed to remain constant over the integration period.

In obtaining the one-orbital period perturbations, true anomaly is considered as the free variable,

$$\Delta x = \int_0^{2\pi} \left(\frac{dx}{dt} \frac{dt}{df} \right) df \quad (228)$$

where $x = [a, e, i, \omega, \Omega]$.

Three classes of perturbation formulas are developed,

1. General formulas: applicable for all orbit regions (except the precise GEO altitude with $\omega_e = n$, because of the factor $(\frac{\omega_e}{n} - 1)$ in denominator).
2. LEO formulas: applicable only for LEO orbits, and are derived from general formulas using the approximations $\omega_e \ll n$ and $e^2 \ll 1$.
3. GEO formulas: applicable for GEO orbit and orbits around GEO altitude, and are derived from general formulas taking the limit $\chi \rightarrow 1$, where $\chi = \frac{\omega_e}{n}$.

Following relations are useful in the derivation,

$$p = a(1 - e^2) \quad (229a)$$

$$n = \sqrt{\frac{\mu}{a^3}} \quad (229b)$$

$$\cos E = \frac{e + \cos f}{1 + e \cos f} \quad (229c)$$

$$r = \frac{a(1 - e^2)}{1 + e \cos f} \quad (229d)$$

$$\frac{dt}{df} = \frac{1}{n} \left(\frac{r}{a} \right)^2 \frac{1}{\sqrt{1 - e^2}} \quad (229e)$$

3.12 General and LEO Perturbation Expressions for One Orbital Period

The expressions for general perturbation formulas and LEO perturbation formulas have identical form, but different coefficients need to be inserted. The coefficients for general perturbation formulas can be obtained from Appendix A, and the coefficients for LEO perturbation formulas can be obtained from Appendix B.

$$\begin{aligned} \Delta a = & C_{80} \left[\sin(2\omega - \alpha_{G0} - \frac{2\pi\omega_e}{n} + \Omega - \phi_m) - \sin(2\omega - \alpha_{G0} + \Omega - \phi_m) \right] + C_{81} \left[\sin(2\omega + \alpha_{G0} \right. \\ & + \frac{2\pi\omega_e}{n} - \Omega + \phi_m) - \sin(2\omega + \alpha_{G0} - \Omega + \phi_m) \left. \right] + C_{82} \left[\sin(\alpha_{G0} + \frac{2\pi\omega_e}{n} - \Omega + \phi_m) \right. \\ & \left. - \sin(\alpha_{G0} - \Omega + \phi_m) \right] \quad (230) \end{aligned}$$

In comparison with the formulation of Peng et al [14] that can be found Appendix C, the non-constant dipole leads to further terms, in the power of the eccentricity. The simple *sini* dependence is extended with the varying dipole direction.

$$\begin{aligned} \Delta e = & D_{110} \left[\sin(2\omega + \alpha_{G0} + \frac{2\pi\omega_e}{n} - \Omega + \phi_m) - \sin(2\omega + \alpha_{G0} - \Omega + \phi_m) \right] + D_{111} \left[\sin(2\omega - \alpha_{G0} \right. \\ & - \frac{2\pi\omega_e}{n} + \Omega - \phi_m) - \sin(2\omega - \alpha_{G0} + \Omega - \phi_m) \left. \right] + D_{112} \left[\sin(\alpha_{G0} + \frac{2\pi\omega_e}{n} - \Omega + \phi_m) \right. \\ & \left. - \sin(\alpha_{G0} - \Omega + \phi_m) \right] + \frac{D_{1054}\pi}{na^2\sqrt{1 - e^2}} \sin 2\omega \quad (231) \end{aligned}$$

Comparable as in the case of the semi-major axis, relaxation of the eccentricity and dipole stability leads to higher order terms in the eccentricity and the inclination dependence is contrasted with the dipole orientation terms.

$$\Delta i = J_1 \left[\sin(2\omega + \alpha_{G0} + \frac{2\pi\omega_e}{n} - \Omega + \phi_m) - \sin(2\omega + \alpha_{G0} - \Omega + \phi_m) \right] + J_2 \left[\sin(2\omega - \alpha_{G0} \right.$$

$$\begin{aligned}
& -\frac{2\pi\omega_e}{n} + \Omega - \phi_m) - \sin(2\omega - \alpha_{G0} + \Omega - \phi_m) \Big] + J_3 \left[\sin(\alpha_{G0} + \frac{2\pi\omega_e}{n} - \Omega + \phi_m) \right. \\
& \left. - \sin(\alpha_{G0} - \Omega + \phi_m) \right] + H_4 \left[\cos(\omega + \alpha_{G0} + \frac{2\pi\omega_e}{n} - \Omega + \phi_m) - \cos(\omega + \alpha_{G0} - \Omega + \phi_m) \right] + \\
& H_5 \left[\cos(\omega - \alpha_{G0} - \frac{2\pi\omega_e}{n} + \Omega - \phi_m) - \cos(\omega - \alpha_{G0} + \Omega - \phi_m) \right] + \\
& E_{202} \left[\sin(\omega + \alpha_{G0} + \frac{2\pi\omega_e}{n} - \Omega + \phi_m) - \sin(\omega + \alpha_{G0} - \Omega + \phi_m) \right] + \\
& E_{203} \left[\sin(\omega - \alpha_{G0} - \frac{2\pi\omega_e}{n} + \Omega - \phi_m) - \sin(\omega - \alpha_{G0} + \Omega - \phi_m) \right] + \frac{\pi \sin 2\omega}{na^2\sqrt{1-e^2}} I_{12} \quad (232)
\end{aligned}$$

In comparison to Peng, higher order terms in the eccentricity occur. The J terms are not referring to gravitational constants but can be found in the appendix as well.

$$\begin{aligned}
\Delta\Omega = & N_1 \left[\cos(2\omega + \alpha_{G0} + \frac{2\pi\omega_e}{n} - \Omega + \phi_m) - \cos(2\omega + \alpha_{G0} - \Omega + \phi_m) \right] + N_2 \left[\cos(2\omega - \alpha_{G0} \right. \\
& \left. - \frac{2\pi\omega_e}{n} + \Omega - \phi_m) - \cos(2\omega - \alpha_{G0} + \Omega - \phi_m) \right] + N_3 \left[\cos(\alpha_{G0} + \frac{2\pi\omega_e}{n} - \Omega + \phi_m) - \right. \\
& \left. \cos(\alpha_{G0} - \Omega + \phi_m) \right] + L_{177} \left[\cos(\omega + \alpha_{G0} + \frac{2\pi\omega_e}{n} - \Omega + \phi_m) - \cos(\omega + \alpha_{G0} - \Omega + \phi_m) \right] \\
& + L_{178} \left[\cos(\omega - \alpha_{G0} - \frac{2\pi\omega_e}{n} + \Omega - \phi_m) - \cos(\omega - \alpha_{G0} + \Omega - \phi_m) \right] \\
& + J_{180} \left[\sin(\omega + \alpha_{G0} + \frac{2\pi\omega_e}{n} - \Omega + \phi_m) - \sin(\omega + \alpha_{G0} - \Omega + \phi_m) \right] \\
& + J_{181} \left[\sin(\omega - \alpha_{G0} - \frac{2\pi\omega_e}{n} + \Omega - \phi_m) - \sin(\omega - \alpha_{G0} + \Omega - \phi_m) \right] + \\
& \frac{K_6\pi}{na^2\sqrt{1-e^2}} \left[K_{11} + K_{13} \sin \omega \right] + \frac{2\pi K_9}{na^2\sqrt{1-e^2}} \left[\frac{K_{12}}{2} + K_2 \sin \omega + K_{14} \sin^2 \omega \right] \\
& + \frac{\pi K_{10}}{na^2\sqrt{1-e^2}} \left[K_{15} - K_{11} \cos 2\omega + K_{13} \sin \omega \right] \quad (233)
\end{aligned}$$

Again, higher order terms do occur. The term labelled N are placeholders and can be found in the appendix. They are unconnected to the dipole direction.

$$\begin{aligned}
\Delta\omega = & Q_{142} \left[\cos(2\omega + \alpha_{G0} + \frac{2\pi\omega_e}{n} - \Omega + \phi_m) - \cos(2\omega + \alpha_{G0} - \Omega + \phi_m) \right] + Q_{143} \left[\cos(2\omega - \right. \\
& \left. \alpha_{G0} - \frac{2\pi\omega_e}{n} + \Omega - \phi_m) - \cos(2\omega - \alpha_{G0} + \Omega - \phi_m) \right] + Q_{144} \left[\cos(\alpha_{G0} + \frac{2\pi\omega_e}{n} - \Omega + \phi_m) \right.
\end{aligned}$$

$$\begin{aligned}
& -\cos(\alpha_{G0} - \Omega + \phi_m) \Big] + Q_{145} \Big[\cos(\omega + \alpha_{G0} + \frac{2\pi\omega_e}{n} - \Omega + \phi_m) - \cos(\omega + \alpha_{G0} - \Omega + \phi_m) \Big] \\
& + Q_{146} \Big[\cos(\omega - \alpha_{G0} - \frac{2\pi\omega_e}{n} + \Omega - \phi_m) - \cos(\omega - \alpha_{G0} + \Omega - \phi_m) \Big] \\
& + Q_{147} \Big[\sin(\omega + \alpha_{G0} + \frac{2\pi\omega_e}{n} - \Omega + \phi_m) - \sin(\omega + \alpha_{G0} - \Omega + \phi_m) \Big] \\
& + Q_{148} \Big[\sin(\omega - \alpha_{G0} - \frac{2\pi\omega_e}{n} + \Omega - \phi_m) - \sin(\omega - \alpha_{G0} + \Omega - \phi_m) \Big] \\
& + \frac{Q_{149}\pi}{na^2\sqrt{1-e^2}} \Big[K_{11} + K_{13} \sin \omega \Big] + \frac{2\pi Q_{150}}{na^2\sqrt{1-e^2}} \Big[\frac{K_{12}}{2} + K_2 \sin \omega + K_{14} \sin^2 \omega \Big] + \frac{\pi Q_{151}}{na^2\sqrt{1-e^2}} \\
& \Big[K_{15} - K_{11} \cos 2\omega + K_{13} \sin \omega \Big] + \frac{\pi}{na^2\sqrt{1-e^2}} \Big[Q_{43} + Q_{131}Q_{133} + \frac{Q_{131}Q_{134}e}{2} \\
& + Q_{132}Q_{134} \cos 2\omega \Big] \quad (234)
\end{aligned}$$

3.13 GEO Perturbation Expressions for One Orbital Period

In the following, the orbital averaged expressions of the Lorentz force induced perturbations of each of the orbital elements in the geostationary region are listed.

$$\begin{aligned}
\Delta a = B_0\pi \left(\frac{q}{m} \right) \frac{\omega_e a \sin i \sin \theta_m \cos^2 \frac{i}{2} e}{\mu(1-e^2)} \cos(2\omega - \alpha_{G0} + \Omega - \phi_m) + B_0\pi \left(\frac{q}{m} \right) \frac{\sin i \sin \theta_m e}{na^2(1-e^2)} \\
(2 - \cos i) \cos(\alpha_{G0} - \Omega + \phi_m) - \frac{1}{2} B_0\pi \left(\frac{q}{m} \right) \frac{\sin i \sin \theta_m e^3}{na^2(1-e^2)^{\frac{5}{2}}} \cos(\alpha_{G0} - \Omega + \phi_m) \quad (235)
\end{aligned}$$

Compared to Peng et al [14], as in the previous case, higher order terms are picked up in eccentricity. The dipole dependence of the Lorentz force in combination with the time dependence of the dipole leads to a coupled term of the *sini* and the pole change.

$$\begin{aligned}
\Delta e = B_0\pi \left(\frac{q}{m} \right) \frac{\omega_e \sin i \sin \theta_m \sin^2 \frac{i}{2} e^2}{4\mu} \cos(2\omega + \alpha_{G0} - \Omega + \phi_m) - \frac{B_0\pi}{\mu} \left(\frac{q}{m} \right) \sin i \sin \theta_m \cos^2 \frac{i}{2} \omega_e \\
\left(\frac{e^2}{4} - \frac{3}{2} \right) \cos(2\omega - \alpha_{G0} + \Omega - \phi_m) + \frac{B_0\pi}{a^3 n (1-e^2)^{\frac{3}{2}}} \left(\frac{q}{m} \right) \sin i \sin \theta_m \left(1 - e^2 - \frac{e^4}{4} \right) \\
\cos(\alpha_{G0} - \Omega + \phi_m) - \frac{B_0\pi}{a^3 n} \left(\frac{q}{m} \right) \sin i \sin \theta_m \left(\frac{e^2}{4} - 2 + \frac{\cos i}{2} \right) \cos(\alpha_{G0} - \Omega + \phi_m) \\
- \frac{B_0\omega_e}{\mu} \frac{q}{m} \cos \theta_m \sin^2 i \left(-e^3 + \frac{e}{2} \right) \pi \sin 2\omega \quad (236)
\end{aligned}$$

In the eccentricity, the overall structure of the terms is comparable to Peng, however, the time varying dipole terms occur.

$$\begin{aligned}
\Delta\Omega = & -\frac{\pi B_0 e^3 q \sin \theta_m \sin^2 \frac{i}{2}}{4a^3 mn \sin i (1-e^2)^{\frac{3}{2}}} \sin(2\omega + \alpha_{G0} - \Omega + \phi_m) - \frac{3\pi B_0 e q \sin \theta_m \cos^2 \frac{i}{2} (1 + \frac{e^2}{2})}{2a^3 mn \sin i (1-e^2)^{\frac{3}{2}}} \\
& \sin(2\omega - \alpha_{G0} + \Omega - \phi_m) - \frac{\pi B_0 e q \sin \theta_m \cos i \cos^2 \frac{i}{2}}{a^3 mn \sin i} \sin(2\omega - \alpha_{G0} + \Omega - \phi_m) \\
& - \frac{3\pi B_0 e q \sin \theta_m \cos i (1 + \frac{e^2}{2})}{2a^3 mn \sin i (1-e^2)^{\frac{3}{2}}} \sin(\alpha_{G0} - \Omega + \phi_m) - \frac{\pi B_0 e q \sin \theta_m \cos^2 i}{a^3 mn \sin i} \sin(\alpha_{G0} - \Omega + \phi_m) \\
& + \frac{\pi B_0 e q \cos \omega \sin \theta_m}{a^3 mn \sin i (1-e^2)^{\frac{3}{2}}} \sin(\omega - \alpha_{G0} + \Omega - \phi_m) + \frac{\pi B_0 e q \cos i \sin \omega \sin \theta_m}{a^3 mn \sin i (1-e^2)^{\frac{3}{2}}} \cos(\omega - \alpha_{G0} + \Omega - \phi_m) \\
& - \frac{(\frac{e^2}{2} + 1)\pi B_0 q \cos \theta_m}{na^3 m (1-e^2)^{\frac{3}{2}}} \left[2 + \frac{3e^2}{4} - 2 \cos i (1-e^2)^{\frac{3}{2}} + \frac{e^2 \sin^2 \omega}{2} \right] + \frac{\pi e^2 B_0 q \cos \theta_m}{2na^3 m (1-e^2)^{\frac{3}{2}}} \left[\frac{5}{2} + 3 \sin^2 \omega \right] \\
& - \frac{\pi e^2 B_0 q \cos \theta_m}{4na^3 m (1-e^2)^{\frac{3}{2}}} \left[\frac{3e^2}{4} - 2 \cos 2\omega - \frac{3e^2 \cos 2\omega}{4} + 2 \cos i (1-e^2)^{\frac{3}{2}} \cos 2\omega + \frac{e^2 \sin^2 \omega}{2} \right] \quad (237)
\end{aligned}$$

$$\begin{aligned}
\Delta\omega = & -\frac{B_0 q e \pi \sin \theta_m \sin^2 \frac{i}{2}}{4a^3 mn} \left(-\frac{e^2 \cos i}{\sin i (1-e^2)^{\frac{3}{2}}} + \sin i \right) \sin(2\omega + \alpha_{G0} - \Omega + \phi_m) + \frac{2\pi B_0 q \sin \theta_m \cos^2 \frac{i}{2}}{a^3 mn} \\
& \left[\frac{3e \cos i (1 + \frac{e^2}{2})}{4 \sin i (1-e^2)^{\frac{3}{2}}} + \frac{e \cos^2 i}{2 \sin i} - \frac{(3 + \frac{e^2}{2}) \sin i}{4e} \right] \sin(2\omega - \alpha_{G0} + \Omega - \phi_m) - \frac{2\pi B_0 q \sin \theta_m}{a^3 mn} \\
& \sin(\alpha_{G0} - \Omega + \phi_m) \left[-\frac{3e \cos^2 i (1 + \frac{e^2}{2})}{4 \sin i (1-e^2)^{\frac{3}{2}}} - \frac{e \cos^3 i}{2 \sin i} + \frac{\sin i (\frac{e^3}{8} + e + \frac{1}{e})}{2(1-e^2)^{\frac{3}{2}}} + \frac{\sin i (\frac{e^2}{4} + 2 - \frac{\cos i}{2})}{2e} \right] \\
& - \frac{\pi B_0 e q \cos \omega \sin \theta_m \cos i}{a^3 mn \sin i (1-e^2)^{\frac{3}{2}}} \sin(\omega - \alpha_{G0} + \Omega - \phi_m) - \frac{\pi B_0 e q \cos^2 i \sin \omega \sin \theta_m}{a^3 mn \sin i (1-e^2)^{\frac{3}{2}}} \cos(\omega - \alpha_{G0} + \Omega - \phi_m) \\
& + \frac{(\frac{e^2}{2} + 1)\pi B_0 q \cos \theta_m \cos i}{na^3 m (1-e^2)^{\frac{3}{2}}} \left[2 + \frac{3e^2}{4} - 2 \cos i (1-e^2)^{\frac{3}{2}} + \frac{e^2 \sin^2 \omega}{2} \right] - \frac{\pi e^2 B_0 q \cos \theta_m \cos i}{2na^3 m (1-e^2)^{\frac{3}{2}}} \\
& \left[\frac{5}{2} + 3 \sin^2 \omega \right] + \frac{\pi e^2 B_0 q \cos \theta_m \cos i}{4na^3 m (1-e^2)^{\frac{3}{2}}} \left[\frac{3e^2}{4} - 2 \cos 2\omega - \frac{3e^2 \cos 2\omega}{4} + 2 \cos i (1-e^2)^{\frac{3}{2}} \cos 2\omega \right. \\
& \left. + \frac{e^2 \sin^2 \omega}{2} \right] + \frac{\pi B_0 q \cos \theta_m}{na^3 m (1-e^2)^{\frac{3}{2}}} \left[4 \cos i - \frac{\cos 2\omega \sin^2 i (1-e^2)^{\frac{3}{2}}}{2} \right] \quad (238)
\end{aligned}$$

In general the terms for the geosynchronous region are simpler and easier to control compared to the low earth orbital region or the more general expressions. This is due to the fact that the approximation limit of $\frac{\omega_e}{n}$ could be utilized.

4.0 RESULTS AND DISCUSSION

Several orbits corresponding to LEO and GEO regions are simulated. For all the simulation cases, an aluminum sphere of 1 m^2 surface area is considered. Simulation time is four days. Epoch

of initialization is 12:00:00 UTC, March 21, 2000. Earth's gravity, Sun and Moon gravitational perturbation, direct solar radiation pressure (SRP), atmospheric drag (only for LEO) and Lorentz force perturbation are included in the modeling. Gravitational potential has been modeled up to degree and order 12. Atmospheric drag coefficient is taken as two for spherical body. SRP diffuse reflection coefficient is taken as .035. Dipole model has been chosen for Earth's magnetic field. Earth's shadow is modeled as a cylinder. For LEO simulations, plasma electrons are assumed to be collected over entire surface area, whereas photons and plasma ions are assumed to be collected over frontal surface area. For GEO simulations, plasma electrons and ions are assumed to be collected over entire surface area, whereas photons are assumed to be collected over frontal surface area. This difference between GEO and LEO, as stated earlier, is because LEO ions are at rest relative to body and hence ram into frontal surface area. Two area-to-mass ratio objects are investigated, one corresponds to general satellites with low area-to-mass ratio (LAMR) of $.02 \frac{m^2}{kg}$ and the other corresponds to high area-to-mass ratio (HAMR) of $23.6 \frac{m^2}{kg}$.

4.1 Low Earth Orbit Simulation

Three different groups of LEO are simulated. The first LEO group is characterized by low initial inclination; the second LEO group is characterized by high initial inclination; and the third LEO group comprises of sun-synchronous orbits. Table 3 describes the LEO cases that are simulated.

Table 3. The LEO Cases

$a = 6778 \text{ Km}, \omega = 30^0, \Omega = 60^0, v = 100^0, e = .001$		
LEO group 1 ($i = .1^0$)	LEO group 2 ($i = 89^0$)	LEO group 3 ($i = 97.0292^0$)
AMR = .02	AMR = .02	AMR = .02
AMR = 23.6	AMR = 23.6	AMR = 23.6

Two plasma conditions are simulated, one resulting in low body charge and the other leading to high body charge. For low-charge plasma condition, International Reference Ionosphere (IRI) is used to obtain electron temperature, ion temperature, electron density, percentage ion composition for a given date, latitude, longitude and height profile. Composition of O^+ , H^+ , He^+ , O_2^+ , NO^+ and N^+ ions can be obtained. High-charge plasma condition corresponds to body entering auroral ovals in the north and south geomagnetic hemispheres. Location of auroral oval is determined using Holzworth's interpolation curve [43],

$$\theta = A_1 + A_2 \cos(\phi + A_3) + A_4 \cos(2\phi + 2A_5) + A_6 \cos(3\phi + 3A_7) \quad (239)$$

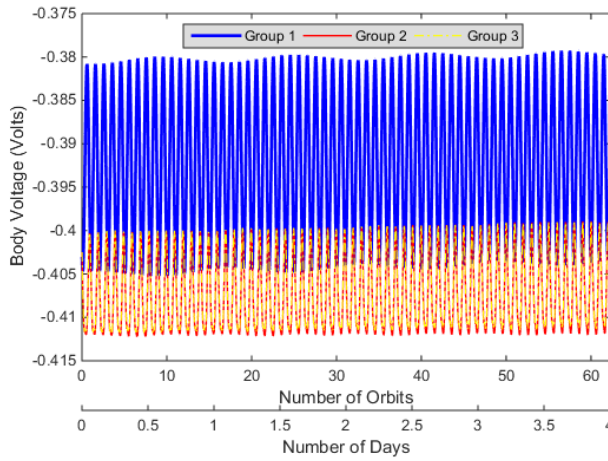
where θ is corrected geomagnetic co-latitude and ϕ represents magnetic local time in radians. A table listing values of coefficients A_1 through A_7 for poleward edge and equatorward edge of the auroral oval is given by Holzworth [43] at various geomagnetic conditions discriminated by the parameter Q (IGY quarter-hourly range index of magnetic activity) values. For the simulations in

this report, Q is two (relatively quiet geomagnetic activity). Corrected geomagnetic co-latitude and magnetic local time are obtained using a software package developed by Shepherd [44]. The high-charge plasma densities and temperatures inside auroral ovals are simulated as *Spennis Fontheim with ECSS cold background* environment [45], which is defined in Table 4.

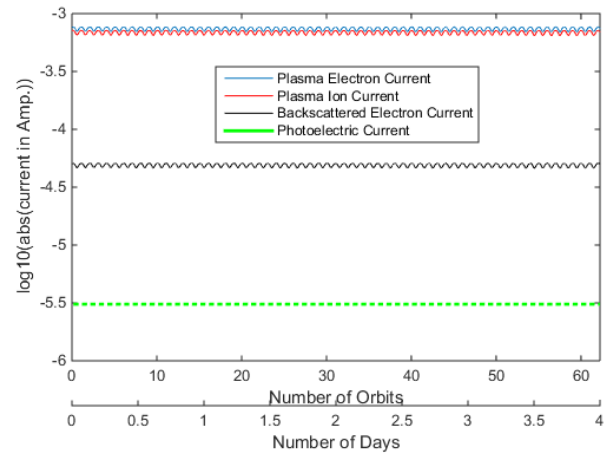
Table 4. Plasma Parameters Inside Auroral Oval

Particles	Number Density (cm^{-3})	Energy (eV)
O^+ ions	125	.2
electrons1	125	.2
electrons2	1.482	12940

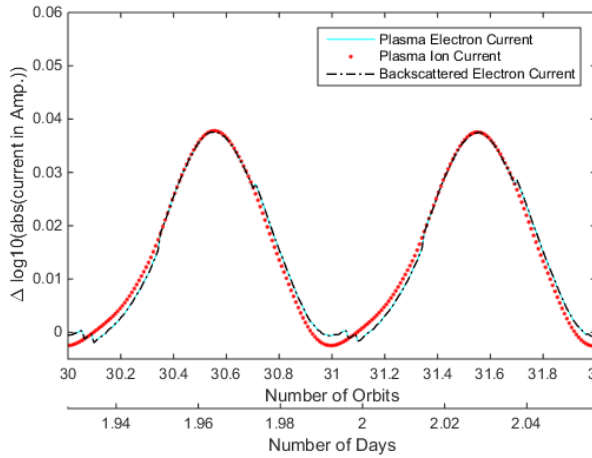
Figure 7 shows the voltage and current plots of LEO LAMR bodies Under Low-charge plasma condition. Figure 7a plots the voltage comparison of group 1, group 2, group 3 LEO objects. The body voltage plots have a short-period variation of one orbital period and a long-period variation of one day. These periodic variations in voltage result from periodicity in altitude or the LEO plasma data dependence on altitude; the altitude variations arise mainly because of the orbit eccentricity value and its variation. Figure 7b shows the logarithm of absolute value of current for 0.1^0 inclined LEO. Plasma electron current is the dominating current, and hence the equilibrium voltages are negative. In the photoelectric current plot of Figure 7b, when an object is in Earth's shadow, the photoelectric current is zero (or its logarithm value is not defined), whereas it is a constant negative value when the object is in sunlight. Since photoelectric current is several orders of magnitude smaller than other currents, the voltage changes resulting from sunlight-to-shadow and shadow-to-sunlight transitions are not significant. Figure 7c shows the difference between currents of group 2 and group 1 (for truncated duration: orbit 30 - orbit 32), Figure 7d shows difference between currents of group 3 and group 1. As can be seen, group 2 and group 3 currents are of similar order as that of currents of group 1. Difference of photoelectric currents is deliberately not included in Figure 7c and Figure 7d, as different-group orbits enter or leave Earth's shadow region at different times; the values of photoelectric currents for group 2 or group 3, are, however, same as that of group 1.



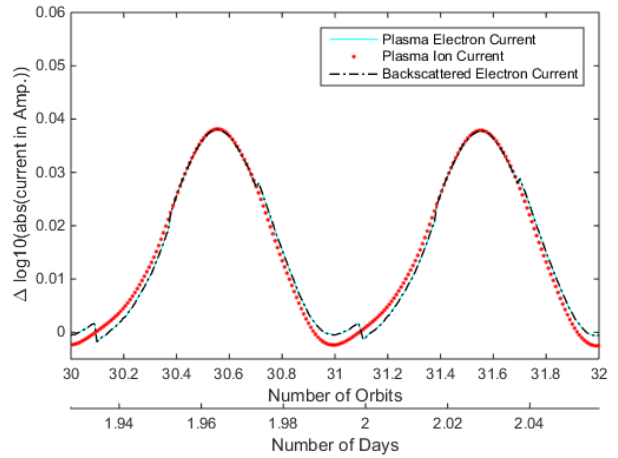
(a) Body Voltage



(b) Logarithm of Absolute Value of Current (Group 1)



(c) Difference in Logarithm of Absolute Value of Currents (Group 2 - Group 1)



(d) Difference in Logarithm of Absolute Value of Currents (Group 3 - Group 1)

Figure 7. Charging Characteristic of LEO Under Low-Charge Plasma Conditions (LAMR)

Figure 8 shows the voltage for LEO objects Under High-charge plasma conditions. As compared to low-charge plasma condition depicted in Figure 7, where the maximum negative voltage is less than unity, here the voltage can reach thousands of negative volts. The body voltages inside auroral oval reach approximately -2.6K Volts under sunlit condition and reach approximately -60K Volts (orbit number 51 and 53 in Figure 8a, e.g.), when in Earth's shadow. When outside the auroral oval, body voltages are small and of comparable order as that of low-charge plasma conditions.

Figure 9 shows the common logarithm of magnitudes of perturbing accelerations for LEO orbits. The most dominant and the least dominant perturbing accelerations correspond to higher harmonics of Earth's gravitational force and Lorentz force, respectively. The jumps in Lorentz force in higher inclined orbits are due to \vec{B} nearly aligning up with \vec{v}_{rel} .

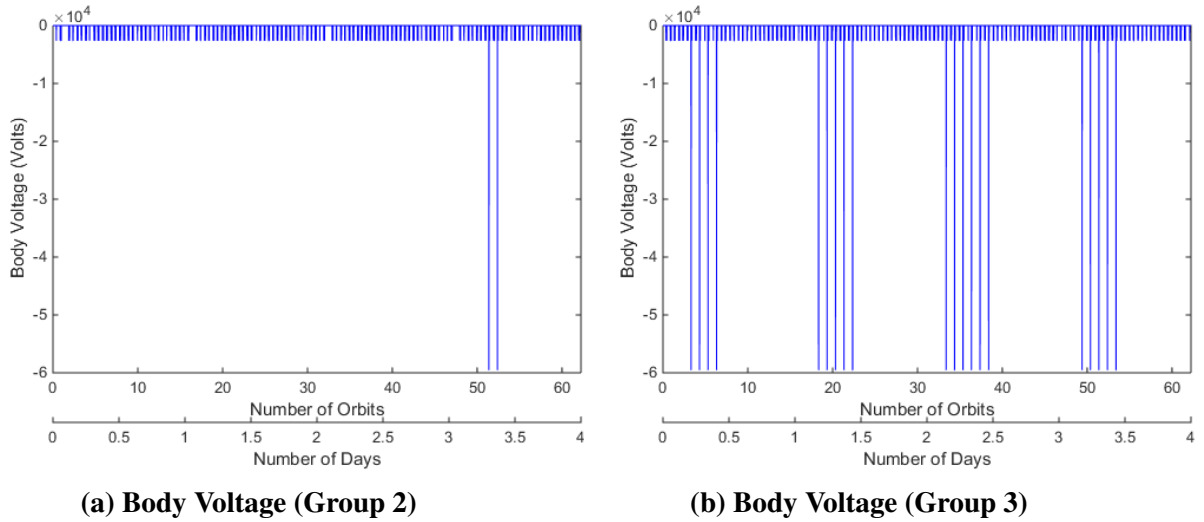


Figure 8. Voltage Characteristic of LEO Objects (LAMR, High-Charge Plasma Condition)

In order to investigate the importance of Lorentz force, difference between simulation cases including Lorentz force and simulation cases excluding Lorentz force for low-charge plasma conditions are displayed in Figures 10, 11, 12. Figure 10 shows the in-track perturbations. For the in-track perturbation, the dynamics is clearly secular for all the three groups. In addition to the long-term secular variation, there is also a short-period variation, most clearly visible in group 1 in-track plots; the periodic variation corresponds to the body voltage periodic variation as seen in Figure 7a. The positive values of in-track perturbations also suggest that the position in Lorentz force included orbit is always ahead of the position in Lorentz force excluded orbit. The in-track perturbations are of the order of 10^{-3} m for all the three groups.

Figure 11 shows the cross-track perturbations. For cross-track perturbations, the mean is approximately zero, which implies that, on an average, there is no change in orbital plane due to Lorentz force. For all the three groups, there is a short-period variation with time-scale of one orbital period and increasing amplitude. A factor contributing to the increasing short-period amplitude of cross-track perturbations is the increasing inclination of Lorentz included orbit relative to Lorentz excluded orbit over time. For higher inclined group 2 or group 3 orbits, there is also a long-period variation with time-scale of one day. Cross-track perturbations are also influenced by orbit inclination, as the perturbations are an order higher for higher inclined group 2 or group 3 orbits as compared to lowly inclined group 1 orbit, whose cross-track perturbations are of the order of 10^{-4} to 10^{-3} m.

Figure 12 shows the radial perturbations. For radial perturbations of lowly inclined group 1 orbit, the mean is approximately a negative constant value. Radial perturbations of group 1 orbit exhibit a short-period variation of one orbital time period with an increasing amplitude. Possible explanations for the increasing amplitude include the increasing amplitude of variation in the semi-major axis difference between Lorentz included and Lorentz excluded orbits. Higher inclined group 2 and group 3 orbits exhibit, on an average, a decreasing secular behavior. A factor contributing to this

secular behavior in radial perturbations is the decreasing semi-major axis of Lorentz force included orbit relative to semi-major axis of Lorentz force excluded orbit over time. A short one-orbital period variation and a long one-day period variation are also exhibited by the radial perturbations of group 2 and group 3 orbits. The radial perturbations are of the order of 10^{-5} m for group 2 and d3 and of 10^{-4} m for group 1.

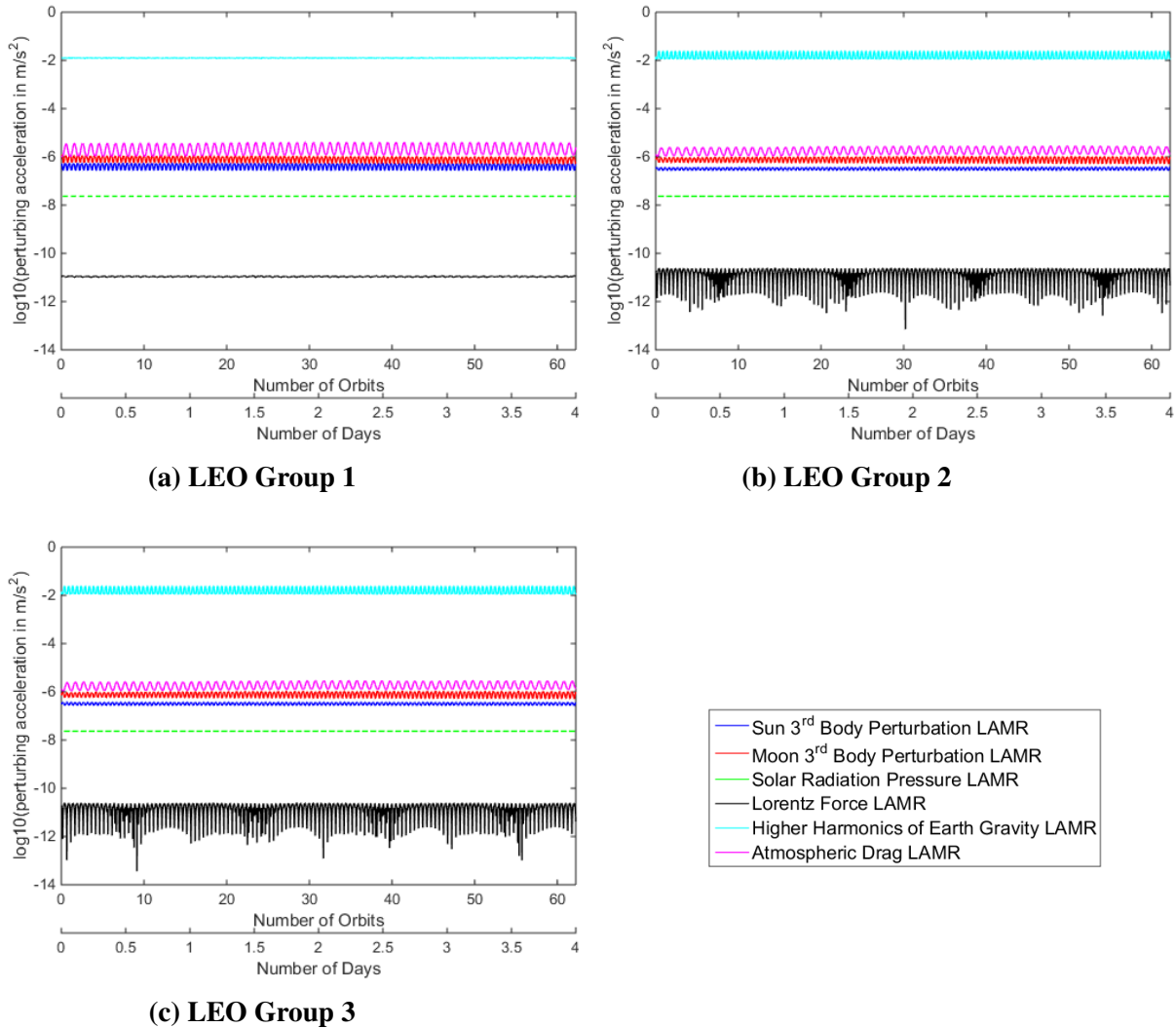
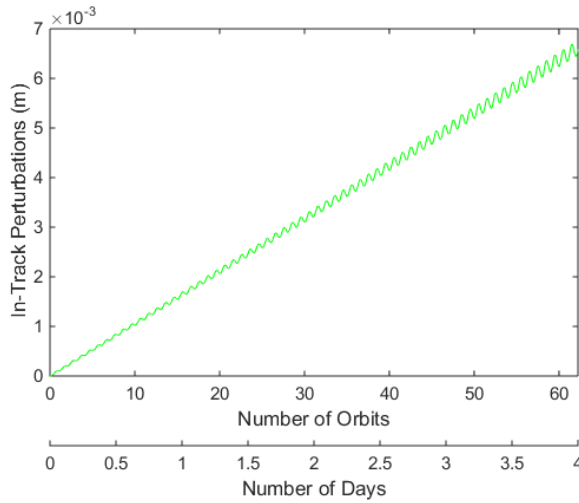
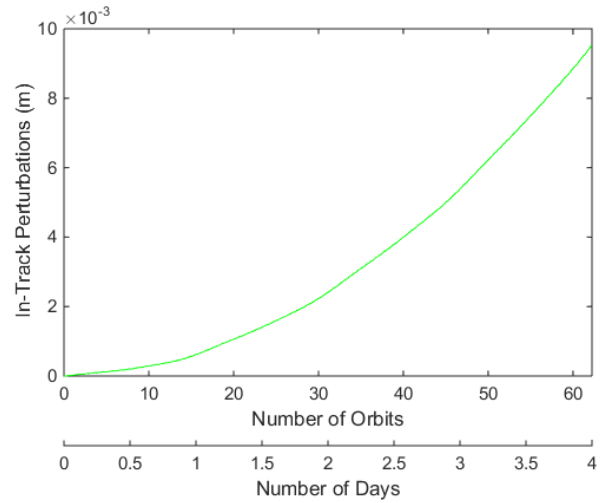


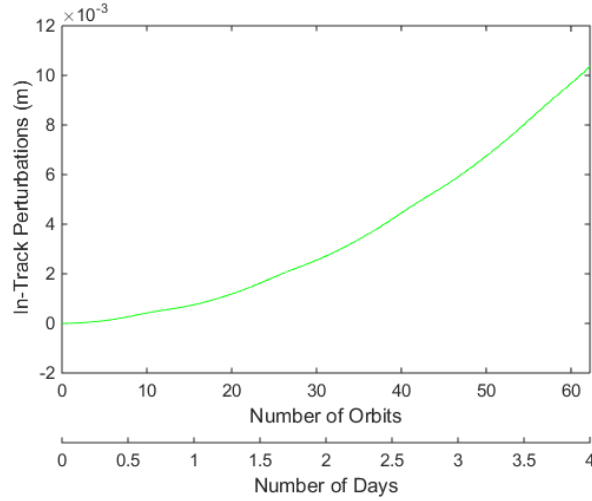
Figure 9. Common Logarithm of Perturbing Acceleration Magnitudes for LEO Orbits Under Low-Charge Plasma Conditions



(a) In-track Perturbations, Group 1

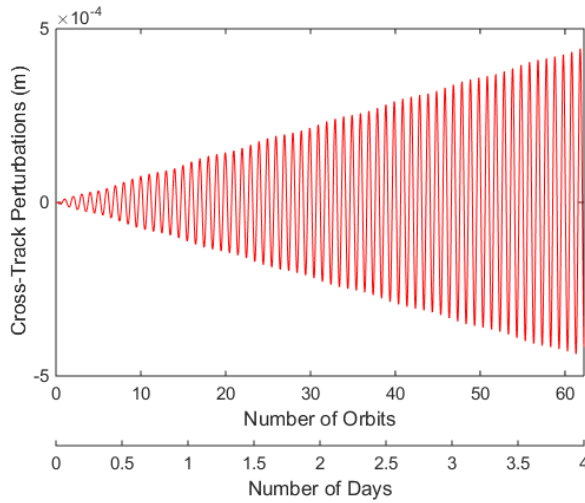


(b) In-track Perturbations, Group 2

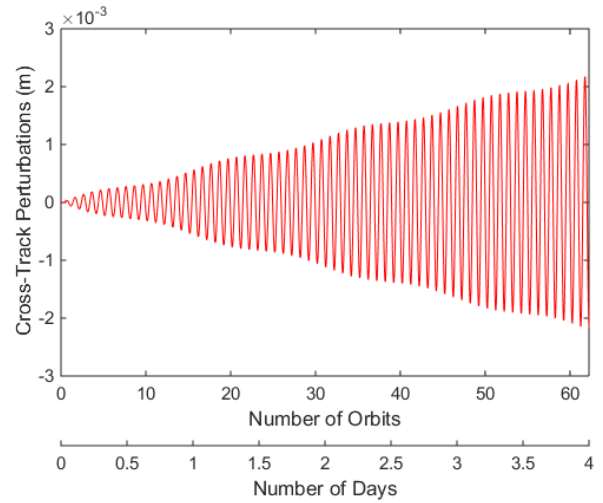


(c) In-track Perturbations, Group 3

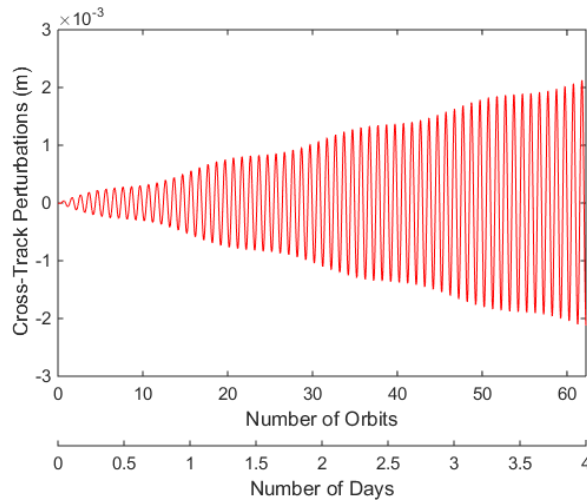
Figure 10. In-track Perturbations for Lorentz Force Perturbed Low Earth Orbit Relative to Lorentz Force Excluded Orbit Under Low-Charge Plasma Conditions (LAMR Object)



**(a) Cross-Track Perturbations,
Group 1**

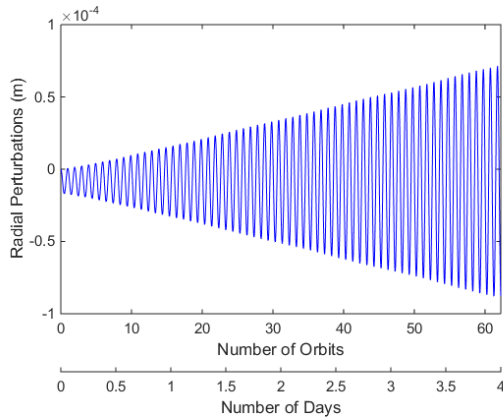


**(b) Cross-Track Perturbations,
Group 2**

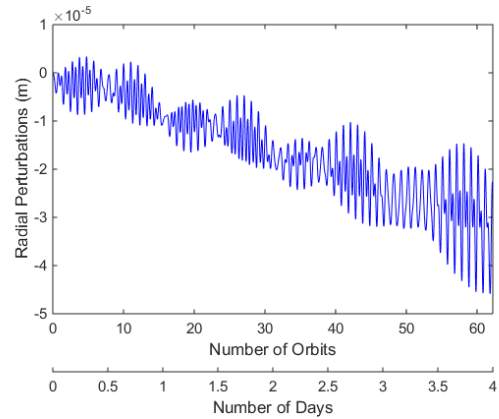


**(c) Cross-Track Perturbations,
Group 3**

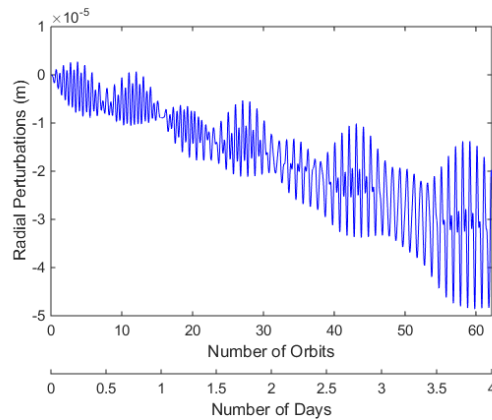
**Figure 11. Cross-track Perturbations for Lorentz Force Perturbed Low Earth Orbit
Relative to Lorentz Force Excluded Orbit Under Low-Charge Plasma Conditions
(LAMR Object)**



(a) Radial Perturbations, Group 1



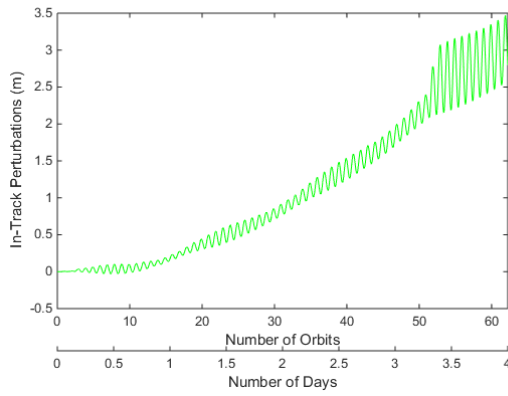
(b) Radial Perturbations, Group 2



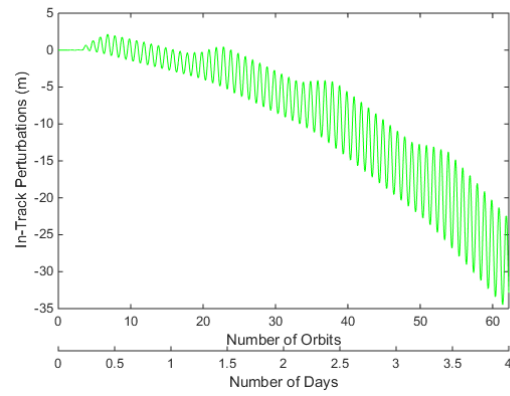
(c) Radial Perturbations, Group 3

Figure 12. Radial Perturbations for Lorentz Force Perturbed Low Earth Orbit Relative to Lorentz Force Excluded Orbit Under Low-Charge Plasma Conditions (LAMR Object)

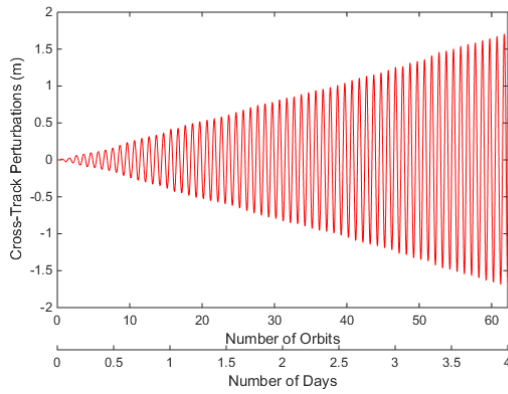
Figure 13 shows in-track, cross-track and radial perturbations between Lorentz-included and Lorentz-excluded simulation cases for LEO LAMR objects Under High-charge plasma condition. High-charge plasma conditions are created through auroral passages, which do not apply to lowly in-clined group 1 orbit. Compared to low-charge plasma conditions given by Figures 10, 11, 12, the perturbations in Figure 13 are several order magnitudes larger due to high negative voltages inside auroral oval as seen in Figure 8. The in-track and cross-track perturbations are of the order of two to 3.5 meters for group 2. Group 3 experiences a large secular trend in the in-track direction of up to 35 meters and a periodic perturbation of up to 5 meters in the cross track direction. The radial perturbations are of the order of 0.25 m for group 2 and of four meters for group 3. The secular/periodic trend is similar to that of low-charge plasma condition. The steep change in group 2 in-track and radial perturbations around orbit 51 is due to large negative body voltage as observed in Figure 8a, same holds for the step function like increase for group 3 (compare with Figure 8b).



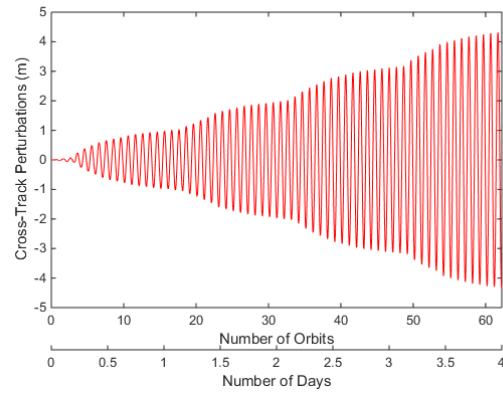
**(a) In-Track Perturbations,
Group 2**



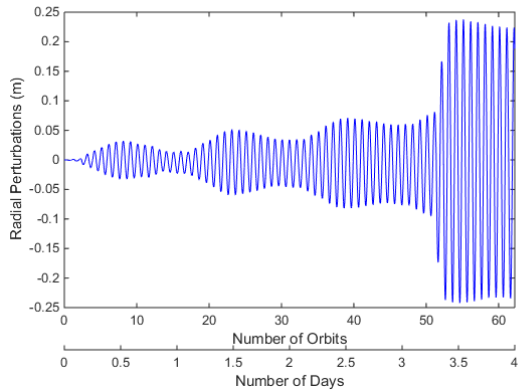
**(b) In-Track Perturbations,
Group 3**



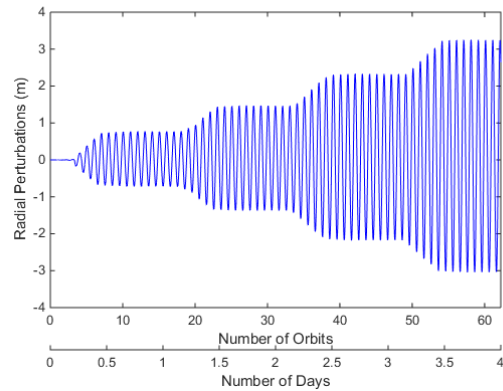
**(c) Cross-Track Perturbations,
Group 2**



**(d) Cross-Track Perturbations,
Group 3**



(e) Radial-Track Perturbations, Group 2



(f) Radial -Track Perturbations, Group 3

Figure 13. In-Track Perturbations, Cross-Track perturbations, Radial Perturbations for Lorentz Force Perturbed Low Earth Orbit Relative to Lorentz Force Excluded Orbit Under High-Charge Plasma Conditions (LAMR object)

HAMR LEO objects (initial $a = 6778$ Km) crash into Earth after about five orbital time-periods because of high atmospheric drag forces. Tables 5, 6 show a single orbit in-track, cross-track and radial perturbations for HAMR objects in LEO Under Low-charge and high-charge plasma conditions respectively.

Table 5. Perturbations of HAMR Object in LEO Under Low-Charge Plasma Conditions After One Orbital Time-Period

Orbit Group	In-track Perturbations (m)	Cross-track (m)	Perturbations	Radial Perturbations (m)
Group 1	1.39×10^{-1}	1×10^{-2}		-7×10^{-3}
Group 2	2.7×10^{-2}	-3.9×10^{-2}		-4×10^{-3}
Group 3	6×10^{-3}	-4×10^{-2}		-3×10^{-3}

Table 6. Perturbations of HAMR Object in LEO Under High-Charge Plasma Conditions After One Orbital Time-Period

Orbit Group	In-track Perturbations (m)	Cross-track (m)	Perturbations	Radial Perturbations (m)
Group 2	5.34	-1.91×10^1		-4.49×10^{-2}
Group 3	5.85×10^{-1}	-1.63×10^1		-3.04×10^{-2}

4.2 Geosynchronous Earth Orbit Simulation

Three different groups of geosynchronous orbits are considered; the first GEO group is characterized by low inclination ($.1^0$) and small eccentricity (.001) as initial parameters; the second GEO group is characterized by inclination of 15^0 and eccentricity of .015; and the third GEO group is characterized by inclination of 40^0 and eccentricity of .015. The initial argument of perigee and right ascension of ascending node values are kept same as that of LEO simulations. The initial true anomaly values are taken such that the initial longitude value is 75^0 E (GEO libration point). The GEO cases are given in Table 7.

Table 7. The GEO Cases

$a = 42164 \text{ Km}, \omega = 30^0, \Omega = 60^0$		
GEO group 1 ($i = .1^0, e = .001, v = 344.15^0$)	GEO group 2 ($i = 15^0, e = .015, v = 344.6$)	GEO group 3 ($i = 40^0, e = .015, v = 349^0$)
AMR = .02	AMR = .02	AMR = .02
AMR = 23.6	AMR = 23.6	AMR = 23.6

Similar to LEO, two different plasma conditions are simulated, one corresponding to low-charge conditions and the other corresponding to high-charge conditions. Denton [46] provides GEO plasma parameters for three classes of particles: hot electrons (30 eV to 45 KeV), hot protons (100 eV to 45 KeV) and low protons (1 eV to 100 eV). Data corresponding to one-solar-cycle (1990 - 2001) averaged low proton density, hot proton density, hot electron density, hot proton perpendicular and parallel temperatures, hot electron perpendicular and parallel temperatures (Maxwellian temperatures for distributions in the perpendicular and parallel directions of magnetic field, respectively) can be obtained from Denton [46]. The net temperature for the overall distribution is then taken as

$$T = \frac{2}{3}T_{\perp} + \frac{1}{3}T_{\parallel} \quad (240)$$

Temperature distribution for low protons is not given by Denton. An assumption of 50 eV (corresponding to mid value of the energy range) is used for the low proton temperature. Once the data is extracted from Denton for a particular turbulence level (decided by geomagnetic K_p index value), an interpolation surface is fit through the data from which plasma parameters can be obtained for any orbit local time. Low-charge plasma condition is simulated using Denton's data for $K_p = 1$. For simulating high-charge plasma condition, high-flux ATS-6 data [15], given in Table 8, have been used.

Table 8. High-Charge Plasma Environment for GEO

Particles	Number Density (m^{-3})	Energy (eV)
electrons	2.36×10^5	16000
protons	2.36×10^5	2.95×10^4

Figures 14a and 14b show voltage and equilibrium currents, respectively, of a GEO body Under Low-charge plasma condition, where Plasma Electron Current (PEC), Plasma Ion Current (PIC), Secondary Electron Current (SEC), Backscattered Electron Current (BEC), Photoelectric Current (PC) stand for plasma electron current, respectively.

Unlike LEO, photoelectric current is one of the major contributors here, and its absence in shadow region results in large dip in voltage. The body potential is few positive volts in sunlight. On the other hand, for high-charge plasma condition described by Table 8, body voltage is 2.293 volts under sunlit condition, and it is about -50K volts, when in Earth's shadow.

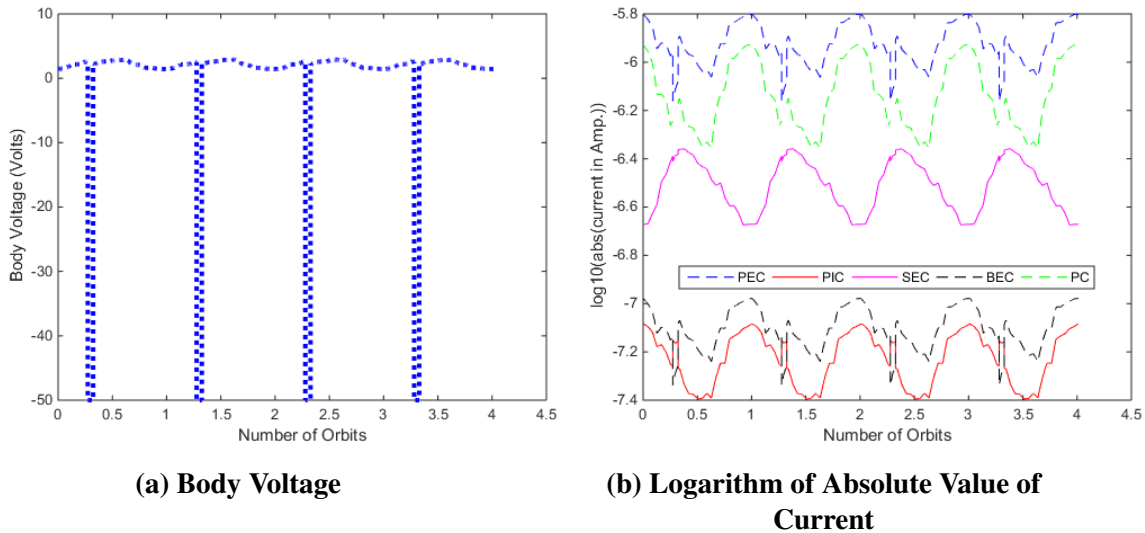
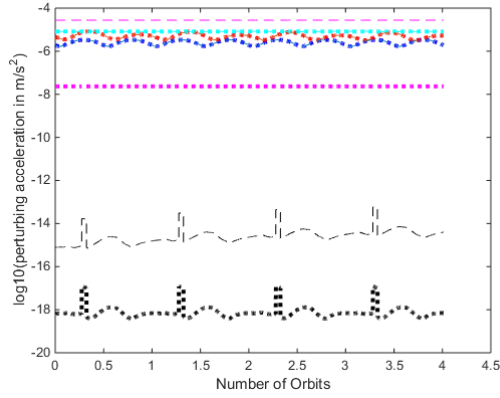
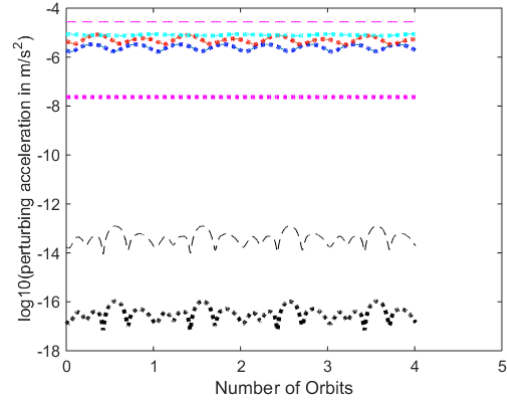


Figure 14. Charging Characteristic of GEO Group 1 (LAMR, Low-Charge Plasma Condition)

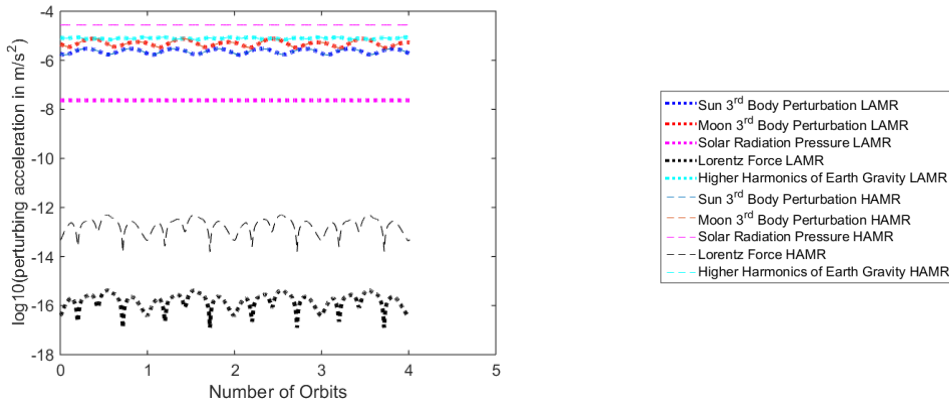
Figure 15 shows the logarithm of magnitudes of perturbing accelerations for GEO orbits. For the LAMR objects, higher harmonics of Earth's gravity and sun/moon third body gravitational perturbations are the dominant contributors to perturbing acceleration; for the HAMR objects, however, solar radiation pressure also becomes one of the major contributors. Lorentz force is still the least dominating factor effecting perturbing acceleration. The sudden jumps in Lorentz perturbation in Figure 15a implies that the object is in Earth's shadow. The jumps in Lorentz perturbation in Figures 15b, 15c are because of magnetic field vector nearly aligning up with the relative velocity vector.



(a) GEO Group 1



(b) GEO Group 2



(c) GEO Group 3

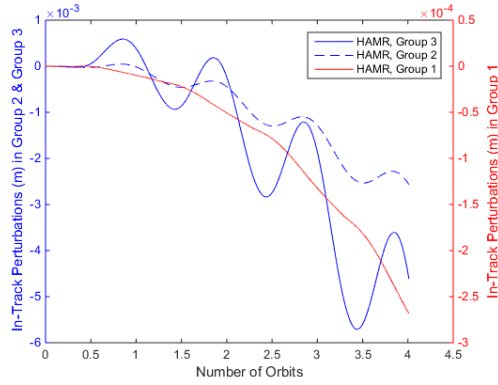
Figure 15. Common Logarithm of Perturbing Acceleration Magnitudes for GEO Orbits, Low-Charge Plasma Condition

Figures 16, 17, 18 show in-track, cross-track and radial perturbations of Lorentz force included orbit relative to Lorentz force excluded orbit, respectively for HAMR objects. Figures 16a, 16b show the in-track perturbations corresponding to low-charge and high-charge plasma conditions respectively. Under both low-charge and high-charge plasma conditions, lowly inclined group 1 orbit exhibits secular increasing trend in in-track direction, whereas higher inclined orbits of group 2 and group 3 exhibit secular decreasing trend in in-track plots. In addition to the secular trend, the in-track perturbations also exhibit a short periodic variation with a period of one day. The increasing secular trend in group 1 in-track perturbation arises because of decreasing semi-major axis of Lorentz force included orbit relative to Lorentz force excluded orbit. Similarly, the decreasing secular trend in higher inclined in-track plots arise out of increasing semi-major axis of Lorentz force included orbit relative to Lorentz force excluded orbit. Since the in-track perturbations for group 1 orbit are positive, object in Lorentz force included orbit lies ahead of object in Lorentz force excluded orbit. By similar logic, object in higher inclined orbits in Lorentz force included orbits, on an average, lags behind object in Lorentz force excluded orbits. For group 1 orbit Under Low-charge plasma conditions, the order of in-track perturbations is 10^{-4} m

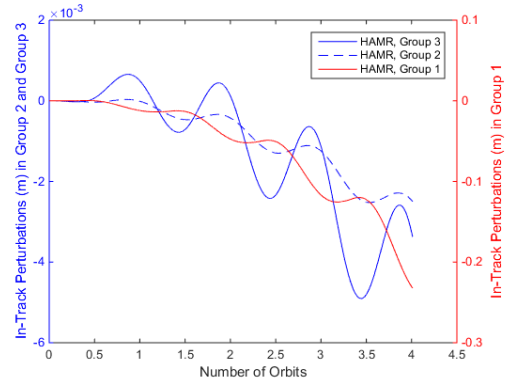
whereas it is an order higher for group 2 and group 3 orbits. Under High-charge plasma conditions, for group 1 orbit, the order of in-track perturbations is 0.3 m, which is three orders of magnitude higher than group 2 and group 3 orbits. This opposite trend for group 1 orbit under High-charge plasma condition is due to body voltage reaching approximately -50K volts in shadow Under High-charge plasma condition; as the simulations are run near equinox, higher inclined orbits do not enter Earth's shadow region and hence do not see a surge in Lorentz force values.

Figures 17a, 17b show cross-track perturbations of Lorentz force included orbit relative to Lorentz force excluded orbit Under Low-charge and high-charge plasma conditions respectively. The cross-track perturbation plots nearly exhibit a zero-mean periodic variation with an approximate period of one day. The zero-mean periodic behavior implies that, on an average, there is no change in orbital plane due to Lorentz force. The amplitudes of the periodic variations in the cross-track perturbations increase with time, and a factor responsible for this increasing behavior is the decreasing RAAN of the Lorentz force included orbit relative to Lorentz force excluded orbit. Between group 2 and group 3 orbits, group 3 orbits exhibit larger amplitudes of variations because of higher inclination. For low-charge plasma conditions, cross-track perturbations are of the order of 10^{-6} m for lowly inclined group 1 orbit, whereas it is two orders of magnitude higher for higher inclined group 2 and group 3 orbits. For group 1 orbit under high-charge plasma conditions, cross-track perturbations are of the order of 10^{-3} m, which is one order of magnitude higher than group 2 and group 3 orbits. The sharp change in slope of group 1 orbit under high-charge plasma condition (near .8 orbital period epoch) corresponds to the body entering Earth's shadow region for the first time.

Figures 18a, 18b show radial perturbations of Lorentz force included orbit relative to Lorentz force excluded orbit Under Low-charge and high-charge plasma conditions respectively. Group 1 radial perturbation plots clearly exhibit a decreasing secular trend superimposed with a periodic variation. The secular trend arises out of decreasing semi-major axis of Lorentz force included orbit relative to Lorentz force excluded orbit. The periodic variation in radial perturbations of group 1 orbit has a time-scale of approximately one day, and the amplitude of variation increases over time. Higher inclined group 2 and group 3 orbits have a small secular (increasing) trend because of increasing relative semi-major axis. Group 2 and group 3 orbits also have a periodic variation of one-day period with increasing amplitude. Also, group 3 orbits have larger amplitudes of variations compared to group 2 orbits. Under Low-charge plasma conditions, group 1 orbit has radial perturbations of the order of 10^{-6} m, which is three orders of magnitude smaller than higher inclined group 2 and group 3 orbits. On the contrary, under high-charge plasma conditions, group 1 orbit has perturbations of the order of 10^{-2} m, which is an order of magnitude larger than higher inclined groups.

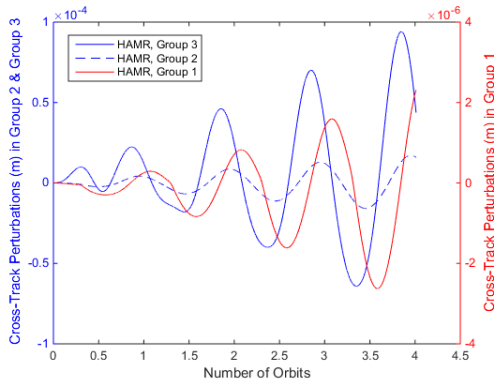


(a) In-Track Perturbations, Low-Charge Condition

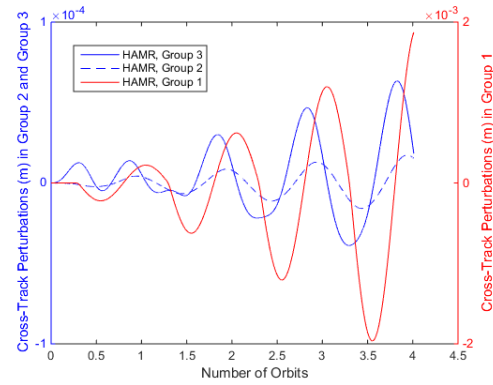


(b) In-Track Perturbations, High-Charge Condition

Figure 16. In-Track Perturbations for Lorentz Force Perturbed GEO Relative to Lorentz Force Excluded Orbit (HAMR Object)

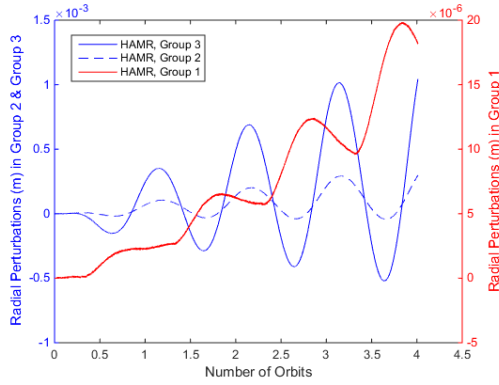


(a) Cross-track Perturbations, Low-charge Condition

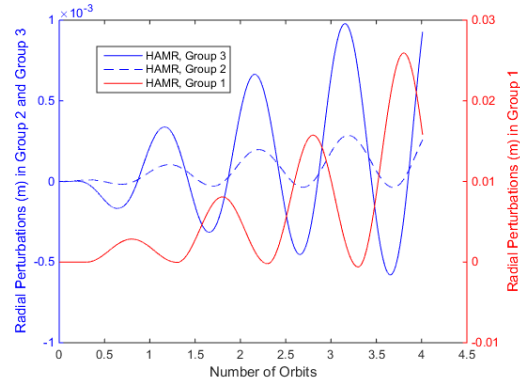


(b) Cross-track Perturbations, High-charge Condition

Figure 17. Cross-Track Perturbations for Lorentz Force Perturbed GEO Relative to Lorentz Force Excluded Orbit (HAMR Object)



(a) Radial Perturbations, Low-Charge Condition



(b) Radial Perturbations, High-Charge Condition

Figure 18. Radial Perturbations for Lorentz Force Perturbed GEO Relative to Lorentz Force Excluded Orbit (HAMR Object)

The in-track, cross-track and radial perturbation differences appear to be less oscillatory for GEO when compared to LEO. The primary reason for this difference is that geosynchronous body completes only four orbits whereas low Earth body completes approximately 62 orbits in four day simulation period.

It is interesting to investigate the orbital element differences of high-charge group 1 orbit because of large voltages in shadow. Figure 19 shows the difference in orbital elements (between Lorentz force included modeling and Lorentz force excluded modeling) for group 1 orbits under high charging plasma condition. The steep changes correspond to the body being in Earth's shadow. The variations in difference in orbital elements (especially, semi-major axis and inclination) in between the jumps is small relative to the scale of the jumps, and hence the apparent flattening.

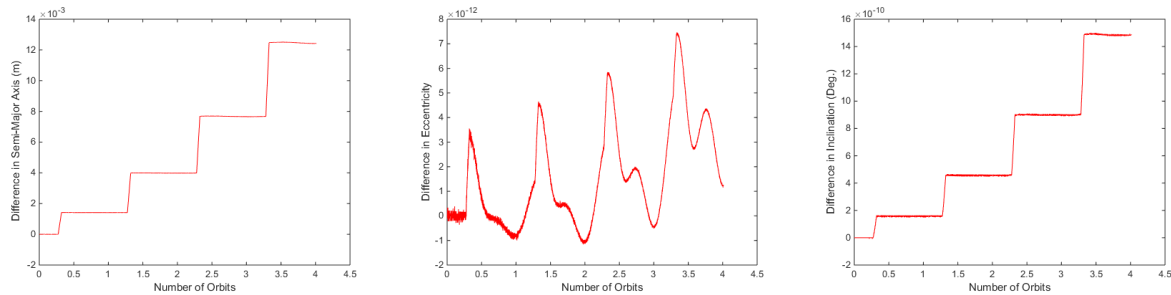


Figure 19. Difference in Semi-Major Axis, Eccentricity and Inclination for Cases With and Without Lorentz Force Modeling. GEO Group 1 Under High-Charge Plasma Condition (HAMR)

Plots corresponding to LAMR objects in GEO are not included here because of their relative small perturbation values when compared to that of HAMR objects. Table 9, however, lists the orders of

in-track, cross-track and radial perturbations of the Lorentz force included orbit relative to Lorentz force excluded orbit for LAMR objects.

Table 9. Orders of Magnitude for In-Track, Cross-Track and Radial Perturbations for LAMR Objects in GEO Over a Period of Four Days

GEO group	In-track perturbations (m)	Cross-track perturbations (m)	Radial Perturbations (m)
Group 1	10^{-7}	10^{-9}	10^{-7}
Group 2	10^{-6}	10^{-7}	10^{-7}
Group 3	10^{-6}	10^{-7}	10^{-6}

4.3 Comparison of Analytic Expressions

Table 10 compares perturbation values obtained using analytic expressions developed in this research [Equations (230) - (234)] with perturbation values obtained using analytic expressions developed by Peng (given in Appendix C). δx ($x \equiv a, e, i, \omega, \Omega$) represents difference in orbital elements (after one orbital-period) between the Lorentz-perturbed and Keplerian orbits. ‘ A_r ’ in the tables stands for analytic expressions developed in this research and ‘ A_p ’ stands for analytic expressions developed by Peng et al. [14]. A constant voltage of -.4 volts and a constant capacitance of 7.72×10^{-9} F are assumed for the LEO object.

Table 10. Values of Orbital Perturbations for LAMR Objects in LEO Under Low-Charge Plasma Conditions

Groups	δa (m)	δe	δi (Deg.)	$\delta \omega$ (Deg.)	$\delta \Omega$ (Deg.)
Group 1	A_r : -1.13E-9	A_r : 1.02E-16	A_r : 3.97E-11	A_r : -3.95E-8	A_r : 4.05E-8
	A_p : -1.21E-9	A_p : -1.26E-21	A_p : 4.27E-11	A_p : -3.98E-8	A_p : 4.08E-8
Group 2	A_r : -6.58 E-7	A_r : 5.72E-14	A_r : 4.31E-11	A_r : -7.36E-10	A_r : -4.82E-10
	A_p : -6.96E-7	A_p : -1.37E-16	A_p : 4.56E-11	A_p : 1.75E-10	A_p : -4.83E-10
Group 3	A_r : -6.55 E-7	A_r : 5.67E-14	A_r : 4.36E-11	A_r : -9.30E-10	A_r : -4.97E-10
	A_p : -6.91E-7	A_p : -1.38E-16	A_p : 4.60E-11	A_p : -3.14E-11	A_p : -4.98E-10

As can be seen from Table 10, there is significant difference between the eccentricity and argument of perigee results. Thorough validation is needed at this point.

5.0 CONCLUSIONS

A detailed modeling of plasma electron and ion currents, backscattered current, secondary current and photoelectric current have been carried out for computing object voltage resulting from the

natural space environment. An approximate space plasma environment modeling has been achieved. With the help of voltage modeling and dipole Earth magnetic field modeling, Lorentz forces acting as orbital perturbations on space objects has been computed. The Lorentz forces are induced by the movement of the objects that acquire charge in the natural space plasma environment. The derivations have been made under the assumption of a spherical conducting object. Appropriate models for Earth gravitational force, Moon and Sun third body gravitational forces, solar radiation pressure and atmospheric drag have also been included. Sample simulations have been made to illustrate the effect of the Lorentz force perturbations representatively for high area-to-mass and low area-to-mass ratio objects, that are spherical aluminum conductors. Simulations in geosyn-chronous Earth orbits and low Earth orbits have been made. Both low-charge plasma condition and high-charge plasma condition have been simulated.

For the geosynchronous region, 75^0 longitude position has been selected for simulation. Among low Earth orbits (altitude ≈ 400 Km), special attention has been paid to sun-synchronous orbits. Effect of area-to-mass ratio and inclination have been studied for both orbit regimes. Effect of Earth's shadow on the evolution of orbital elements has been studied. Comparison of magnitudes of different perturbation forces has been done.

For low Earth low area-to-mass ratio objects under low-charge plasma conditions, in-track perturbations exhibit a distinct secular increasing trend, cross-track perturbations exhibit a near zero-mean periodic variation with increasing amplitude, and the radial perturbations of highly inclined orbits (nearly polar) exhibit a secular decreasing trend. For low Earth low area-to-mass ratio objects under high-charge plasma conditions, in-track perturbations exhibit secular increasing trend for group 2 ($i_i = 89^0$) orbit, and secular decreasing trend for group 3 (sun-synchronous) orbit; the cross-track and radial perturbations exhibit a near-zero mean variation with increasing amplitude values. For geosynchronous high area-to-mass ratio objects, under both low-charge and high-charge plasma conditions, the in-track perturbations exhibit secular decreasing trend, the cross-track perturbations have a periodic variation with near-zero mean, the radial perturbations have a distinct secular increasing trend for lowly inclined (nearly equatorial) orbits whereas the radial perturbations have a small secular increasing trend for higher inclined group 2 ($i_i = 15^0$) and group 3 ($i_i = 40^0$) orbits.

In geosynchronous region, high-charge plasma condition results in transition of voltage from few positive volts in sunlight to approximately -40 kV in shadow. As a result of the high negative voltage, in-track, cross-track and radial perturbations for lowly inclined high area-to-mass ratio object increase by several orders of magnitude as compared to low-charge plasma condition; this also brings in large and steep changes in perturbations of orbital elements. In low Earth region, high-charge plasma condition inside auroral oval results in voltages to the tune of -2.6 kV in sunlight and to the tune of -60 kV in shadow. This results in in-track, cross-track and radial perturbations for low area-to-mass ratio object increase by 3-4 orders of magnitude as compared to low-charge plasma condition.

The variational equations which allow for the derivation of the secular change of the orbital elements due to Lorentz force perturbations have been significantly extended. A thorough validation and in depth understanding of those expressions is the next step in this research. The analytical expressions derived from the variational equations allow for fast long term propagation, however further research is needed.

REFERENCES

- [1] Frueh, Carolin, Kelecy, Thomas, "Coupled Orbit-Attitude Dynamics of High Area-to-Mass Ratio (HAMR) Objects: Influence of Solar Radiation Pressure, Earth's Shadow and the Visibility in Light Curves," *Celestial Mechanics and Dynamical Astronomy*, Vol. 117, No. 4, Dec. 2013, pp 385-404.
- [2] Pines, Samuel, "Uniform Representation of the Gravitational Potential and its Derivatives," *AIAA Journal*, Vol. 11, No. 11, Nov. 1973, pp. 1508-1511.
- [3] Vallado, David A., "Fundamentals of Astrodynamics and Applications," 4th ed., Microcosm Press, Hawthorne, CA, 2013, pp. 1011-1016.
- [4] DeForest, Sherman, E., "Spacecraft Charging at Synchronous Orbit," *Journal of Geophysical Research*, Vol. 77, No. 4, Feb. 1, 1972, pp. 651-659.
- [5] Mullen, E. G., Gussenhoven, M. S., Hardy, D. A., Aggson, T. A., Ledley, B. G. and Whipple, E., "Scatha Survey of High-Level Spacecraft Charging in Sunlight," *Journal of Geophysical Research*, Vol. 91, No. A2, Feb. 1, 1986, pp. 1474-1490.
- [6] Anderson, Phillip C., "Characteristic of Spacecraft Charging in Low Earth Orbit," *Journal of Geophysical Research*, Vol. 117, No. A7, Jul. 2012.
- [7] Lai, Shu T., "Fundamentals of Spacecraft Charging: Spacecraft Interactions with Space Plasmas," Princeton University Press, Princeton and Oxford, 2012.
- [8] Hastings, Daniel, Garrett, Henry, "Spacecraft-Environment Interactions," Cambridge University Press, Cambridge, 1996.
- [9] Mandell, Myron J., Davis, Victoria A., Cooke, David L., Wheelock, Adrian T., "Nascap-2K Spacecraft Charging Code Overview," (online) *Spacecraft Charging Technology Conference*, Albuquerque, New Mexico, Sept. 22, 2010.
- [10] Muranaka, T., Hosoda, S., Kim, J., Hatta, S., Ikeda, K., Hamanaga, T., Cho, M., Usui, H., Ueda, O. H., Koga, K., Goka, T., "Development of Multi-Utility Spacecraft Charging Analysis Tool," *IEEE Transactions on Plasma Science*, Vol. 36, No. 5, Oct. 2008, pp. 2336-2349.
- [11] Clerc, S., Brosse, S., Chane-Yook, M., "SPARCS: An Advanced Software for Spacecraft Charging Analyses," 8th *Spacecraft Charging Technology Conference*, Huntsville, AL, 2004.
- [12] Juhasz, Antal, Horanyi, Mihaly, "Dynamics of Charged Space Debris in the Earth's Plasma Environment," *Journal of Geophysical Research*, Vol. 102, No. A4, Apr. 1, 1997, pp. 7237-7246.
- [13] Abdel-Aziz, Yehia A., "Lorentz Force Effects on the Orbit of a Charged Artificial Satellite: A New Approach," *Applied Mathematics Sciences*, Vol. 1, Nos. 29-32, 2007, pp. 1511-1518.

- [14] Peng, Chao, Gao, Yang, "Lorentz-Force-Perturbed Orbits with Application to J_2 -Invariant Formation," *Acta Astronautica*, Vol. 77, Aug.-Sept. 2012, pp. 12-28. doi: 10.1016/j.actaastro.2012.03.002
- [15] Frueh C., Ferguson D., Lin C., Jah M.K., "Passive Electrostatic Charging of Near-Geosynchronous Space Debris HAMR objects and its Effects on the Coupled Object Dynamics", *AAS/AIAA Space Flight Mechanics Meeting*, Santa Fe, NM, January 26-30, AAS 14-428
- [16] Wertz, J. R., "Spacecraft Attitude Determination and Control," Astrophysics and Space Science Library, Vol. 73, D. Reidel Publishing Company, London, 1978
- [17] Fairfield, Donald H., Mead, Gilbert D., "Magnetospheric Mapping with a Quantitative Geomagnetic Field Model," *Journal of Geophysical Research*, Vol. 80, No. 4, Feb. 1, 1975, pp. 535-542. doi: 10.1029/JA080i004p00535
- [18] Tsyganenko, N. A., Usmanov, A. V., "Determination of the Magnetospheric Current System Parameters and Development of Experimental Geomagnetic Field Models Based on Data from IMP and HEOS Satellites, Planet," *Planetary and Space Science*, Vol. 30, pp. 985-998, Sept. 1982. doi: 10.1016/0032-0633(82)90148-9
- [19] Tsyganenko, N. A., Sitnov, M. I., "Modeling the Dynamics of the Inner Magnetosphere During Strong Geomagnetic Storms," *Journal of Geophysical Research*, Vol. 110, A03208, 2005. doi: 10.1029/2004JA010798
- [20] Olson, W. P., Pfitzer, K. A., "Magnetospheric Magnetic Field Modeling (1977)," Ann. Sci. Rep. F44620-75-C-0033, Air Force Off. of Sci. Res., Arlington, Va.
- [21] Pfitzer, K. A., Olson, W. P., Mogstad, T., "A Time Dependent Source Driven Magnetospheric Magnetic Field Model," EOS, 69, 426, 1988
- [22] Ostapenko, A. A., Maltsev, Y. P., "Relation of the Magnetic Field in the Magnetosphere to the Geomagnetic and Solar Wind Activity," *Journal of Geophysical Research*, Vol. 102, No. A8, Aug. 1, 1997, pp. 17467-17473. doi: 10.1029/97JA00937
- [23] Fairfield, D. H., Tsyganenko, N. A., Usmanov, A. V., Malkov, M. V., "A Large Magnetosphere Magnetic Field Database," *Journal of Geophysical Research*, Vol. 99, No. A6, Jun. 1, 1994, pp. 11319-11326. doi: 10.1029/94JA00255
- [24] Lyon, J. G., Fedder, J. A., Mobarry, C. M., "The Lyon-Fedder-Mobarry (LFM), Global MHD Magnetospheric Simulation Code", *Journal of Atmospheric and Solar-Terrestrial Physics*, Vol. 66, Iss. 15-16, Oct.-Nov. 2004, pp. 1333-1350. doi: 10.1016/j.jastp.2004.03.020
- [25] Garrett, H. B., "The Charging of Spacecraft Surfaces," *Reviews of Geophysics and Space Physics*, Vol. 19, No. 4, Nov. 1981, pp. 577-616. doi: 10.1029/RG019i004p00577
- [26] Reif, F., "Fundamentals of Statistical and Thermal Physics," McGraw-Hill, New York NY, 1965

- [27] Boal, David, "Lectures on Statistical Physics," *Department of Physics, Simon Fraser University*. URL: <http://www.sfu.ca/~boal/445lects/445lec18.pdf>
- [28] Whipple, Elden C, "Potentials of Surfaces in Space," *Rep. Prog. Phys.*, Vol. 44, 1981
- [29] Sternglass, E. J., "Theory of Secondary Electron Emission by High-Speed Ions," *Phys. Rev.*, Vol. 108, No. 1, Oct. 1, 1957
- [30] Archard, G. D., "Back Scattering of Electrons," *Journal of Applied Physics*, Vol. 32, No. 8, Aug. 1961. doi: 10.1063/1.1728385
- [31] Everhart, T. E., "Simple Theory Concerning the Reflection of Electrons from Solids," *Journal of Applied Physics*, Vol. 31, No. 8, Aug. 1960. doi: 10.1063/1.1735868
- [32] Jeanneret, J.B., *photoemission at LHC – a simple model*, CERN/Note 97-48 (AP), 1997
- [33] Powell, C. J., "Analysis of Optical and Inelastic Electron Scattering Data, III. Reflectance Data for Beryllium, Germanium, Antimony and Bismuth," *Journal of the Optical Society of America*, Vol. 60, No. 2, Feb. 1970, pp. 214-220. doi: 10.1364/JOSA.60.000214
- [34] Lai, S. T., Tautz, M. F., "Aspects of Spacecraft Charging in Sunlight," *IEEE Transactions on Plasma Science*, Vol. 34, No. 5, Oct. 2006, pp. 2053-2061
- [35] Fowler, R. H., "The analysis of Photoelectric Sensitivity Curves for Clean Metals at Various Temperatures," *Physical Review*, Vol. 38, Iss. 1, Jul. 1, 1931
- [36] Eagle, Robert, "Lectures on Electricity and Magnetism," DrPhysicsA Youtube channel, <https://www.youtube.com/user/DrPhysicsA>, Last Updated 29 June 2014.
- [37] Moller, K. D., "Optics Learning by Computing, with Model Examples Using Mathcad, Matlab, Mathematica and Maple," 2nd Ed., Springer Science+Business Media, LLC, New York, NY 10013, USA, 2007
- [38] Schulz, L. G., Tangherlini, F. R., "Optical Constants of Silver, Gold, Copper and Aluminum. II. The index of Refraction n," *Journal of the Optical Society of America*, Vol. 44, Iss. 5, May 1954, pp. 362-368. doi: 10.1364/JOSA.44.000362
- [39] Orfanidis, Sophocles J., "Lectures on Electromagnetic Waves and Antennas," Rutgers School of Engineering, www.ece.rutgers.edu/~orfanidi/ewa., n.d.
- [40] Brendel, R., Bormann, D., "An Infrared Dielectric Function Model for Amorphous Solids," *Journal of Applied Physics*, Vol. 71, Iss. 1, 1991. doi: 10.1063/1.350737
- [41] Rakic, A. D., Djurisic, A. B., Elazar, J. M., Majewski, M. L., "Optical Properties of Metallic Films for Vertical-Cavity Optoelectronic Devices," *Applied Optics*, Vol. 37, Iss. 22, 1998, pp. 5271-5283. doi: 10.1364/AO.37.005271
- [42] Cui Chunshi, Goree, J., "Fluctuations of the Charge on a Dust Grain in a Plasma," *IEEE Transactions on Plasma Science*, Vol. 22, No. 2, Apr. 1994.

- [43] Holzworth, R.H., Meng, C.I., “Mathematical Representation of the Auroral Oval,” *Geophysical Research Letters*, Sept. 1975.
- [44] Shepherd, S.G., “Altitude-Adjusted Corrected Geomagnetic Coordinates: Definition and Functional Approximations,” *Journal of Geophysical Research: Space Physics*, Vol. 119, Issue 9, pp. 7501-7521, Sept. 2014.
- [45] Imhof, Christian, Mank, Holger, Lange, Jorg, “Charging Simulations for a Low Earth Orbit Satellite with SPIS Using Different Environment Inputs,” 14th *Spacecraft Charging Technology Conference*, ESA/ESTEC, Noordwijk, NL, Apr. 2016.
- [46] Denton, M. H., Thomsen, M. F., Korth H., Lynch S., Zhang, J. C., Liemohn, M. W., “Bulk Plasma Properties at Geosynchronous Orbit,” *Journal of Geophysical Research*, Vol. 110, Iss. A7, Jul. 2005.

APPENDIX A - GENERAL PERTURBATION COEFFICIENTS

$$C_{80} = 2B_0 \left(\frac{q}{m} \right) \left(\frac{\omega_e a \sin i \sin \theta_m \cos^2 \frac{i}{2}}{\mu(e^2 - 1)} \right) \left[\frac{1}{\left(\frac{\omega_e}{n} - 2 \right)} + \frac{e}{4 \left(\frac{\omega_e}{n} - 1 \right)} + \frac{3e}{4 \left(\frac{\omega_e}{n} - 3 \right)} \right] \quad (\text{A-1})$$

$$C_{81} = -2B_0 \left(\frac{q}{m} \right) \frac{\omega_e a \sin i \sin \theta_m \sin^2 \frac{i}{2}}{\mu(e^2 - 1)} \left[\frac{1}{\left(\frac{\omega_e}{n} + 2 \right)} + \frac{e}{4 \left(\frac{\omega_e}{n} + 1 \right)} + \frac{3e}{4 \left(\frac{\omega_e}{n} + 3 \right)} \right] \quad (\text{A-2})$$

$$C_{82} = 2B_0 \left(\frac{q}{m} \right) \frac{\sin i \sin \theta_m}{na^2(1 - e^2)} \left[\frac{e\omega_e}{2n} \left(\frac{\frac{2\omega_e}{n} - \cos i}{\frac{\omega_e^2 a^3}{\mu} - 1} \right) + \frac{e^3}{(1 - e^2)^{\frac{3}{2}}} \left(\frac{(3 - \frac{\omega_e^2 a^3}{\mu})}{(1 - \frac{\omega_e^2 a^3}{\mu})(9 - \frac{\omega_e^2 a^3}{\mu})} \right) + 1 \right] \quad (\text{A-3})$$

$$\begin{aligned} D_{110} = & B_0 \left(\frac{q}{m} \right) \frac{\omega_e \sin i \sin \theta_m \sin^2 \frac{i}{2}}{4\mu} \left[-\frac{1}{\frac{\omega_e}{n} + 1} + \frac{1}{\frac{\omega_e}{n} + 3} + \frac{e^2}{2 \left(\frac{\omega_e}{n} - 1 \right)} + \frac{e^3}{4 \left(\frac{\omega_e}{n} - 2 \right)} \right] + B_0 \left(\frac{q}{m} \right) \\ & \frac{\sin i \sin \theta_m}{4a^3 n} \left[\frac{e}{(1 - e^2)^{3/2}} + \frac{\omega_e}{n} \right] \left[\frac{e^2}{4 \left(\frac{\omega_e}{n} + 5 \right)} + \frac{e^3}{8 \left(\frac{\omega_e}{n} + 6 \right)} - \frac{\frac{e}{2} - e^3}{\frac{\omega_e}{n} + 4} - \frac{\frac{e^F 2}{4} - 2}{\frac{\omega_e}{n} + 3} \right] + \\ & \frac{B_0 q \sin i \sin \theta_m \left(\frac{7e^3}{8} + \frac{e}{2} \right)}{2m \left(\frac{\omega_e}{n} + 2 \right)} \left[\frac{\omega_e}{\mu} \left(1 - \frac{\cos i}{2} \right) + \frac{e}{2a^3 n (1 - e^2)^{3/2}} \right] - \frac{B_0 \omega_e q \sin i \sin \theta_m \sin^2 \frac{i}{2} \left(\frac{e^2}{4} - 2 \right)}{2m\mu \left(\frac{\omega_e}{n} + 1 \right)} - \\ & \frac{(B_0 q \sin i \sin \theta_m \sin^2 \frac{i}{2} \left(\frac{e}{2} - e^3 \right))}{(2a^3 mn)} \quad (\text{A-4}) \end{aligned}$$

$$\begin{aligned} D_{111} = & B_0 \frac{q \sin i \sin \theta_m \cos^2 \frac{i}{2}}{m \mu} \left[\frac{n(-e^3 + \frac{e}{2})}{2} + \frac{\omega_e(\frac{e^2}{4} - \frac{3}{2})}{2 \left(\frac{\omega_e}{n} - 1 \right)} + \frac{\omega_e(\frac{e^2}{4} - \frac{5}{2})}{2 \left(\frac{\omega_e}{n} - 3 \right)} + \frac{\omega_e(-e^3 + \frac{e}{2})}{2 \left(\frac{\omega_e}{n} - 4 \right)} \right. \\ & \left. - \frac{\omega_e(\frac{7e^3}{8} + \frac{e}{2})}{\frac{\omega_e}{n} - 2} - \frac{e^2 \omega_e}{8 \left(\frac{\omega_e}{n} + 1 \right)} - \frac{e^3 \omega_e}{16 \left(\frac{\omega_e}{n} + 2 \right)} - \frac{e^2 \omega_e}{8 \left(\frac{\omega_e}{n} - 5 \right)} - \frac{e^3 \omega_e}{16 \left(\frac{\omega_e}{n} - 6 \right)} \right] \quad (\text{A-5}) \end{aligned}$$

$$\begin{aligned} D_{112} = & \frac{B_0 q \sin i \sin \theta_m}{2a^3 mn (1 - e^2)^{\frac{3}{2}}} \left[\frac{e^5}{32 \left(\frac{\omega_e}{n} + 6 \right)} + \frac{e^4}{8 \left(\frac{\omega_e}{n} + 5 \right)} + \frac{e^5}{4 \left(\frac{\omega_e}{n} + 4 \right)} + \frac{3e^4}{8 \left(\frac{\omega_e}{n} + 3 \right)} + \frac{13e^5}{32 \left(\frac{\omega_e}{n} + 2 \right)} + \right. \\ & \left. \frac{-1 + e^2 + \frac{e^4}{4}}{\left(\frac{\omega_e}{n} + 1 \right)} + \frac{1 - e^2 - \frac{e^4}{4}}{\left(\frac{\omega_e}{n} - 1 \right)} - \frac{13e^5}{32 \left(\frac{\omega_e}{n} - 2 \right)} - \frac{3e^4}{8 \left(\frac{\omega_e}{n} - 3 \right)} - \frac{e^5}{4 \left(\frac{\omega_e}{n} - 4 \right)} - \frac{e^4}{8 \left(\frac{\omega_e}{n} - 5 \right)} - \frac{e^5}{32 \left(\frac{\omega_e}{n} - 6 \right)} \right] \\ & + \frac{B_0 q \sin i \sin \theta_m}{2a^3 mn} \left(\frac{\omega_e}{n} \right) \left[\frac{e^3}{8 \left(\frac{\omega_e}{n} + 4 \right)} + \frac{e^2}{4 \left(\frac{\omega_e}{n} + 3 \right)} - \frac{\frac{e}{2} - e^3}{\left(\frac{\omega_e}{n} + 2 \right)} + \frac{\cos i}{2 \left(\frac{\omega_e}{n} + 1 \right)} - \frac{\frac{e^2}{4} - 2}{\left(\frac{\omega_e}{n} + 1 \right)} - \frac{\frac{e^2}{4} - 2}{\left(\frac{\omega_e}{n} - 1 \right)} \right. \\ & \left. - \frac{\cos i}{2 \left(\frac{\omega_e}{n} - 1 \right)} - \frac{\frac{e}{2} - e^3}{\left(\frac{\omega_e}{n} - 2 \right)} + \frac{e^2}{4 \left(\frac{\omega_e}{n} - 3 \right)} + \frac{e^3}{8 \left(\frac{\omega_e}{n} - 4 \right)} \right] + \frac{(B_0 q \sin i \sin \theta_m \left(\frac{7e^3}{8} + \frac{e}{2} \right))}{(a^3 mn)} \quad (\text{A-6}) \end{aligned}$$

$$D_{105_4} = -\frac{B_0 \omega_e q \cos \theta_m \sin^2 i \sqrt{1-e^2} (-e^3 + \frac{e}{2})}{amn} \quad (\text{A-7})$$

$$J_1 = \frac{B_0 q \sin \theta_m}{a^3 mn (1-e^2)^{\frac{3}{2}}} \left[-\frac{3e^4 \sin^2 \frac{i}{2}}{32(\frac{\omega_e}{n} + 6)} - \frac{e^3 \sin^2 \frac{i}{2}}{8(\frac{\omega_e}{n} + 5)} - \frac{3e^4 \sin^2 \frac{i}{2}}{8(\frac{\omega_e}{n} + 4)} - \frac{e \sin^2 \frac{i}{2} (\frac{3e^2}{4} + \frac{3}{2})}{2(\frac{\omega_e}{n} + 3)} - \frac{\sin^2 \frac{i}{2} (\frac{9e^4}{16} + 1)}{\frac{\omega_e}{n} + 2} + \frac{e}{4(\frac{\omega_e}{n} + 1)} \left(\cos i \left(\frac{3}{2} - \frac{e^2}{2} \right) - \frac{3e^2}{4} - \frac{3}{2} \right) - \frac{e^3 \sin^2 \frac{i}{2}}{8(\frac{\omega_e}{n} - 1)} - \frac{3e^4 \sin^2 \frac{i}{2}}{32(\frac{\omega_e}{n} - 2)} - \frac{3e^4 \sin^2 \frac{i}{2} n}{8\omega_e} \right] \\ + \frac{B_0 q \sin \theta_m \cos i \sin^2 \frac{i}{2} \omega_e}{a^3 mn^2} \left[\frac{e^2}{4(\frac{\omega_e}{n} + 4)} - \frac{e}{2(\frac{\omega_e}{n} + 3)} + \frac{\frac{e^2}{2} + 1}{\frac{\omega_e}{n} + 2} - \frac{e}{2(\frac{\omega_e}{n} + 1)} + \frac{e^2 n}{4\omega_e} \right] \quad (\text{A-8})$$

$$J_2 = \frac{B_0 q \sin \theta_m \cos^2 \frac{i}{2}}{a^3 mn (1-e^2)^{\frac{3}{2}}} \left[\frac{3e^4}{32(\frac{\omega_e}{n} - 6)} + \frac{e^3}{8(\frac{\omega_e}{n} - 5)} + \frac{3e^4}{8(\frac{\omega_e}{n} - 4)} + \frac{3e(\frac{e^2}{2} + 1)}{4(\frac{\omega_e}{n} - 3)} + \frac{\frac{9e^4}{16} + 1}{\frac{\omega_e}{n} - 2} + \frac{e}{4 \cos^2 \frac{i}{2} (\frac{\omega_e}{n} - 1)} \left(\cos i \left(-\frac{e^2}{2} + \frac{3}{2} \right) + \frac{3e^2}{4} + \frac{3}{2} \right) + \frac{e^3}{8(\frac{\omega_e}{n} + 1)} + \frac{3e^4}{32(\frac{\omega_e}{n} + 2)} + \frac{3e^4 n}{8\omega_e} \right] \\ + \frac{B_0 q \sin \theta_m \cos i \cos^2 \frac{i}{2} \omega_e}{a^3 mn^2} \left[-\frac{e^2}{4(\frac{\omega_e}{n} - 4)} + \frac{e}{2(\frac{\omega_e}{n} - 3)} - \frac{\frac{e^2}{2} + 1}{\frac{\omega_e}{n} - 2} + \frac{e}{2(\frac{\omega_e}{n} - 1)} - \frac{e^2 n}{4\omega_e} \right] \quad (\text{A-9})$$

$$J_3 = \frac{B_0 q \sin \theta_m}{a^3 mn (1-e^2)^{\frac{3}{2}}} \left[-\frac{3e^4}{32(\frac{\omega_e}{n} - 4)} - \frac{e^3}{8(\frac{\omega_e}{n} - 3)} - \frac{3e^4}{8(\frac{\omega_e}{n} - 2)} - \frac{3e(1 + \frac{e^2}{2})}{4(\frac{\omega_e}{n} - 1)} - \frac{3e(1 + \frac{e^2}{2})}{4(\frac{\omega_e}{n} + 1)} - \frac{3e^4}{8(\frac{\omega_e}{n} + 2)} - \frac{e^3}{8(\frac{\omega_e}{n} + 3)} - \frac{3e^4}{32(\frac{\omega_e}{n} + 4)} - \frac{(\frac{9e^4}{16} + 1)n}{\omega_e} \right] + \frac{B_0 q \sin \theta_m \cos i \omega_e}{a^3 mn^2} \left[\frac{e^2}{4(\frac{\omega_e}{n} - 2)} - \frac{e}{2(\frac{\omega_e}{n} - 1)} - \frac{e}{2(\frac{\omega_e}{n} + 1)} + \frac{e^2}{4(\frac{\omega_e}{n} + 2)} + \frac{(\frac{e^2}{2} + 1)n}{\omega_e} \right] \quad (\text{A-10})$$

$$H_4 = -\frac{B_0 e q \cos i \sin \omega \sin \theta_m}{2a^3 mn (1-e^2)^{\frac{3}{2}}} \left[\frac{3e^3}{8(\frac{\omega_e}{n} + 2)} + \frac{1}{(\frac{\omega_e}{n} + 1)} + \frac{e^3}{8(\frac{\omega_e}{n} - 2)} + \frac{e^3}{8(\frac{\omega_e}{n} + 4)} \right] - \frac{3B_0 e^4 q \cos i \sin \omega \sin \theta_m}{16a^3 m \omega_e (1-e^2)^{\frac{3}{2}}} \quad (\text{A-11})$$

$$H_5 = -\frac{B_0 e q \cos i \sin \omega \sin \theta_m}{2a^3 mn (1-e^2)^{\frac{3}{2}}} \left[\frac{3e^3}{8(\frac{\omega_e}{n} - 2)} + \frac{1}{(\frac{\omega_e}{n} - 1)} + \frac{e^3}{8(\frac{\omega_e}{n} + 2)} + \frac{e^3}{8(\frac{\omega_e}{n} - 4)} \right] - \frac{3B_0 e^4 q \cos i \sin \omega \sin \theta_m}{16a^3 m \omega_e (1-e^2)^{\frac{3}{2}}} \quad (\text{A-12})$$

$$E_{202} = \frac{B_0eq \cos \omega \sin \theta_m}{2a^3mn(1-e^2)^{\frac{3}{2}}} \left[\frac{3e^3}{8(\frac{\omega_e}{n}+2)} + \frac{1}{(\frac{\omega_e}{n}+1)} + \frac{e^3}{8(\frac{\omega_e}{n}-2)} + \frac{e^3}{8(\frac{\omega_e}{n}+4)} \right] + \frac{3B_0e^4q \cos \omega \sin \theta_m}{16a^3m\omega_e(1-e^2)^{\frac{3}{2}}} \quad (\text{A-13})$$

$$E_{203} = -\frac{B_0eq \cos \omega \sin \theta_m}{2a^3mn(1-e^2)^{\frac{3}{2}}} \left[\frac{3e^3}{8(\frac{\omega_e}{n}-2)} + \frac{1}{(\frac{\omega_e}{n}-1)} + \frac{e^3}{8(\frac{\omega_e}{n}+2)} + \frac{e^3}{8(\frac{\omega_e}{n}-4)} \right] - \frac{3B_0e^4q \cos \omega \sin \theta_m}{16a^3m\omega_e(1-e^2)^{\frac{3}{2}}} \quad (\text{A-14})$$

$$I_{12} = \frac{3B_0e^4q \cos \theta_m \sin i}{8am(e^2-1)} + \frac{B_0e^2\omega_eq \sin 2i \cos \theta_m \sqrt{1-e^2}}{4amn} \quad (\text{A-15})$$

$$N_1 = \frac{B_0q \sin \theta_m \sin^2 \frac{i}{2}}{a^3mn \sin i (1-e^2)^{\frac{3}{2}}} \left[\frac{3e^4}{32(\frac{\omega_e}{n}+6)} + \frac{e^3}{8(\frac{\omega_e}{n}+5)} + \frac{3e^4}{8(\frac{\omega_e}{n}+4)} + \frac{3e(\frac{e^2}{2}+1)}{4(\frac{\omega_e}{n}+3)} + \frac{1+\frac{9e^4}{16}}{(\frac{\omega_e}{n}+2)} \right. \\ \left. + \frac{3e(1+\frac{e^2}{2})}{4(\frac{\omega_e}{n}+1)} + \frac{e^3}{8(\frac{\omega_e}{n}-1)} + \frac{3e^4}{32(\frac{\omega_e}{n}-2)} + \frac{3e^4n}{8\omega_e} \right] + \frac{B_0q \sin \theta_m \omega_e \cos i \sin^2 \frac{i}{2}}{a^3mn^2 \sin i} \left[-\frac{e^2}{4(\frac{\omega_e}{n}+4)} \right. \\ \left. + \frac{e}{2(\frac{\omega_e}{n}+3)} - \frac{\frac{e^2}{2}+1}{(\frac{\omega_e}{n}+2)} + \frac{e}{2(\frac{\omega_e}{n}+1)} - \frac{e^2n}{4\omega_e} \right] \quad (\text{A-16})$$

$$N_2 = \frac{B_0q \sin \theta_m \cos^2 \frac{i}{2}}{a^3mn \sin i (1-e^2)^{\frac{3}{2}}} \left[-\frac{3e^4}{32(\frac{\omega_e}{n}-6)} - \frac{e^3}{8(\frac{\omega_e}{n}-5)} - \frac{3e^4}{8(\frac{\omega_e}{n}-4)} - \frac{3e(1+\frac{e^2}{2})}{4(\frac{\omega_e}{n}-3)} - \frac{\frac{9e^4}{16}+1}{(\frac{\omega_e}{n}-2)} \right. \\ \left. - \frac{3e(1+\frac{e^2}{2})}{4(\frac{\omega_e}{n}-1)} - \frac{e^3}{8(\frac{\omega_e}{n}+1)} - \frac{3e^4}{32(\frac{\omega_e}{n}+2)} - \frac{3e^4n}{8\omega_e} \right] + \frac{B_0q \sin \theta_m \omega_e \cos i \cos^2 \frac{i}{2}}{a^3mn^2 \sin i} \left[\frac{e^2}{4(\frac{\omega_e}{n}-4)} \right. \\ \left. - \frac{e}{2(\frac{\omega_e}{n}-3)} + \frac{1+\frac{e^2}{2}}{(\frac{\omega_e}{n}-2)} - \frac{e}{2(\frac{\omega_e}{n}-1)} + \frac{e^2n}{4\omega_e} \right] \quad (\text{A-17})$$

$$N_3 = \frac{B_0q \sin \theta_m \cos i}{a^3mn \sin i (1-e^2)^{\frac{3}{2}}} \left[\frac{3e^4}{8(\frac{\omega_e}{n}+2)} + \frac{3e(1+\frac{e^2}{2})}{4(\frac{\omega_e}{n}+1)} + \frac{3e(1+\frac{e^2}{2})}{4(\frac{\omega_e}{n}-1)} + \frac{3e^4}{8(\frac{\omega_e}{n}-2)} + \frac{e^3}{8(\frac{\omega_e}{n}-3)} \right. \\ \left. + \frac{3e^4}{32(\frac{\omega_e}{n}-4)} + \frac{e^3}{8(\frac{\omega_e}{n}+3)} + \frac{3e^4}{32(\frac{\omega_e}{n}+4)} + \frac{(\frac{9e^4}{16}+1)n}{\omega_e} \right] + \frac{B_0q \sin \theta_m \omega_e \cos^2 i}{a^3mn^2 \sin i} \left[-\frac{e^2}{4(\frac{\omega_e}{n}+2)} \right. \\ \left. + \frac{e}{2(\frac{\omega_e}{n}+1)} + \frac{e}{2(\frac{\omega_e}{n}-1)} - \frac{e^2}{4(\frac{\omega_e}{n}-2)} - \frac{(\frac{e^2}{2}+1)n}{\omega_e} \right] \quad (\text{A-18})$$

$$L_{177} = -\frac{B_0eq \cos \omega \sin \theta_m}{2a^3mn \sin i (1-e^2)^{\frac{3}{2}}} \left[\frac{3e^3n}{8\omega_e} + \frac{3e^3}{8(\frac{\omega_e}{n}+2)} + \frac{1}{(\frac{\omega_e}{n}+1)} + \frac{e^3}{8(\frac{\omega_e}{n}-2)} + \frac{e^3}{8(\frac{\omega_e}{n}+4)} \right] \quad (\text{A-19})$$

$$L_{178} = \frac{B_0eq \cos \omega \sin \theta_m}{2a^3mn \sin i (1-e^2)^{\frac{3}{2}}} \left[\frac{3e^3n}{8\omega_e} + \frac{3e^3}{8(\frac{\omega_e}{n}-2)} + \frac{1}{(\frac{\omega_e}{n}-1)} + \frac{e^3}{8(\frac{\omega_e}{n}+2)} + \frac{e^3}{8(\frac{\omega_e}{n}-4)} \right] \quad (\text{A-20})$$

$$J_{180} = -\frac{B_0eq \cos i \sin \omega \sin \theta_m}{2a^3mn \sin i (1-e^2)^{\frac{3}{2}}} \left[\frac{3e^3n}{8\omega_e} + \frac{3e^3}{8(\frac{\omega_e}{n}+2)} + \frac{1}{(\frac{\omega_e}{n}+1)} + \frac{e^3}{8(\frac{\omega_e}{n}-2)} + \frac{e^3}{8(\frac{\omega_e}{n}+4)} \right] \quad (\text{A-21})$$

$$J_{181} = -\frac{B_0eq \cos i \sin \omega \sin \theta_m}{2a^3mn \sin i (1-e^2)^{\frac{3}{2}}} \left[\frac{3e^3n}{8\omega_e} + \frac{3e^3}{8(\frac{\omega_e}{n}-2)} + \frac{1}{(\frac{\omega_e}{n}-1)} + \frac{e^3}{8(\frac{\omega_e}{n}+2)} + \frac{e^3}{8(\frac{\omega_e}{n}-4)} \right] \quad (\text{A-22})$$

$$\frac{K_6\pi}{na^2\sqrt{1-e^2}} \left[K_{11} + K_{13} \sin \omega \right] = -\frac{(\frac{e^2}{2}+1)\pi B_0q \cos \theta_m}{na^3m(1-e^2)^{\frac{3}{2}}} \left[2 + \frac{3e^2}{4} - \frac{\omega_e \sin 2i (1-e^2)^{\frac{3}{2}}}{n \sin i} + \frac{e^2 \sin^2 \omega}{2} \right] \quad (\text{A-23})$$

$$\frac{2\pi K_9}{na^2\sqrt{1-e^2}} \left[\frac{K_{12}}{2} + K_2 \sin \omega + K_{14} \sin^2 \omega \right] = \frac{\pi e^2 B_0q \cos \theta_m}{2na^3m(1-e^2)^{\frac{3}{2}}} \left[\frac{5}{2} + 3 \sin^2 \omega \right] \quad (\text{A-24})$$

$$\frac{\pi K_{10}}{na^2\sqrt{1-e^2}} \left[K_{15} - K_{11} \cos 2\omega + K_{13} \sin \omega \right] = -\frac{\pi e^2 B_0q \cos \theta_m}{4na^3m(1-e^2)^{\frac{3}{2}}} \left[\frac{3e^2}{4} - 2 \cos 2\omega - \frac{3e^2 \cos 2\omega}{4} + \frac{\omega_e \sin 2i (1-e^2)^{\frac{3}{2}} \cos 2\omega}{n \sin i} + \frac{e^2 \sin^2 \omega}{2} \right] \quad (\text{A-25})$$

$$\begin{aligned} Q_{142} = & -\frac{B_0q \sin \theta_m \cos i \sin^2 \frac{i}{2}}{a^3mn \sin i (1-e^2)^{\frac{3}{2}}} \left[\frac{3e^4}{32(\frac{\omega_e}{n}+6)} + \frac{e^3}{8(\frac{\omega_e}{n}+5)} + \frac{3e^4}{8(\frac{\omega_e}{n}+4)} + \frac{3e(\frac{e^2}{2}+1)}{4(\frac{\omega_e}{n}+3)} + \frac{1+\frac{9e^4}{16}}{(\frac{\omega_e}{n}+2)} \right. \\ & + \frac{3e(1+\frac{e^2}{2})}{4(\frac{\omega_e}{n}+1)} + \frac{e^3}{8(\frac{\omega_e}{n}-1)} + \frac{3e^4}{32(\frac{\omega_e}{n}-2)} + \left. \frac{3e^4n}{8\omega_e} \right] - \frac{B_0q \sin \theta_m \omega_e \cos^2 i \sin^2 \frac{i}{2}}{a^3mn^2 \sin i} \left[-\frac{e^2}{4(\frac{\omega_e}{n}+4)} \right. \\ & + \frac{e}{2(\frac{\omega_e}{n}+3)} - \frac{\frac{e^2}{2}+1}{(\frac{\omega_e}{n}+2)} + \frac{e}{2(\frac{\omega_e}{n}+1)} - \left. \frac{e^2n}{4\omega_e} \right] + \frac{B_0\omega_e q \sin i \sin \theta_m \sin^2 \frac{i}{2}}{4a^3mn^2} \left[-\frac{e}{2(\frac{\omega_e}{n}+5)} + \frac{(3+\frac{e^2}{2})}{e(\frac{\omega_e}{n}+1)} \right] \end{aligned}$$

$$+ \frac{1}{\left(\frac{\omega_e}{n} + 4\right)} - \frac{5 + \frac{e^2}{2}}{e\left(\frac{\omega_e}{n} + 3\right)} + \frac{e}{2\left(\frac{\omega_e}{n} - 1\right)} \left] - \frac{B_0 q \sin i \sin \theta_m \sin^2 \frac{i}{2}}{4a^3 mn} \quad (\text{A-26})$$

$$\begin{aligned} Q_{143} = & -\frac{B_0 q \sin \theta_m \cos^2 \frac{i}{2} \cos i}{a^3 mn \sin i (1 - e^2)^{\frac{3}{2}}} \left[-\frac{3e^4}{32\left(\frac{\omega_e}{n} - 6\right)} - \frac{e^3}{8\left(\frac{\omega_e}{n} - 5\right)} - \frac{3e^4}{8\left(\frac{\omega_e}{n} - 4\right)} - \frac{3e(1 + \frac{e^2}{2})}{4\left(\frac{\omega_e}{n} - 3\right)} - \frac{\frac{9e^4}{16} + 1}{\left(\frac{\omega_e}{n} - 2\right)} \right. \\ & - \frac{3e(1 + \frac{e^2}{2})}{4\left(\frac{\omega_e}{n} - 1\right)} - \frac{e^3}{8\left(\frac{\omega_e}{n} + 1\right)} - \frac{3e^4}{32\left(\frac{\omega_e}{n} + 2\right)} - \left. \frac{3e^4 n}{8\omega_e} \right] - \frac{B_0 q \sin \theta_m \omega_e \cos^2 i \cos^2 \frac{i}{2}}{a^3 mn^2 \sin i} \left[\frac{e^2}{4\left(\frac{\omega_e}{n} - 4\right)} - \frac{e}{2\left(\frac{\omega_e}{n} - 3\right)} \right. \\ & + \frac{1 + \frac{e^2}{2}}{\left(\frac{\omega_e}{n} - 2\right)} - \frac{e}{2\left(\frac{\omega_e}{n} - 1\right)} + \frac{e^2 n}{4\omega_e} \left] + \frac{B_0 \omega_e q \sin i \sin \theta_m \cos^2 \frac{i}{2}}{4a^3 mn^2} \left[\frac{e}{2\left(\frac{\omega_e}{n} - 5\right)} - \frac{1}{\left(\frac{\omega_e}{n} - 4\right)} + \frac{(5 + \frac{e^2}{2})}{e\left(\frac{\omega_e}{n} - 3\right)} \right. \\ & - \left. \frac{(3 + \frac{e^2}{2})}{e\left(\frac{\omega_e}{n} - 1\right)} - \frac{e}{2\left(\frac{\omega_e}{n} + 1\right)} \right] + \frac{B_0 q \sin i \sin \theta_m \cos^2 \frac{i}{2}}{4a^3 mn} \quad (\text{A-27}) \end{aligned}$$

$$\begin{aligned} Q_{144} = & -\frac{B_0 q \sin \theta_m \cos^2 i}{a^3 mn \sin i (1 - e^2)^{\frac{3}{2}}} \left[\frac{3e^4}{8\left(\frac{\omega_e}{n} + 2\right)} + \frac{3e(1 + \frac{e^2}{2})}{4\left(\frac{\omega_e}{n} + 1\right)} + \frac{3e(1 + \frac{e^2}{2})}{4\left(\frac{\omega_e}{n} - 1\right)} + \frac{3e^4}{8\left(\frac{\omega_e}{n} - 2\right)} + \frac{e^3}{8\left(\frac{\omega_e}{n} - 3\right)} \right. \\ & + \frac{3e^4}{32\left(\frac{\omega_e}{n} - 4\right)} + \frac{e^3}{8\left(\frac{\omega_e}{n} + 3\right)} + \frac{3e^4}{32\left(\frac{\omega_e}{n} + 4\right)} + \left. \frac{(\frac{9e^4}{16} + 1)n}{\omega_e} \right] - \frac{B_0 q \sin \theta_m \omega_e \cos^3 i}{a^3 mn^2 \sin i} \left[-\frac{e^2}{4\left(\frac{\omega_e}{n} + 2\right)} \right. \\ & + \frac{e}{2\left(\frac{\omega_e}{n} + 1\right)} + \frac{e}{2\left(\frac{\omega_e}{n} - 1\right)} - \frac{e^2}{4\left(\frac{\omega_e}{n} - 2\right)} - \left. \frac{(\frac{e^2}{2} + 1)n}{\omega_e} \right] + \frac{B_0 q \sin i \sin \theta_m}{a^3 mn (1 - e^2)^{\frac{3}{2}}} \left[-\frac{e^3}{32\left(\frac{\omega_e}{n} - 5\right)} - \frac{e^3}{32\left(\frac{\omega_e}{n} - 3\right)} \right. \\ & + \frac{(\frac{e^3}{8} + e + \frac{1}{e})}{2\left(\frac{\omega_e}{n} - 1\right)} + \frac{(\frac{e^3}{8} + e + \frac{1}{e})}{2\left(\frac{\omega_e}{n} + 1\right)} - \frac{e^3}{32\left(\frac{\omega_e}{n} + 3\right)} - \frac{e^3}{32\left(\frac{\omega_e}{n} + 5\right)} + \frac{2n}{\omega_e} \left] + \frac{B_0 \omega_e q \sin i \sin \theta_m}{2a^3 mn^2} \left[\frac{e}{4\left(\frac{\omega_e}{n} - 3\right)} \right. \\ & - \frac{1}{2\left(\frac{\omega_e}{n} - 2\right)} + \frac{(\frac{e^2}{4} + 2 - \frac{\cos i}{2})}{e\left(\frac{\omega_e}{n} - 1\right)} - \frac{(2 + \frac{e^2}{4} + \frac{\cos i}{2})}{e\left(\frac{\omega_e}{n} + 1\right)} + \frac{1}{2\left(\frac{\omega_e}{n} + 2\right)} - \left. \frac{e}{4\left(\frac{\omega_e}{n} + 3\right)} \right] \quad (\text{A-28}) \end{aligned}$$

$$Q_{145} = \frac{B_0 e q \cos \omega \sin \theta_m \cos i}{2a^3 mn \sin i (1 - e^2)^{\frac{3}{2}}} \left[\frac{3e^3 n}{8\omega_e} + \frac{3e^3}{8\left(\frac{\omega_e}{n} + 2\right)} + \frac{1}{\left(\frac{\omega_e}{n} + 1\right)} + \frac{e^3}{8\left(\frac{\omega_e}{n} - 2\right)} + \frac{e^3}{8\left(\frac{\omega_e}{n} + 4\right)} \right] \quad (\text{A-29})$$

$$Q_{146} = -\frac{B_0 e q \cos \omega \sin \theta_m \cos i}{2a^3 mn \sin i (1 - e^2)^{\frac{3}{2}}} \left[\frac{3e^3 n}{8\omega_e} + \frac{3e^3}{8\left(\frac{\omega_e}{n} - 2\right)} + \frac{1}{\left(\frac{\omega_e}{n} - 1\right)} + \frac{e^3}{8\left(\frac{\omega_e}{n} + 2\right)} + \frac{e^3}{8\left(\frac{\omega_e}{n} - 4\right)} \right] \quad (\text{A-30})$$

$$Q_{147} = \frac{B_0 e q \cos^2 i \sin \omega \sin \theta_m}{2a^3 mn \sin i (1 - e^2)^{\frac{3}{2}}} \left[\frac{3e^3 n}{8\omega_e} + \frac{3e^3}{8\left(\frac{\omega_e}{n} + 2\right)} + \frac{1}{\left(\frac{\omega_e}{n} + 1\right)} + \frac{e^3}{8\left(\frac{\omega_e}{n} - 2\right)} + \frac{e^3}{8\left(\frac{\omega_e}{n} + 4\right)} \right] \quad (\text{A-31})$$

$$Q_{148} = \frac{B_0 e q \cos^2 i \sin \omega \sin \theta_m}{2a^3 m n \sin i (1 - e^2)^{\frac{3}{2}}} \left[\frac{3e^3 n}{8\omega_e} + \frac{3e^3}{8(\frac{\omega_e}{n} - 2)} + \frac{1}{(\frac{\omega_e}{n} - 1)} + \frac{e^3}{8(\frac{\omega_e}{n} + 2)} + \frac{e^3}{8(\frac{\omega_e}{n} - 4)} \right] \quad (\text{A-32})$$

$$\frac{Q_{149} \pi}{na^2 \sqrt{1 - e^2}} (K_{11} + K_{13} \sin \omega) = \frac{(\frac{e^2}{2} + 1) \pi B_0 q \cos \theta_m \cos i}{na^3 m (1 - e^2)^{\frac{3}{2}}} \left[2 + \frac{3e^2}{4} - \frac{\omega_e \sin 2i (1 - e^2)^{\frac{3}{2}}}{n \sin i} + \frac{e^2 \sin^2 \omega}{2} \right] \quad (\text{A-33})$$

$$\frac{2\pi Q_{150}}{na^2 \sqrt{1 - e^2}} \left[\frac{K_{12}}{2} + K_2 \sin \omega + K_{14} \sin^2 \omega \right] = -\frac{\pi e^2 B_0 q \cos \theta_m \cos i}{2na^3 m (1 - e^2)^{\frac{3}{2}}} \left[\frac{5}{2} + 3 \sin^2 \omega \right] \quad (\text{A-34})$$

$$\frac{\pi Q_{151}}{na^2 \sqrt{1 - e^2}} \left[K_{15} - K_{11} \cos 2\omega + K_{13} \sin \omega \right] = \frac{\pi e^2 B_0 q \cos \theta_m \cos i}{4na^3 m (1 - e^2)^{\frac{3}{2}}} \left[\frac{3e^2}{4} - 2 \cos 2\omega - \frac{3e^2 \cos 2\omega}{4} + \frac{\omega_e \sin 2i (1 - e^2)^{\frac{3}{2}} \cos 2\omega}{n \sin i} + \frac{e^2 \sin^2 \omega}{2} \right] \quad (\text{A-35})$$

$$\frac{\pi}{na^2 \sqrt{1 - e^2}} \left[Q_{43} + Q_{131} Q_{133} + \frac{Q_{131} Q_{134} e}{2} + Q_{132} Q_{134} \cos 2\omega \right] = \frac{\pi B_0 q \cos \theta_m}{na^3 m (1 - e^2)^{\frac{3}{2}}} \left[4 \cos i - \frac{\omega_e}{2n} \cos 2\omega \sin^2 i (1 - e^2)^{\frac{3}{2}} \right] \quad (\text{A-36})$$

—

—

—

APPENDIX B - LEO PERTURBATION COEFFICIENTS

$$C_{80} = B_0 \left(\frac{q}{m} \right) \left(\frac{\omega_e a \sin i \cos^2 \frac{i}{2} \sin \theta_m}{\mu} \right) \quad (\text{B-1})$$

$$C_{81} = B_0 \left(\frac{q}{m} \right) \left(\frac{\omega_e a \sin i \sin^2 \frac{i}{2} \sin \theta_m}{\mu} \right) \quad (\text{B-2})$$

$$C_{82} = 2B_0 \left(\frac{q}{m} \right) \left(\frac{\sin i \sin \theta_m}{na^2} \right) \quad (\text{B-3})$$

$$D_{110} = \frac{1}{6} B_0 \left(\frac{q}{m} \right) \frac{\omega_e \sin i \sin \theta_m}{\mu} \left[5 \sin^2 \frac{i}{2} + 1 \right] \quad (\text{B-4})$$

$$D_{111} = \frac{7}{6} B_0 \left(\frac{q}{m} \right) \frac{\sin i \sin \theta_m \cos^2 \frac{i}{2} \omega_e}{\mu} \quad (\text{B-5})$$

$$D_{112} = -\frac{B_0 q \sin i \sin \theta_m n}{m \mu} \quad (\text{B-6})$$

$$D_{1054} = -\frac{B_0 \omega_e q \cos \theta_m \sin^2 i e}{2 a m n} \quad (\text{B-7})$$

$$J_1 = -\frac{B_0 q \sin \theta_m \sin^2 \frac{i}{2}}{2 a^3 m n} \quad (\text{B-8})$$

$$J_2 = -\frac{B_0 q \sin \theta_m \cos^2 \frac{i}{2}}{2 a^3 m n} \quad (\text{B-9})$$

$$J_3 = \frac{B_0 q \sin \theta_m}{a^3 m \omega_e} \left[-1 + \frac{\cos i \omega_e}{n} \right] \quad (\text{B-10})$$

$$H_4 = -\frac{B_0 e q \cos i \sin \omega \sin \theta_m}{2 a^3 m n} \quad (\text{B-11})$$

$$H_5 = \frac{B_0 e q \cos i \sin \omega \sin \theta_m}{2 a^3 m n} \quad (\text{B-12})$$

$$E_{202} = \frac{B_0 e q \cos \omega \sin \theta_m}{2 a^3 m n} \quad (\text{B-13})$$

$$E_{203} = \frac{B_0 e q \cos \omega \sin \theta_m}{2 a^3 m n} \quad (\text{B-14})$$

$$I_{12} = \frac{B_0 e^2 \omega_e q \sin 2i \cos \theta_m}{4 a m n} \quad (\text{B-15})$$

$$N_1 = \frac{B_0 q \sin \theta_m \sin^2 \frac{i}{2}}{2 a^3 m n \sin i} \quad (\text{B-16})$$

$$N_2 = \frac{B_0 q \sin \theta_m \cos^2 \frac{i}{2}}{2 a^3 m n \sin i} \quad (\text{B-17})$$

$$N_3 = \frac{B_0 q \sin \theta_m \cos i}{a^3 m \sin i \omega_e} \left(1 - \frac{\omega_e}{n} \cos i \right) \quad (\text{B-18})$$

$$L_{177} = -\frac{B_0 e q \cos \omega \sin \theta_m}{2 a^3 m n \sin i} \quad (\text{B-19})$$

$$L_{178} = -\frac{B_0 e q \cos \omega \sin \theta_m}{2 a^3 m n \sin i} \quad (\text{B-20})$$

$$J_{180} = -\frac{B_0 e q \cos i \sin \omega \sin \theta_m}{2 a^3 m n \sin i} \quad (\text{B-21})$$

$$J_{181} = \frac{B_0 e q \cos i \sin \omega \sin \theta_m}{2a^3 m n \sin i} \quad (\text{B-22})$$

$$\frac{K_6 \pi}{na^2 \sqrt{1-e^2}} \left[K_{11} + K_{13} \sin \omega \right] = -\frac{2\pi B_0 q \cos \theta_m}{na^3 m} \quad (\text{B-23})$$

$$\frac{2\pi K_9}{na^2 \sqrt{1-e^2}} \left[\frac{K_{12}}{2} + K_2 \sin \omega + K_{14} \sin^2 \omega \right] = \frac{\pi e^2 B_0 q \cos \theta_m}{2na^3 m (1-e^2)^{\frac{3}{2}}} \left[\frac{5}{2} + 3 \sin^2 \omega \right] \quad (\text{B-24})$$

$$\frac{\pi K_{10}}{na^2 \sqrt{1-e^2}} \left[K_{15} - K_{11} \cos 2\omega + K_{13} \sin \omega \right] = \frac{\pi e^2 B_0 q \cos \theta_m \cos 2\omega}{2a^3 m n} \quad (\text{B-25})$$

$$Q_{142} = -\frac{B_0 q \sin \theta_m \sin^2 \frac{i}{2} \cos i}{2a^3 m n \sin i} + \frac{B_0 q \sin i \sin \theta_m \sin^2 \frac{i}{2}}{4a^3 m n} \left(\frac{4\omega_e}{3ne} - 1 \right) \quad (\text{B-26})$$

$$Q_{143} = -\frac{B_0 q \sin \theta_m \cos i \cos^2 \frac{i}{2}}{2a^3 m n \sin i} + \frac{B_0 q \sin i \sin \theta_m \cos^2 \frac{i}{2}}{4a^3 m n} \left[\frac{4\omega_e}{3ne} + 1 \right] \quad (\text{B-27})$$

$$Q_{144} = -\frac{B_0 q \sin \theta_m \cos^2 i}{\omega_e a^3 m \sin i} \left(1 - \frac{\omega_e \cos i}{n} \right) + \frac{2B_0 q \sin i \sin \theta_m}{a^3 m n} \left(\frac{n}{\omega_e} - \frac{\omega_e}{ne} \right) \quad (\text{B-28})$$

$$Q_{145} = \frac{B_0 e q \cos \omega \cos i \sin \theta_m}{2a^3 m n \sin i} \quad (\text{B-29})$$

$$Q_{146} = \frac{B_0 e q \cos \omega \cos i \sin \theta_m}{2a^3 m n \sin i} \quad (\text{B-30})$$

$$Q_{147} = \frac{B_0 e q \cos^2 i \sin \omega \sin \theta_m}{2a^3 m n \sin i} \quad (\text{B-31})$$

$$Q_{148} = -\frac{B_0 e q \cos^2 i \sin \omega \sin \theta_m}{2a^3 m n \sin i} \quad (\text{B-32})$$

$$\frac{Q_{149} \pi}{na^2 \sqrt{1-e^2}} (K_{11} + K_{13} \sin \omega) = \frac{2\pi B_0 q \cos \theta_m \cos i}{na^3 m} \quad (\text{B-33})$$

$$\frac{2\pi Q_{150}}{na^2 \sqrt{1-e^2}} \left[\frac{K_{12}}{2} + K_2 \sin \omega + K_{14} \sin^2 \omega \right] = -\frac{\pi e^2 B_0 q \cos \theta_m \cos i}{2na^3 m (1-e^2)^{\frac{3}{2}}} \left[\frac{5}{2} + 3 \sin^2 \omega \right] \quad (\text{B-34})$$

$$\frac{\pi Q_{151}}{na^2 \sqrt{1-e^2}} \left[K_{15} - K_{11} \cos 2\omega + K_{13} \sin \omega \right] = -\frac{\pi e^2 B_0 q \cos \theta_m \cos 2\omega \cos i}{2a^3 m n} \quad (\text{B-35})$$

$$\begin{aligned} \frac{\pi}{na^2 \sqrt{1-e^2}} \left[Q_{43} + Q_{131} Q_{133} + \frac{Q_{131} Q_{134} e}{2} + Q_{132} Q_{134} \cos 2\omega \right] &= \frac{\pi B_0 q \cos \theta_m}{na^3 m (1-e^2)^{\frac{3}{2}}} \left[4 \cos i - \right. \\ &\quad \left. \frac{\omega_e}{2n} \cos 2\omega \sin^2 i (1-e^2)^{\frac{3}{2}} \right] \quad (\text{B-36}) \end{aligned}$$

$$\frac{\Delta a}{T_{period}} = 2 \left(\frac{q}{m} \right) B_0 \frac{\omega_e}{\sqrt{\mu a}} \frac{\sin i}{(1-e^2)} \hat{N}_x \quad (C-1)$$

$$\begin{aligned} \frac{\Delta e}{T_{period}} = & \left(\frac{q}{m} \right) B_0 \frac{\omega_e}{\sqrt{\mu a^3}} \frac{\sin i}{e^3 \sqrt{1-e^2}} \left[3e^2 \sqrt{1-e^2} + 4 \cos^2 \omega (1-e^2)^{3/2} + 6e^2 \cos^2 \omega + 2e^4 \sin^2 \omega \right. \\ & \left. - 4 \cos^2 \omega + 2 - 4e^2 - 2\sqrt{1-e^2} \right] \hat{N}_x - \left(\frac{q}{m} \right) B_0 \frac{\omega_e}{\sqrt{\mu a^3}} \frac{\sqrt{1-e^2}(1-\sqrt{1-e^2})^2}{e^3} \sin i \cos i \sin 2\omega \hat{N}_y \\ & - \left(\frac{q}{m} \right) B_0 \frac{\omega_e}{\sqrt{\mu a^3}} \frac{\sqrt{1-e^2}(1-\sqrt{1-e^2})^2}{e^3} \sin^2 i \sin 2\omega \hat{N}_z \quad (C-2) \end{aligned}$$

$$\begin{aligned} \frac{\Delta i}{T_{period}} = & \left(\frac{q}{m} \right) B_0 \left[-\frac{1}{a^3(1-e^2)^{3/2}} + \frac{\omega_e}{\sqrt{\mu a^3}} \cos i \frac{e^2 + \cos 2\omega (1-\sqrt{1-e^2})^2}{e^2 \sqrt{1-e^2}} \right] \hat{N}_x + \left(\frac{q}{m} \right) B_0 \\ & \left[\frac{\omega_e}{\sqrt{\mu a^3}} \cos^2 i \sin 2\omega \frac{(1-\sqrt{1-e^2})^2}{e^2 \sqrt{1-e^2}} \right] \hat{N}_y + \left(\frac{q}{m} \right) B_0 \left[\frac{1}{2} \frac{\omega_e}{\sqrt{\mu a^3}} \frac{(1-\sqrt{1-e^2})^2}{e^2 \sqrt{1-e^2}} \sin 2i \sin 2\omega \right] \hat{N}_z \quad (C-3) \end{aligned}$$

$$\begin{aligned} \frac{\Delta \omega}{T_{period}} = & \left(\frac{q}{m} \right) B_0 \frac{\omega_e}{\sqrt{\mu a^3}} \left[2 \frac{\sin i \sin \omega \cos \omega}{e^4} (1-\sqrt{1-e^2})^2 - \frac{\cos^2 i}{\sin i} \sin 2\omega \frac{(1-\sqrt{1-e^2})^2}{e^2 \sqrt{1-e^2}} \right] \hat{N}_x + \\ & \left(\frac{q}{m} \right) B_0 \frac{1}{a^3(1-e^2)^{3/2}} (-2 \sin i + \frac{\cos^2 i}{\sin i}) \hat{N}_y + \left(\frac{q}{m} \right) B_0 \frac{\omega_e}{\sqrt{\mu a^3}} \left[-\frac{\sin i \cos i \cos 2\omega}{e^4} (1-\sqrt{1-e^2})^2 - \right. \\ & \left. \frac{\cos^3 i e^2 - \cos 2\omega (1-\sqrt{1-e^2})^2}{\sin i e^2 \sqrt{1-e^2}} \right] \hat{N}_y + 3 \left(\frac{q}{m} \right) B_0 \frac{1}{a^3(1-e^2)^{3/2}} \cos i \hat{N}_z - \left(\frac{q}{m} \right) B_0 \frac{\omega_e}{\sqrt{\mu a^3}} \\ & \left[\frac{\sin^2 i \cos 2\omega (1-\sqrt{1-e^2})^2}{e^4} + \cos^2 i \frac{e^2 - \cos 2\omega (1-\sqrt{1-e^2})^2}{e^2 \sqrt{1-e^2}} \right] \hat{N}_z \quad (C-4) \end{aligned}$$

$$\begin{aligned} \frac{\Delta \Omega}{T_{period}} = & \left(\frac{q}{m} \right) B_0 \left[\frac{\omega_e}{\sqrt{\mu a^3}} \frac{\cos i}{\sin i} \sin 2\omega \frac{(1-\sqrt{1-e^2})^2}{e^2 \sqrt{1-e^2}} \right] \hat{N}_x + \left(\frac{q}{m} \right) B_0 \left[-\frac{1}{a^3(1-e^2)^{3/2}} \cos i + \right. \\ & \left. \frac{\omega_e}{\sqrt{\mu a^3}} \frac{\cos^2 i e^2 - \cos 2\omega (1-\sqrt{1-e^2})^2}{\sin i e^2 \sqrt{1-e^2}} \right] \hat{N}_y + \left(\frac{q}{m} \right) B_0 \left[-\frac{1}{a^3(1-e^2)^{3/2}} + \frac{\omega_e}{\sqrt{\mu a^3}} \cos i \right. \\ & \left. \frac{e^2 - \cos 2\omega (1-\sqrt{1-e^2})^2}{e^2 \sqrt{1-e^2}} \right] \hat{N}_z \quad (C-5) \end{aligned}$$

APPENDIX D - PUBLICATIONS AND PRESENTATIONS

1. "Space Debris Charging and its Effect on Orbit Evolution," AIAA/AAS Astrodynamics Specialist Conference, 13-16 September 2016, Long beach, California, DOI: 10.2514/6.2016-5254.
2. (In Review)"Space Object Charging and its Effect on Orbit Evolution," Journal of Guidance, Control and Dynamics, manuscript ID: 2017-01-G002733.

APPENDIX E - ABSTRACTS

1. **“Space Debris Charging and its Effect on Orbit Evolution” published in AIAA/AAS Astrodynamics Specialist Conference:** With the increasing number of debris in the space environment surrounding Earth, it has become important to keep track of the orbits of these defunct objects so as to avoid collisions with active satellites, transiting spacecrafts or other important space assets. In this paper, attention has been paid to trajectory evolution of debris in low Earth orbit and geosynchronous orbit regions. One of the forces effecting the trajectory of a space debris is the Lorentz force, which acts when a charged body moves through the Earth's magnetosphere. Because of continuous bombardment of plasma particles, a space debris is often subject to charging. Correct modeling of Lorentz force requires correct modeling of magnetosphere and the body charge, which in turn depends on correct modeling of body currents, space-plasma environment and body capacitance. This research involves modeling of in-space charging for space debris, which are modeled as spherical conductors. Simulations incorporating Lorentz force as an additional perturbation force have been run to evaluate propagation of low area-to-mass ratio and high area-to-mass ratio objects.

2. **“Space Object Charging and its Effect on Orbit Evolution” under review process in Journal of Guidance, Control and Dynamics:** With the increasing number of debris in the space environment surrounding Earth, it has become important to keep track of the orbits of these defunct objects so as to avoid collisions with active satellites, transiting spacecrafts or other important space assets. In this paper, attention has been paid to trajectory evolution of debris in low Earth orbit and geosynchronous orbit regions. One of the forces effecting the trajectory of a space debris is the Lorentz force, which acts when a charged body moves through the Earth's magnetosphere. Because of continuous bombardment of plasma particles, a space debris is often subject to charging. Correct modeling of Lorentz force requires correct modeling of magnetosphere and the body charge, which in turn depends on correct modeling of body currents, space-plasma environment and body capacitance. This research involves modeling of in-space charging for space debris, which are modeled as spherical conductors. Simulations incorporating Lorentz force as an additional perturbation force have been run to evaluate propagation of low area-to-mass ratio and high area-to-mass ratio objects.

LIST OF SYMBOLS, ABBREVIATIONS, AND ACRONYMS

A_e	Electron collection area, m^2
A_i	Ion collection area, m^2
B	Magnetic Field, T
C	Capacitance, F
I_{bsc}	Backscattered current, A
I_e	Plasma electron current, A
I_i	Plasma ion current, A
I_{ph}	Photoelectric current, A
I_{se}	Secondary electron current, A
J	Current density, A/m^2
L	Debye length, m
T_e	Electron plasma temperature, K
T_i	Ion plasma temperature, K
v_{sp}	Object speed, m/s
Z	Atomic number of object material
AM 0	Air Mass Zero
AFRL	Air Force Research Laboratory
BEC	Backscattered Electron Current
CGS	Centimeter-gram-second
CME	Coronal mass ejection
DMSP	Defense Meteorological Satellite Program
DSCS	Defense Satellite Communications System
GEO	Geosynchronous Earth orbit
GOST	Gosudarstvennyy Standart
HAMR	High area-to-mass ratio
HEOS	Highly Eccentric Orbit Satellite
IAGA	International Association of Geomagnetism and Aeronomy
IGRF	International Geomagnetic Reference Field
IMP	Interplanetary Monitoring Platform
ISEE	International Sun-Earth Explorer
LAMR	Low area-to-mass ratio
LEO	Low Earth orbit
LFM	Lyon-Fedder-Mobarry
LVLH	Local-vertical-local-horizontal
MHD	Magnetohydrodynamic
MUSCAT	Multi-Utility Spacecraft Charging Analysis Tool
NASA	National Aeronautics and Space Administration
NASCAP-2K	NASA/Air Force Spacecraft Charging Analysis Program
NASCAP-LEO	NASA Charging Analyzer Program for Low-Earth Orbit
NASCAP-GEO	NASA Charging Analyzer Program for Geosynchronous Orbit

OGO	Orbiting Geophysical Observatory
PC	Photoelectric Current
PEC	Plasma Electron Current
PIC	Particle-in-cell/Plasma Ion Current
POLAR	Potentials Of Large objects in the Auroral Region
RAAN	Right ascension of ascending node
SCATHA	Spacecraft Charging at High Altitudes
SEC	Secondary Electron Current
SPARCS	Spacecraft Charging Software
SPIS	Spacecraft Plasma Interaction System

DISTRIBUTION LIST

DTIC/OCF	
8725 John J. Kingman Rd, Suite 0944	
Ft Belvoir, VA 22060-6218	1 cy
AFRL/RVIL	
Kirtland AFB, NM 87117-5776	2 cys
Official Record Copy	
AFRL/RVSV/Ryan Weisman	1 cy

(This page intentionally left blank)